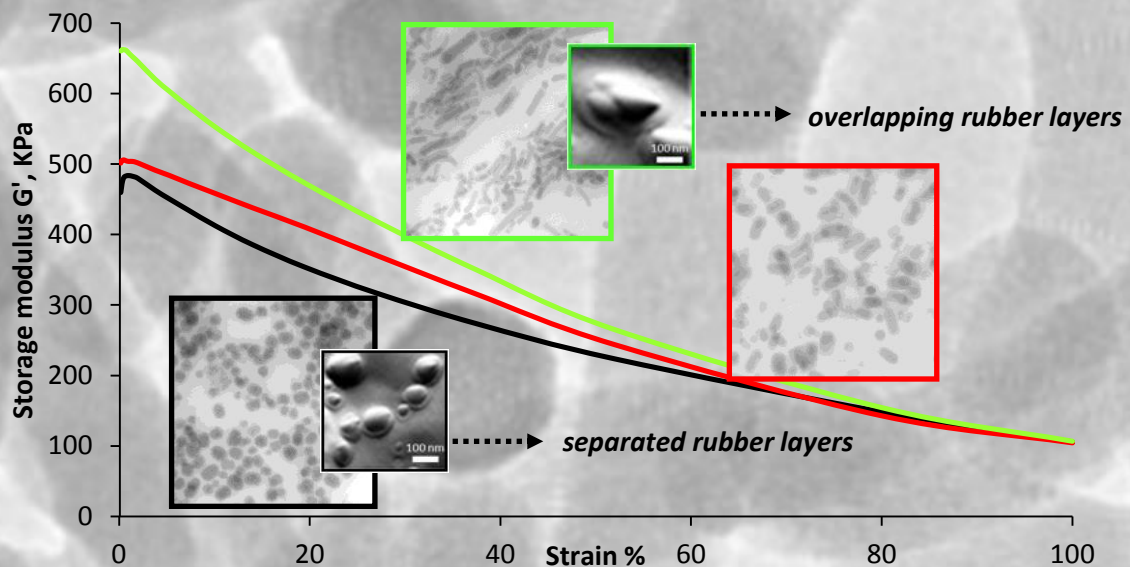




**University of Milan – Bicocca**

**Department of Materials Science**

## **Role of the silica nanoparticle anisotropy on morphological and mechanical properties of Styrene Butadiene Rubber nanocomposites**



**Doctoral dissertation in Materials Science (XVII cycle) - Industrial Curriculum**

**Luciano Tadiello**

**Supervisor: Prof. Roberto Scotti**

**Industrial tutor: Dott. Luca Giannini**

**Dean of the doctorate: Prof. Gian Paolo Brivio**



**University of Milan – Bicocca**

**Department of Materials Science**

# **Role of the silica nanoparticle anisotropy on morphological and mechanical properties of Styrene Butadiene Rubber nanocomposites**

Doctoral dissertation in Materials Science (XVII cycle) - Industrial Curriculum, of

**Luciano Tadiello**

Supervisor: Prof. Roberto Scotti

Industrial tutor: Dott. Luca Giannini

Dean of the doctorate: Prof. Gian Paolo Brivio

March 2, 2015, Milan



## **Table of contents:**

### **1. Introduction and aim of the thesis**

1.1 Introduction.....	2
1.2 Aims of the thesis.....	4
1.3 Structure of the thesis.....	5

### **2. General introduction**

2.1 Nanocomposites and hybrid materials.....	8
2.2 Characteristic features of rubber nanocomposites	
2.2.1 Nanofillers for rubber reinforcement.....	9
2.2.2 Nanocomposites morphology and filler networking.....	11
2.2.3 Nanocomposites mechanical properties.....	14
2.3 Interesting properties of rubber nanocomposites for tire formulations.....	21

### **3. Preparation of rod-like shape-controlled silica (SCS) nanoparticles and related Styrene Butadiene Rubber (SBR) nanocomposites**

3.1 Methods for obtaining silica nanoparticles.....	26
3.2 Synthesis of shape-controlled silica nanoparticles.....	28
3.3 Shape-controlled silica nanoparticles preparation.....	29
3.4 Shape-controlled silica nanoparticles characterization.....	30
3.5 Shape controlled silica/SBR nanocomposites preparation and curing.....	35

### **4. Morphology and physico-chemical properties of SCS/SBR nanocomposites**

4.1 Morphology of silica/SBR composites by TEM.....	40
4.2 Heterogeneities detection in silica/SBR composites by AFM.....	45
4.3 Physico-chemical properties of rubber nanocomposites	
4.3.1 Thermogravimetric analysis: effective filler introduction.....	49
4.3.2 Swelling experiments.....	49
4.4 Time domain (TD) NMR: mobility regimes of polymer chains	
4.4.1 MSE (Magic Sandwich Echo) experiments.....	51

4.4.2 HE (Hahn echo) experiments.....	55
4.4.3 MQ (Multiple Quantum) experiments.....	57
<b>5. Dynamo-mechanical properties of SCS/SBR nanocomposites</b>	
5.1 Rheological properties by ODR (Oscillating Disk Rheometry).....	62
5.2 Rheological behavior by the Einstein-Guth-Smallwood equation.....	67
5.3 Compression dynamics experiments.....	69
5.4 Temperature dependent dynamo-mechanical studies (DMTA).....	70
5.5 Tensile tests and Mullins effect.....	74
<b>6. Conclusions.....</b>	<b>79</b>
<b>7. Appendix: characterization techniques.....</b>	<b>83</b>

*dedicata ad Antonio e Maria*



# **Chapter 1**

## **INTRODUCTION AND AIM OF THE THESIS**



## Introduction

Rubber compounds are largely employed in the manufacturing of plastic goods, especially for the production of tires. Since the mechanical properties of rubber are poor, their improvement is guaranteed through two main processes: the addition of particulate reinforcing fillers and the vulcanization reaction. Reinforcing fillers are mixed with the rubber to improve the rigidity of the obtained compound, preserving the processability of unfilled rubber. Vulcanization is a process to improve the rubber elasticity via a polymeric network made of sulfur crosslinks. Both of them are consolidated processes used by all the major tire producers.

As regards the addition of reinforcing fillers, the tire industry extensively employs carbon black and silica particles as reinforcing fillers<sup>1</sup>.

Silica in particular allows to enhance the tear strength of the material, to increase abrasion resistance and to reduce rolling resistance of the tires.

The reinforcement effect of silica in rubber compounds depends on different contributions. It involves either the hydrodynamic effect, due to volume fraction and shape factor of the filler<sup>2</sup>, and the most important filler-rubber and filler-filler interactions. These determine the formation of an interconnected filler network in the rubber matrix, that is essential for providing effective reinforcement<sup>3</sup>. In particular, the filler-rubber interaction has been recognized to control the filler dispersion and networking through the polymer matrix<sup>4</sup>, depending on the filler particle size and shape, on the surface characteristics of the filler and on the chemical nature of the polymer<sup>5</sup>. It increases with the filler dispersion and with the extent of the organic/inorganic interface. Many studies have also demonstrated that the filler rubber interaction induces the formation of a polymer layer around filler particles with consequent slowdown of the dynamics of the rubber chains interacting with the particle surface<sup>6</sup>.

Nevertheless, the knowledge of the exact mechanism at the microscopic scale by which the filler rubber interaction affects the mechanical reinforcement is still one of the main topics of current investigation<sup>7</sup> and the effect of the inorganic/organic interface on the mechanical behavior still remains a challenge.

The prevailing theory considers that the mechanical reinforcement is related to the strength of the interaction at the filler/rubber interface, and identifies an immobilized rubber phase to describe such interaction<sup>8</sup>. The immobilized rubber is defined as a polymer film of a few nanometers<sup>9</sup>, fixed at the particle rubber interface and thus resistant to dissolution in solvent. More in detail, this film was described as composed by a primary layer of tightly bound rubber interacting with the filler through Van der Waals or chemical bonds (e.g. via silane coupling agents) and a secondary rubber layer more loosely bound to the primary one<sup>10</sup>.

Within these layers the motion of polymer chains is restricted, the rubber stiffness increasing in comparison with the free rubber far from the particles. Rubber occluded inside the particle aggregates has also been considered as a component of the immobilized rubber other than that due to direct filler rubber interaction<sup>11,12</sup>. This rubber contributes to the modulus at low strain since it is constrained in the voids of particle aggregates and is released by increasing the rubber deformation. The existence of immobilized rubber has been already revealed in carbon black<sup>9</sup>, layered silicates<sup>13</sup> and silica<sup>14</sup> filled elastomers, and it has been studied by different analytical approaches. Low field <sup>1</sup>H Nuclear Magnetic Resonance (NMR) spectroscopy has been used to measure the T<sub>2</sub> relaxation time of immobilized chains<sup>6,8</sup>; Atomic Force Microscopy (AFM) images evidenced the topography and thickness of the immobilized rubber<sup>9</sup>, and torsional harmonic AFM has been successively applied to locally determine the stiffness<sup>15</sup>.

The amount of immobilized rubber depends on the area and the nature of the filler rubber interface, and on the presence of physical constraints<sup>16</sup>. However, the influence of the particle morphology and/or of their anisotropy has not been systematically considered, particularly in the case of silica.

In fact, the beneficial reinforcing effect of anisotropic nanofillers in rubber nanocomposites was already proved in other systems. Specifically, layered<sup>17</sup> and fibrillar<sup>18</sup> silicates, carbon nanotubes and nanofibers<sup>19</sup>, halloysite nanotubes<sup>20</sup> have been investigated. However, in spite of the large number of research studies on the role of the particle size and of the filler-polymer interface in determining the mechanical properties of silica-rubber nanocomposites, only few studies have regarded different shapes of the same filler and in particular, of anisotropic silica particles. Recently, our group reported on the in-situ sol-gel synthesis of silica-rubber nanocomposites obtained by using trialkoxysilanes with different functional groups selected as precursors to modulate the filler-filler and the filler rubber interactions<sup>5,7</sup>. Silane substituents were also able to induce the formation of slightly anisotropic shaped silica particles. This highlighted that also the particle shape affected both filler-filler and filler-rubber interactions as well as the filler networking. To the best of our knowledge, no work has reported a systematic discussion of the behavior of rubber composites in relation to the different shapes of silica NPs. In particular, no studies have focused on the design and synthesis of nanocomposites based on shape-controlled anisotropic NPs with increasing aspect ratios (length/width ratios). These are expected to tune the mechanical properties of the nanocomposites, depending on the different morphology of the silica particles.

The lack of a systematic study on the role of the silica particle shape in rubber reinforcement depends on the intrinsic difficulty of tuning the silica nanoparticle shape. In fact, the synthesis of silica NPs with a controlled aspect ratio (length/width) > 1 is not an easy task. The widespread preparation methods of the oxide (e.g. hydrothermal, sol-gel, precipitation etc) generally yield

spherical or slightly irregular NPs. Elongated silica particles have been obtained as the core-shell of other oxides (e.g.  $\text{Fe}_2\text{O}_3$ )<sup>21</sup>. Besides, silica nanofibers were produced by electrospinning<sup>22</sup> or by CVD<sup>23</sup>. In the end, the only route to produce pure shape controlled anisotropic silica NPs is the sol-gel reaction in the presence of a surfactant as structure directing agent. Although the method has been generally applied to produce silica with helical mesostructure it also allows to control the particle shape<sup>24</sup>. In fact, the precursors of silica, tetraethoxysilane, TEOS, and an organotrialkoxysilane (e.g. (3-mercapto propyl)trimethoxy silane, MPTMS), arrange around the self-assembled surfactant (e.g. cetyltrimethylammonium bromide CTAB) micelles during the hydrolysis and condensation reactions. Depending on the trialkoxysilane/TEOS ratio, particles ranging from spherical (0D) to rod-like (1D) with different shape factors, are produced<sup>25</sup>.

### **Aim of the thesis**

The aim of the present work is to investigate the influence of the anisotropic silica particles on the dynamic-mechanical behavior of the SBR nanocomposites, based on the design and synthesis of filler nanoparticles with specific and defined morphology, and considering the formation of the nanoscale rigid rubber at the interface with the filler.

In particular, we focused on the synthesis of shape controlled silica nanoparticles with aspect ratio ranging from 1 to 10 obtained by a sol-gel route assisted by CTAB as structure directing agent. Such NPs were used to prepare silica/SBR nanocomposites by ex-situ blending method. In order to separate the effect of the particle shape from that of the oxide surface chemistry, the same coupling agent and graft density were used for all the prepared compounds. The purpose was to consider the aspect ratio as the only geometrical variance in the silica- rubber systems.

The size, the shape and the assembling of silica NPs were investigated by transmission electron microscopy (TEM) to correlate the filler morphology with the extent of the network in the rubber matrix. The efficacy of the filler network to bind rubber was assessed by swelling measurements.

The morphology of the nanocomposites and the topography of the immobilized rubber were investigated by the integrated approach of Transmission Electron Microscopy (TEM) with AFM, to visualize the stiffest elastomer zone at the interface. Low field  $^1\text{H}$  NMR measurements were performed using Magic Sandwich Echo (MSE) to investigate the mobility of rubber chains close to the filler particles, distinguishing between the motional regimes of tightly immobilized and more loosely interacting and free rubber. To better characterize the less immobilized fractions of the rubber matrix Hahn-Echo (HE) and Multiple Quantum (MQ) techniques were also used.

Dynamic Mechanical Thermal Analysis (DMTA) assessed the fraction of rubber with reduced mobility which affects the stress/strain behavior of cured silica/SBR nanocomposites, and tensile stress-strain tests allowed to study the behavior under high deformation.

Finally, the dynamic-mechanical properties of uncured and vulcanized silica/SBR nanocomposites were investigated and discussed, allowing to suggest a connection between the shape of the silica particles and the functional properties.

### **Structure of the thesis**

The research described hereby employs filler/rubber model systems to understand the reinforcing mechanism operated by silica nanofillers, having spherical and/or rod-like particle shape:

In **Chapter 2** of this thesis the background of hybrid materials and nanocomposites is reviewed, in order to point out the materials class of filler/rubber systems. The main part of the chapter is dedicated to the morphology-properties relation typical for this kind of materials, and the properties of interest for the tire manufacturer.

In **Chapter 3** the preparation of shape-defined silica nanoparticles and related nanocomposites is described, in order to optimize the characteristics of a model system in which the only variable is represented by the nanoparticle shape.

In **Chapter 4** the morphology of nanocomposites containing silica with different particle shape is described, in particular related to self-assembly of nanofillers with different aspect ratios and the formation of an interfacial layer of rubber, stabilized at the particle interphase. The properties of these materials, in relationship with the morphological features, will be the subject of **Chapter 5**.

Finally, **Chapter 6** sums up the main results and reports the conclusions of the investigation.

### **References**

- (1) Hall E., Moreland J.C., *Rubber Chem Technol* **2001** 74, pp. 525–539.
- (2) J.Frolich, W.Niedermeier and H.D.Luginsland, *Compos. Part A-Appl.S.*, 2005, **36**, 449-460
- (3) Zhenhua W., Jun L., Sizhu W., Wenchuan W. and Liqun Z., *Phys. Chem. Chem. Phys.*, 2010, **12**, 3014-3030
- (4) Leblanc J. L. *Prog. Polym. Sci.* **2002**, 27, 627–687
- (5) Scotti R., Wahba L., Crippa M., D'Arienzo M., Donetti R., Santo N., Morazzoni F. *Soft Matter* **2012**, 8, 2131–2143.
- (6) J Berriot, F Lequeux, L Monnerie, H Montes and Paul Sotta, *Journal Non-Crys. Solids*, 2002, 719-724

- (7) Wahba L., D'Arienzo M., Donetti R., Hanel T., Scotti R., Tadiello L., Morazzoni F. *RSC Advances* **2013**, 3, 5832.
- (8) Papon A., Saalwachter K., Schaler K., Guy L., Lequeux F., Montes H. *Macromolecules* **2011**, 44, 913–922.
- (9) Qu M., Deng F., Kalkhoran S. M., Gouldstone A., Robisson A., Van Vliet K. J. *Soft Matter* **2011**, 7, 1066–1077
- (10) Choi S. S., Ko E., *Polymer Testing* **2014** 40, 170-177
- (11) Medalia, A. I.; Laube, S. G. *Rubber Chemistry And Technology* **1978**, 51, 89-109.
- (12) Medalia, AI, *Rubber Chemistry And Technology* **1978**, 51, 437-523.
- (13) Schon F., Thomann R., Gronski W., *Macromol. Symp.* **2002** 189, 105–110
- (14) Montes H., Chaussee T., Papon A., Lequeux F., Guy L., *Eur. Phys. J. E* **2010** 31, 263–268
- (15) Schön P., Dutta S., Shirazi M., Noordermeer J., Vancso G. J. *J Mater Sci* **2011**, 46, 3507–3516.
- (16) Fragiadakis D., Bokobza L., Pissis P., *Polymer* **2011**, 52, 3175-3182
- (17) M. Galimberti, A. Lostritto, A. Spatola, G. Guerra, *Chem. Mater.* 2007, **19**, 2495-2499
- (18) M. Tian, L. Cheng, W. Liang, L. Zhang, *Macromol. Mater. Eng.* 2005, 290, 681–687.
- (19) L. Bokobza, *Polymer* , 2007, **48**, 4907-4920.
- (20) R. Kamble, M. Ghag, S. Gaikawad, B. K. Panda, *J Adv Scient Res*, 2012, **3**, 25-29.
- (21) A Sánchez-Ferrer, M Reufer, R Mezzenga, P Schurtenberger and H Dietsch, *Nanotechnology*, 2010, **21** 185603
- (22) GH An, SY Jeong, HJ Ahn, *Materials letters*, 2011, **65**, 2377–2380
- (23) CS Choi, JH Yoon, *Applied physics A*, 2012, **108**, 509–513
- (24) Du X., He J. *Dalton Trans.* **2010**, 39, 9063-9072
- (25) Scotti R., Conzatti L., D'Arienzo M., Di Credico B., Giannini L., Hanel T., Stagnaro P., Susanna A., Tadiello L., Morazzoni F., *Polymer* **2014**, 55, 1497-1506

## **Chapter 2**

# **SILICA-RUBBER NANOCOMPOSITES**

The chapter is aimed to describe rubber nanocomposites as a class of materials with tunable properties. The driving concepts useful to understand nanocomposites dynamic behavior will be described, in close relationship with their morphology up to the nanoscale. Particular attention will be dedicated to rubber nanocomposites of reinforcing nanoparticles that can be spherical or anisotropic. The properties of interest for the tire manufacturer will also be reported in order to discuss the necessary strategies for improving the desired performances, which are related to the reinforcement effect.

## 2.1 Nanocomposites and hybrid materials

A composite material is defined as a formulate obtained by the combination of two or more materials; the composite is phase-separated, meaning that one or more components constitute the continuous phase (also called matrix) while one or more components constitute the dispersed phase (also called filler or extender). Other molecular components (that are miscible in one or more phases) can be present in the formulation, as coupling agents (acting at the interface between filler and matrix) and additives of different kind (for example oxygen scavengers with antidegradative effect).

A nanocomposite material is a composite in which one of the phase-separated constituent (typically the filler) is present in nanometric form at least along one dimension<sup>1</sup>. Since the exposed surface of a particulate material goes with the power of three with respect to the size of the single particles<sup>2</sup>, a big interfacial area between filler and matrix is expected to be formed, which results in an extended additional phase (interphase) with properties that differ from the bulk materials. Since the tuning of properties at the interphase can change dramatically the macroscopic properties of the whole material, nanocomposites are an attractive field of research for application in many field ranging from biomedical, catalytic processes, separation science, chemical sensing, fuel cell, solar energy accumulation, hydrogen storage, capacitors, micro/nano electronic devices, tribology, etc.

Hybrid materials are defined as a combination of an organic constituent with an inorganic counterpart; they are characterized by phase separation between organic and inorganic constituents, and an intimate contact at the interface<sup>4</sup>.

Hybrid materials are classified according to the nature of bond that exists at the inorganic/organic (I/O) interface, which is highly predictive of the final material properties. Hence, *class 1* hybrids feature weak interactions at the interface like hydrogen bonding, ionic or Van Der Waals interactions, while *class 2* hybrids are characterized by covalent bonding between the organic and inorganic constituents<sup>4</sup>.

In both cases, the hybrid material is expected to combine the good properties of the organic phase (low cost, processability, damping...) together with the good properties of the inorganic phase (electrical conductivity, elastic modulus...).

Silica/rubber nanocomposites for tires are an example of *class 2* hybrids, since a covalent bond exist between organic part (the rubber) and the inorganic part (silica). This is provided by a third component, the coupling agent, that determines the silica-rubber interaction at the molecular level.

In this thesis, silica/rubber systems will be regarded more as nanocomposites than as hybrid materials, in order to remark the importance of the size of the dispersed phase. Anyways, some characteristics related to their I/O interface will highlight their nature of hybrid material.

## **2.2 Characteristic features of rubber nanocomposites**

### **2.2.1 Nanofillers for rubber reinforcement**

Natural and synthetic rubbers, even after vulcanization, cannot be employed as a finite material for common applications (tyres, engine transmissions, conveyor belts, floor insulators, shoe soles, ecc.) without improving their hardness, toughness and wear resistance<sup>5</sup>. As a result reinforcing fillers figure as the second most abundant ingredients in rubber formulations after the rubber itself; this is testified by their presence in relatively high amount if compared to other rubber additives<sup>6</sup>. The main features of the filler that impact on the nanocomposite properties are:

\_Filler particle size: particles produced for tire application must be nanometric in size (at least along one dimension) to exert reinforcement on rubber, as represented in figure 2.1. Bulky particulate materials like calcium carbonate can be employed just to reduce the cost of the final material without any improvement of properties. In this case they can be simply called extenders or non-reinforcing fillers; these will be not considered in the thesis, so the term ‘filler’ or ‘nanofiller’ will be always referred to reinforcing nanofillers.

\_Filler particle surface chemistry: the nature of the filler surface determines the type of bonding with the matrix (covalent, Van Der Waals, H-bond, etc.) and as a consequence controls the nanocomposite homogeneity and the mechanical properties related (wear/abrasion resistance, properties at break). While carbon black surface chemistry can be controlled by simply its degree of oxidation, silica can be surface-modified with chemical compounds, in order to reduce the high hydrophilicity and to create a covalent bond with the matrix. This is the case of sulfurated silanes that are able to react both with silica and rubber<sup>7</sup>; these are the benchmark coupling agents for tire applications. A schematic of the sulfurated silica-silane reaction is reported in figure 2.2



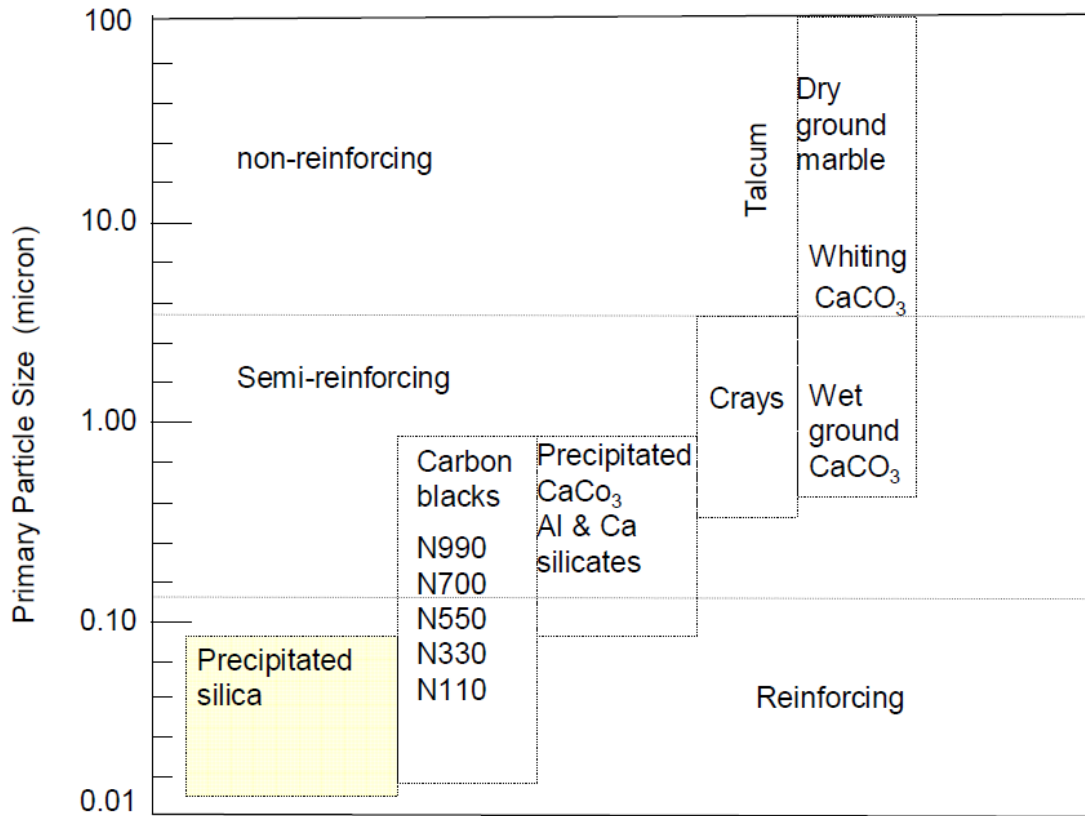


**Figure 2.1:** Classifications of filler reinforcing effect according to the particle size.

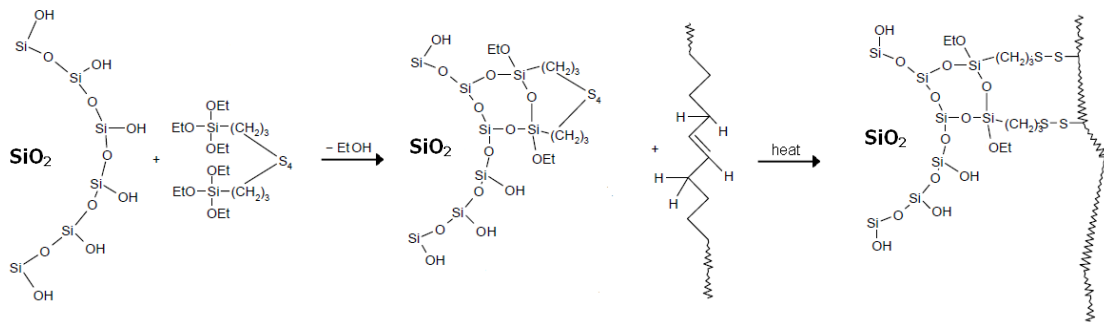


**Figure 2.2:** Schematic of the reaction of a benchmark silane (bis-(triethoxysilylpropyl) tetrasulfide) with silica surface and rubber double bonds.

In a first step, the silane is anchored to the silica particle surface during mixing; in such a way, the change of particle surface chemistry enhance the particle dispersion by reducing the surface tension at the interface. During vulcanization, the polysulfide chain of the silane reacts with the rubber insaturations to form a covalent bond between filler and matrix.

\_ Filler particle shape: filler geometry plays also an important role on the final nanocomposite textural and physical properties. In particular, an anisotropic nanoparticle is defined as an object

having at least one dimension smaller than 100 nm<sup>8</sup>. This means that both bidimensional (platelet-like) and monodimensional (fiber-like) nanoparticles fall inside this classification. Monodimensional anisotropic particles with high aspect ratio (AR 100-200) are called nanofibers, with medium (AR 10-20) are defined nanowhiskers, nanowires or short nanofibers, with low ( $1 \leq AR \leq 10-20$ ) simply nanorods<sup>9</sup>.

\_ Filler aggregation and agglomeration: filler nanoparticles might not be homogeneously distributed inside the matrix, according to the mutual affinity of the particles and the type of bonding that exist at the filler/matrix interface. By definition the term aggregate is related to undispersible clusters of nanoparticles, while the term agglomerate refers to particles clusters that can be redispersed by shearing forces<sup>10</sup>. As regards nanofillers like silica and carbon black, they are produced spherical nanoparticles fused in fractal aggregates.

The effect of the filler characteristics on final properties is studied in the nanocomposite morphological and mechanical properties.

### 2.2.2 Nanocomposite morphology and filler networking

The combination of a particulate filler and matrix should result, in the simplest case, in an homogeneous distribution of filler particles in the matrix, provided that the filler particles have no tendency to agglomerate.

The formation of agglomerates generally takes place when the filler volume fraction in a nanocomposite is relatively high ( $\gg 0.05$ ), because the total interfacial area  $A$  is large while the interparticle distance is short, as shown in Figure 2.3a . At increasing filler content, a percolative threshold is attained and all the isolated, aggregated and agglomerated nanoparticles become part of a network extended through the whole matrix (2.3b). The percolation threshold can be hence defined as the filler volume fraction at which all the particles are interconnected. In a wide sense, the 'dispersed' phase becomes the actual continuous phase, where the matrix just fills the void spaces<sup>11</sup>.

From geometrical observations, Ostwald reported that a collection of spheres of equal radius closely packed fills 74% of the volume<sup>10</sup>, the remaining 26% is empty or

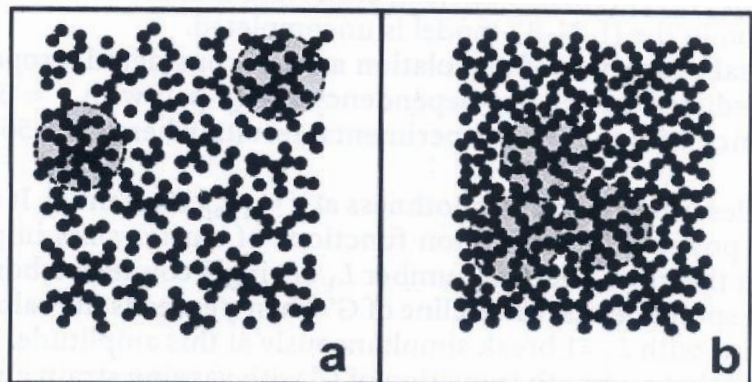


**Figure 2.3:** Sketch of the morphology of a rubber nanocomposite below (a) and above (b) filler percolation.

corresponds the outer phase. This value is the theoretical maximum filling volume in a polymer matrix, acting as outer phase. Actual percolation threshold values are much lower than the theoretical maximum filling volume as a consequence of the interactions occurring between particles (filler-filler interactions), between particle and matrix (filler-rubber interactions), and the formation of an interphase, which allow a continuous network to form even without close packing of particles. The approaches to separate and quantify these interactions will be discussed hereafter. Nanocomposite properties (such as electrical or mechanical) undergo dramatic change upon filler percolation as reported in figure 2.4

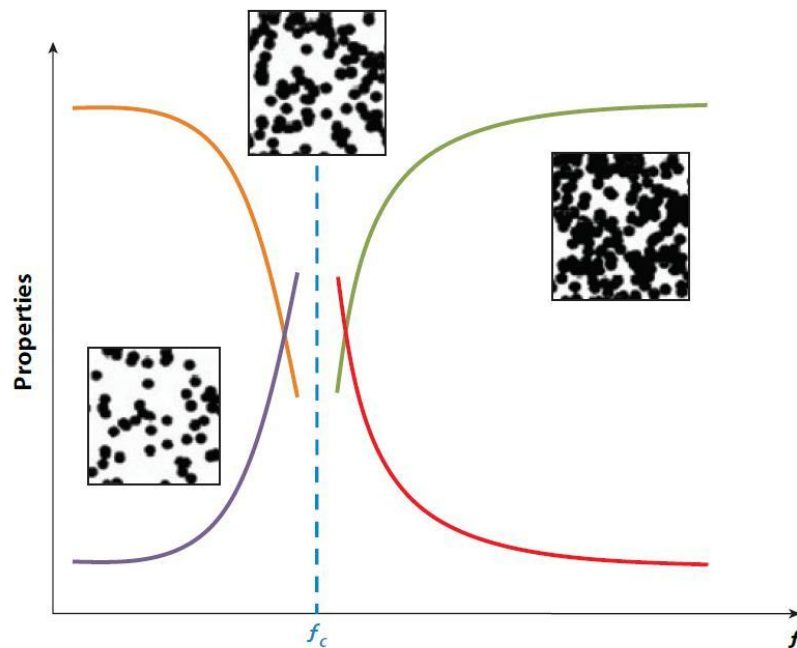


**Figure 2.4:** Schematic of nanocomposite morphology and properties at different levels of filler content.  $f_c$  is the filler percolation threshold.

Where  $f$  is the filler volume fraction and  $f_c$  is the filler percolation threshold<sup>12</sup>. For example, when an electrically conductive particulate (graphite, carbon nanotube, metal nanoparticles) is dispersed in a non-conductive matrix (like most of the polymers), the resulting composite is not significantly conductive below  $f_c$ , while becomes a good conductor above  $f_c$ <sup>12</sup>. The same occurs for the elastic modulus with reinforcing particulates: below  $f_c$  the material exhibit mainly viscous character (similarly to the unfilled polymer), while above  $f_c$  the elastic modulus suddenly improve and the dissipation factor (also called  $\tan\delta$ , related to the viscous dissipation operated by the polymer) decrease. The implications of filler morphology on dynamic properties are described more in depth in the following section.

In this context, anisotropic nanofillers can play an important role thanks to their particular morphological features, that in the case of monodimensional anisotropic nanoparticles can be defined simply by their aspect ratio (AR), e.g. the length/diameter ratio. Figure 2.5 represent a typical trend of percolation threshold with nanofiller aspect ratio

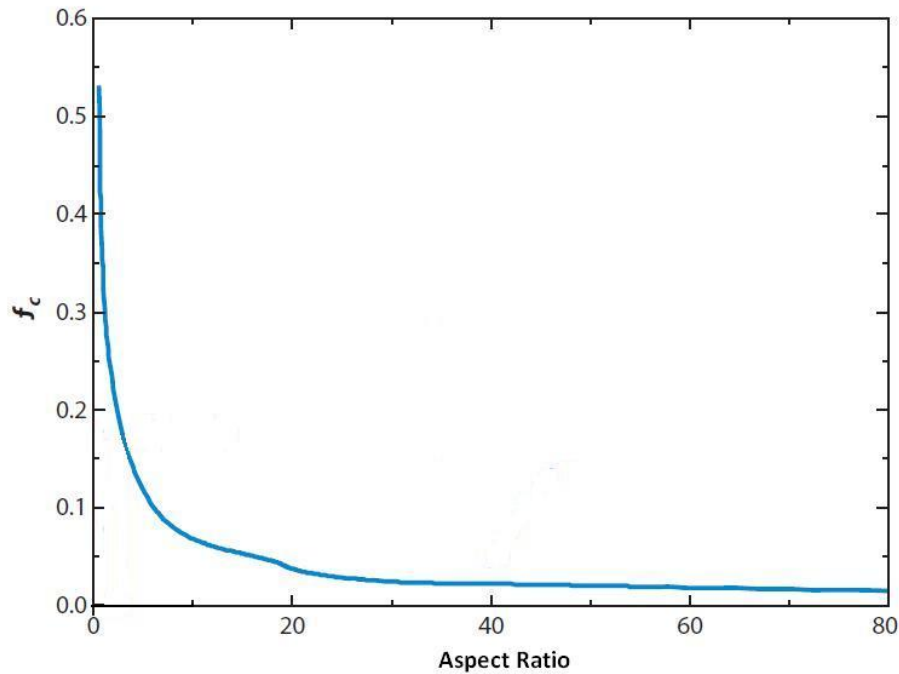


**Figure 2.4:** Percolation threshold  $f_c$  as a function of filler nanoparticles aspect ratio.

Where  $f_c$ , the filler percolation threshold, decrease at increasing filler aspect ratio<sup>13</sup>. Since the formation of a network is related to a dramatic improvement of mechanical properties, anisotropic nanofillers allow to obtain higher reinforcement at lower filler loading with respect to spherical nanofillers. As an example, spherical silica and carbon black based nanocomposites feature percolation threshold at 0,17 volume fraction<sup>14</sup>. Nanoclays represent a class of naturally anisotropic nanoparticles with wide range of aspect ratios (5-100), featuring lower percolation threshold than spherical particles, even at 0,02 volume fraction<sup>15</sup>. Finally, carbon nanotubes that can have aspect ratios in the order of 100-200 are able to form a percolative network in a rubber matrix even at a volume fraction of 0,002<sup>15</sup>.

Additionally, spherical and anisotropic nanoparticles can be also formulated together in a matrix, to obtain a nanocomposite material featuring a dual filler network: little is known about this combined reinforcing effect, but great potential is expected to come out from these mixed-filler system, as witnessed by some recent research<sup>15,16</sup>.

### 2.2.3 Nanocomposite mechanical properties

The choice of filler and matrix depend on the properties desired in the nanocomposite, but the combination of the two normally diverge from the results expected from a classical rule-of-mixture, that can be represented by the equation 1:

$$(1) \quad P(NC) = \varphi P(f) + (1 - \varphi)P(m)$$

being  $P(NC)$  a property of the nanocomposite,  $P(f)$  and  $P(m)$  the same property of the filler and the matrix,  $\varphi$  the filler volume fraction and  $(1-\varphi)$  the matrix volume fraction. This oversimplified picture does not take into account additional synergic factors originating from the combination of filler and matrix, which involves the formation of the interphase and the filler interparticle interactions. As regards the reinforcement of rubber by fillers, it is represented by the cyclic applied stress-deformation ratio, the complex modulus ( $G^*$ ) that can be decomposed in a in-phase elastic component ( $G'$ , storage modulus) and a out-of-phase dissipative component ( $G''$ , loss modulus) according to equation 2:

$$(2) \quad G^* = G' + iG''$$

The ratio  $G''/G'$  is called  $\tan\delta$ , and it indicates the ratio of energy lost to energy stored in a cyclic deformation<sup>17</sup>. The effective reinforcement operated by the filler is represented by the  $G'$ . It is not due to the simple combination of the moduli of inorganic filler and organic matrix weighted by their volume fractions. Most of published work deal with the study of the compositional and structural contributions in rubber nanocomposites to the mechanical reinforcement in terms of storage modulus  $G'$ ,  $G''$  and  $\tan\delta$ . In the following, the main models employed to evaluate the contributions to reinforcements in filler/rubber nanocomposites are reported.

#### *The Einstein-Guth-Smallwood equation*

The widely applied Einstein equation dating 1932, later modified by Guth and Smallwood was a first example of this approach. The starting point was the basic Einstein equation,  $\eta = \eta_0 * (1 + 2.5 \varphi)$ , which calculate the viscosity  $\eta$  of a suspension from the viscosity of the neat liquid  $\eta_0$  and the volume fraction of suspended material  $\varphi$  multiplied by a constant. The equation was derived considering that the effect of presence of an hard particulate material is merely hydrodynamic (e.g. it does not deform upon flow)<sup>18</sup>. This is a valid approximation for diluted systems, but not for concentrated system, which deviate from the model behavior at increasing concentrations and aspect ratio of the particulate material (figure 2.5), because of the stronger interparticle interactions.

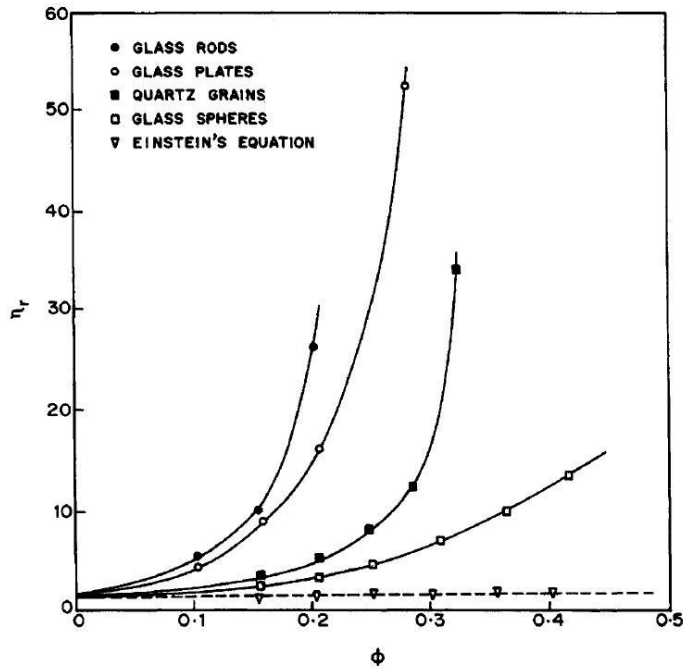


**Figure 2.5:** Deviations of the viscosity of particulate suspensions in water from the Einstein equation (dotted line) for different fillers at different concentrations.

After Guth and Smallwood, the equation was applied to filled polymers, substituting viscosity with elastic modulus, and introducing different terms which takes into account for the filler interparticle interactions and filler particle shape<sup>19,20</sup>. The most general equation for filler/polymer nanocomposites is reported below.

$$(3) \quad G'_0 = G'_{0 \text{ unfilled}} \times (1 + 0,69 \times \varphi \times AR + 1,62 \times \varphi^2 \times AR^2)$$

Where  $G'_0$  and  $G'_{0 \text{ unfilled}}$  correspond to the storage modulus at small strain values of the nanocomposite and the unfilled matrix, respectively, while  $AR$  stands for the nanoparticle aspect ratio. The equation demonstrated to be highly predictive of the final materials modulus considering nanocomposites containing a relatively low amount of filler, while at high values of filler volume fraction the formation of a percolative network provokes a dramatic deviation from the model equation<sup>21,22</sup>.

### *The Payne Effect*

The pioneeristic work of Payne<sup>23</sup> introduced a viscoelasticity-based differentiation of the components of macroscopic reinforcement of particle-filled rubber vulcanizates. Under relatively small oscillatory strain a viscoelastic material undergo a drop in the value of the initial  $G'$  modulus ( $G'_0$ ) until a plateau is reached (corresponding to  $G'_\infty$ ). In this way it is possible to separate distinctly two component of the elastic modulus  $G'$ , namely a strain-dependent and a strain-

independent one. In fact, above the percolation threshold, a network of interacting particles is diffuse throughout the whole matrix. As a deformation is applied, the filler network breaks down at relatively small strain if compared to the strain necessary for the polymer chain rupture. The filler network is held together by relatively weak forces like H-bons and Van der Waals interactions, while covalent bonds exist at the polymer-particle interface (through coupling agents), and in the in-rubber structure (sulfur crosslinks). This strain softening phenomenon is known as Payne effect, and the components of reinforcement are readily separated as reported in figure 2.6

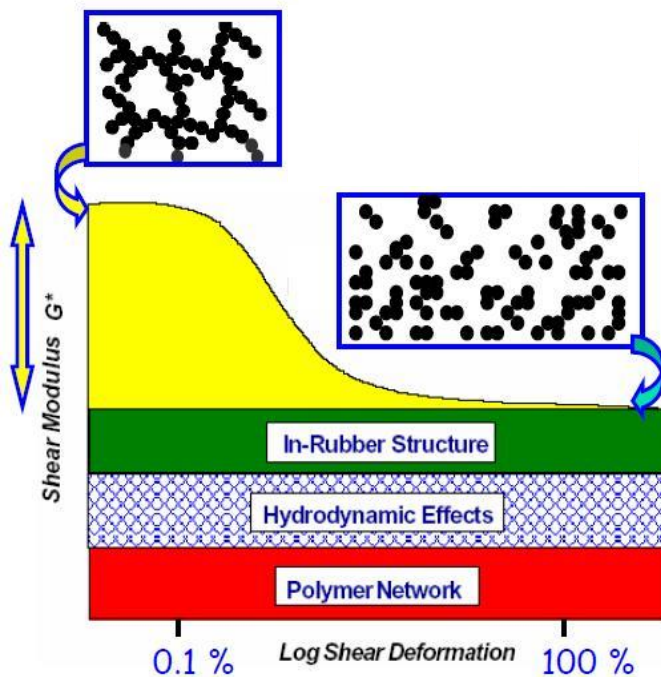


**Figure 2.6:** Schematic of stress-strain curve of a nanocomposite. The strain-dependent and strain-independent contributions to the Payne effect are differently coloured.

where the strain-dependent component (in yellow) is associated with reinforcement brought by filler-filler interactions of the filler network and the strain-independent component (other colours) is associated mainly to filler-rubber interactions. In detail, in-rubber structure and polymer network are related to the crosslink density of the matrix and the nature of the polymer<sup>23</sup>.

The extent of network breakdown can be quantified as a difference  $\Delta G'$  between  $G'_0$  and at high deformation  $G'_\infty$ <sup>23</sup>, and is associated with an energy-dissipative event (hysteresis) according to equation 3.

$$(4) \quad \Delta G' = G'_0 - G'_\infty$$

A nanocomposite characterized by an high low-strain modulus (high  $G'_0$ ) and by a low strain-dependent component (low  $\Delta G'$ ) would demonstrate high reinforcement and also low hysteresis; these technological requirements are of deep interest for the tire manufacturer.

*The immobilized rubber layer model*

The concept that rubber segmental motions can be influenced by the constraint imposed by a solid particulate was suggested by microscopic studies of Medalia<sup>24</sup>. The fractal structure of carbon black aggregates was correlated with the amount of DBP oil (dibutylphthalate) that can be absorbed by the carbon black particulate. For the first time, a differentiation was made between bound rubber, or firmly adsorbed on the particles surface, and occluded rubber, physically constrained in the carbon blacks irregularities, as represented in figure 2.7. Both of them were expected to have different properties from the bulk rubber, thanks to their different motional regimes.

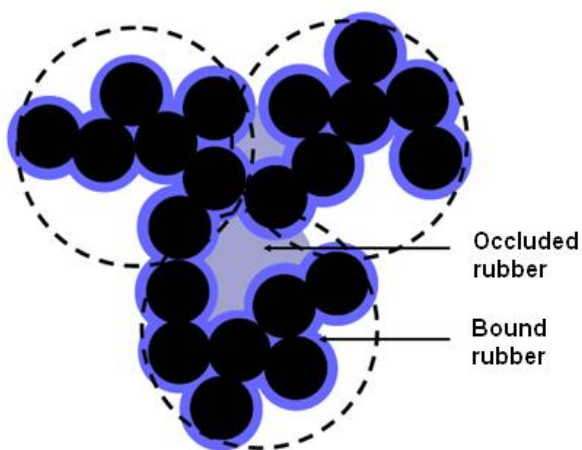


**Figure 2.7:** Scheme of the bound and occluded rubber around a carbon black aggregate, according to Medalia.

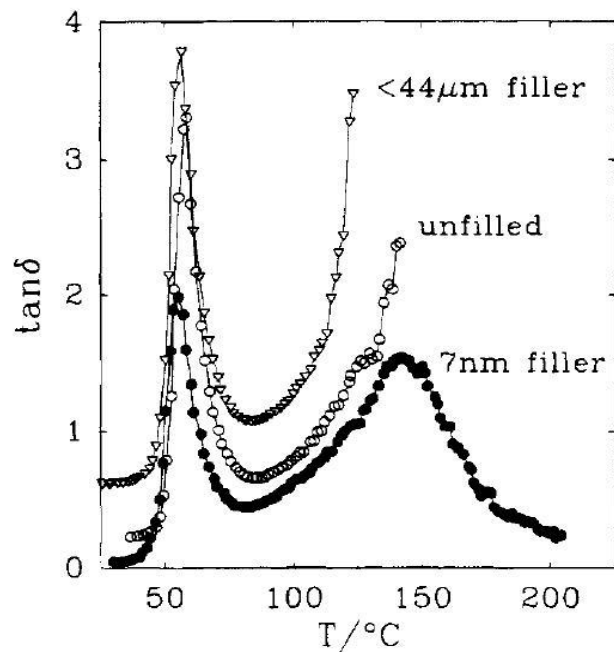


**Figure 2.8:** Temperature dependence of  $\tan\delta$ . The first peak from the left is associated with the main glass transition, while the second peak from the left corresponds to the secondary relaxation, attributed to the fraction of rubber constrained by the filler.



The first relevant evidence of the confinement effect of polymer chains entering in contact with the filler surface was brought by Tsagaropoulos and Eisenberg in 1992<sup>25</sup>; they observed the presence of a well-defined fraction of rubber with increased glass transition temperature with respect to the bulk rubber. This was detected by DMTA, which is able to separate temperature dependent dynamo-mechanical events, in particular related to energy dissipation (figure 2.8).

This observation was validated for different filler/rubber systems, and the amount of the rigid fraction increased with filler amount and exposed filler surface area<sup>26</sup>. In 2003, Arrighi also proposed a numerical method to calculate the exact amount of immobilized rubber<sup>27</sup> from DMTA curves after appropriate deconvolution routines and integration. The interpretation of this preliminary observation found later opposition in literature<sup>28</sup>, hence further investigations were necessary to clarify the issue. For this reasons, later approaches were aimed to study in detail the interactions at the interface.

NMR measurements on nanocomposites have shown the existence of polymer chains with lower mobility than the pure elastomer; in particular, were identified three regions with different mobility: a mobile region far from the particles, an outer shell with less mobility and an inner shell with very little mobility<sup>29</sup>(figure 2.9) The surrounding polymer layer is therefore divided into two parts: a firmly anchored portion (close to the surface) and a weakly bound outermost portion composed of chains interacting with the strongly bonded area. Other investigations, suggested the existence of a glass transition temperature gradient from the inner immobilized layer to the bulk rubber<sup>30</sup>.

After considering a well-defined polymeric layer surrounding each particle in the nanocomposite, the concept of filler-filler interaction requires some update. From the traditional mechanistic interpretation of the Payne effect, the network breakdown consist in the detachment of particles one from the other by rupture of reversible bonds, for example Van der Waals interactions between neighboring particles. Taking into account that the filler-filler contact must be mediated by the interfacial rubber, the Payne effect can be explained by the disentanglement of polymer chains that constitute the actual filler-filler connections. The polymer layers

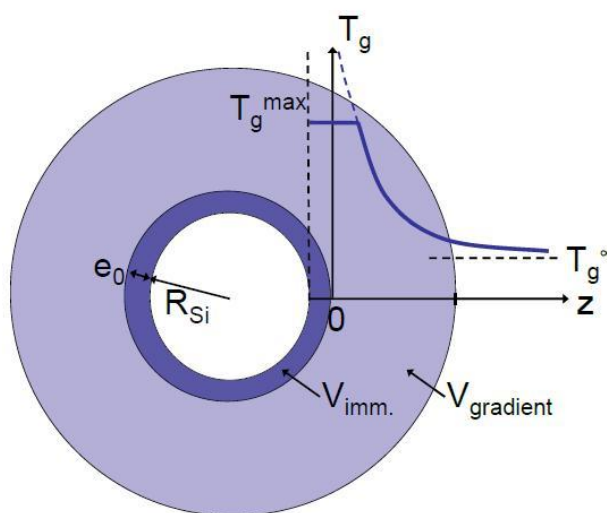


**Figure 2.9:** The rubber layer surrounding a filler nanoparticle (in white) is composed by a firmly anchored portion (dark blue) and a weakly bound outermost portion (light blue).

surrounding each single nanoparticle overlap, connecting them in a percolative network diffuse throughout the whole nanocomposite<sup>31</sup>. Some author showed evidence that this connection is made by polymer chains actually in a glassy state, and described them as ‘glassy bridges’<sup>32</sup>.

From the macroscopic point, the interface stability (associated to filler-rubber interactions) can be also evaluated by mechanical measurements that explore higher strain regimes than the Payne effect. These are tensile tests and Mullins effect. In tensile tests, the material is stretched at strain values 20-50 times higher than for the Payne effect according to the procedure in (Appendix A), and the high-strain effects can be attributed to filler-rubber interactions, that play a complex but important role on tuning the breakage mechanism. The Mullins effect refers to a particular aspect of the mechanical response in filled rubbers in which the stress–strain curve depends on the maximum loading previously encountered. In fact the Mullins effect can be evaluated by a series of tensile traction and retraction tests until break, in which a lag time between cycles allows to restore reversible deformations, while pseudo-permanent deformations cannot be restored. In addition to the simple tensile test, it is possible to evaluate the energy losses localized in different strain intervals, allowing the material to restore between one cycle and the other separating permanent (purely viscous) losses from reversible (viscoelastic) losses<sup>33</sup>. The hysteresis measured in each cycle can be considered as an indicator of these losses, as indicated in Appendix A.

The dissipative effect at different strain levels has been related with different physical phenomena, reviewed by Diani<sup>34</sup>, schematized in figure 2.10.

All these mechanism have been explained in comparison with the derivations of the theory of rubber elasticity, and are adapted for different filler-rubber systems<sup>34</sup>. The double-layer model is a more recent implication, that is particularly useful for systems in which there is direct evidence of a well-defined interfacial rubber layer. This aspect is discussed in a paper of Fukahori<sup>35</sup>, in which the evolution of bridging interfacial rubber of the secondary layer during Mullins test is schematized as follows:

- \_ Upon sample stretching, rubber immobilized on the surface is not moving, while bridging layers are stretching (figure 2.11a).
- \_ When the strain is released, the bridging rubber layers are withdrawing dissipating the stored energy and without coming back to the starting position (figure 2.11b). Hence, in the next stretching, these ‘buckled’ layers will not contribute in giving any modulus improvement.

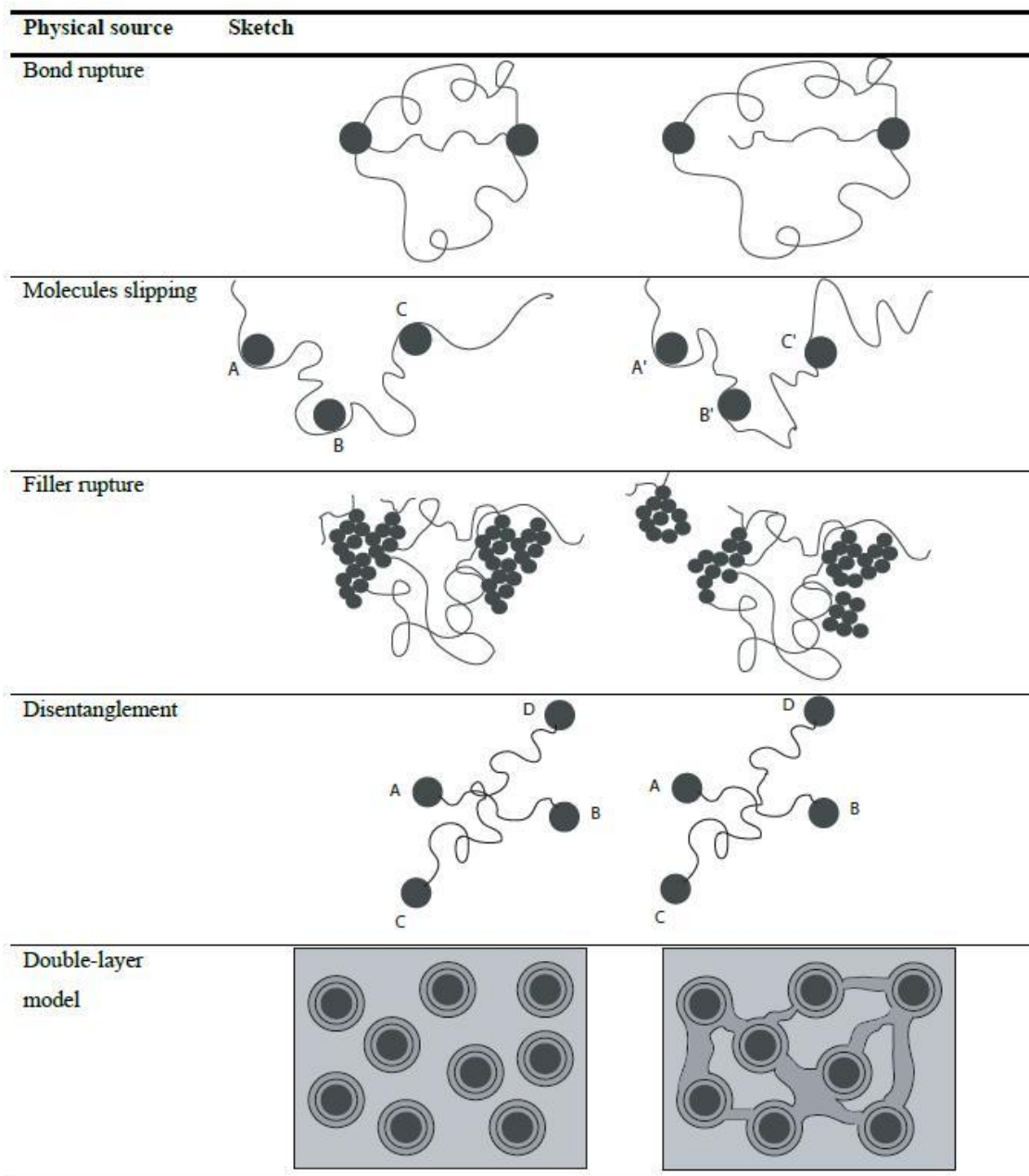


**Figure 2.10:** Different dissipative mechanisms associated to the Mullins effect.

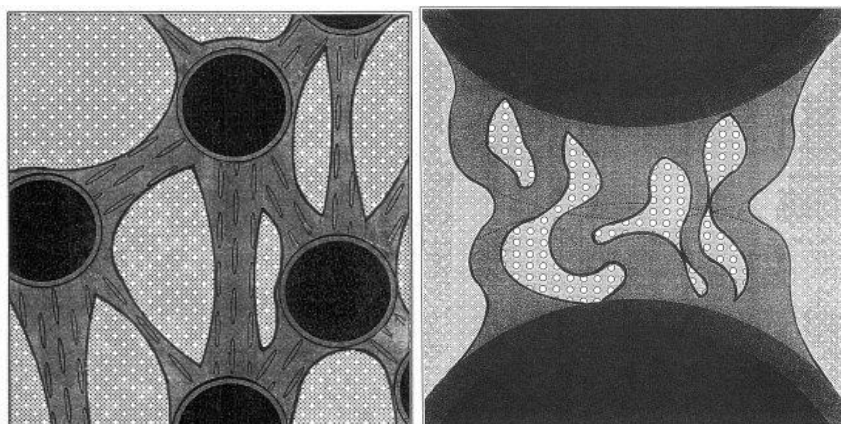


**Figure 2.11:** Model of the double-layer evolution upon strain during the stretching and after the pseudo-permanent deformation.

This means that even if at low strain the contribution of interparticle rubber layers to reinforcement is markedly high, upon high deformations they will lose irreversibly their reinforcing action<sup>35</sup>.

As a final remark, no direct relationship between the particle shape and the filler-rubber interface has been proposed in literature up to now for silica/rubber nanocomposites. Even if it is well understood that the use of anisotropic in spite of spherical nanofillers imparts beneficial properties to rubber nanocomposites, the reinforcing mechanism at the nanoscale is still to be investigated for these systems and will be the main topic of this thesis.

### 2.3 Interesting properties of rubber nanocomposites for tire formulations

A tire is built up from different crude rubber formulates, shaped into single components (tread, innerliner, etc.). These crude components are assembled together with the non-rubber components (steel carcass, cords, etc.) and eventually the tire is cured in a press. The main steps of tire manufacture are summarized in figure 2.12, with highlighted the part related to rubber formulates.

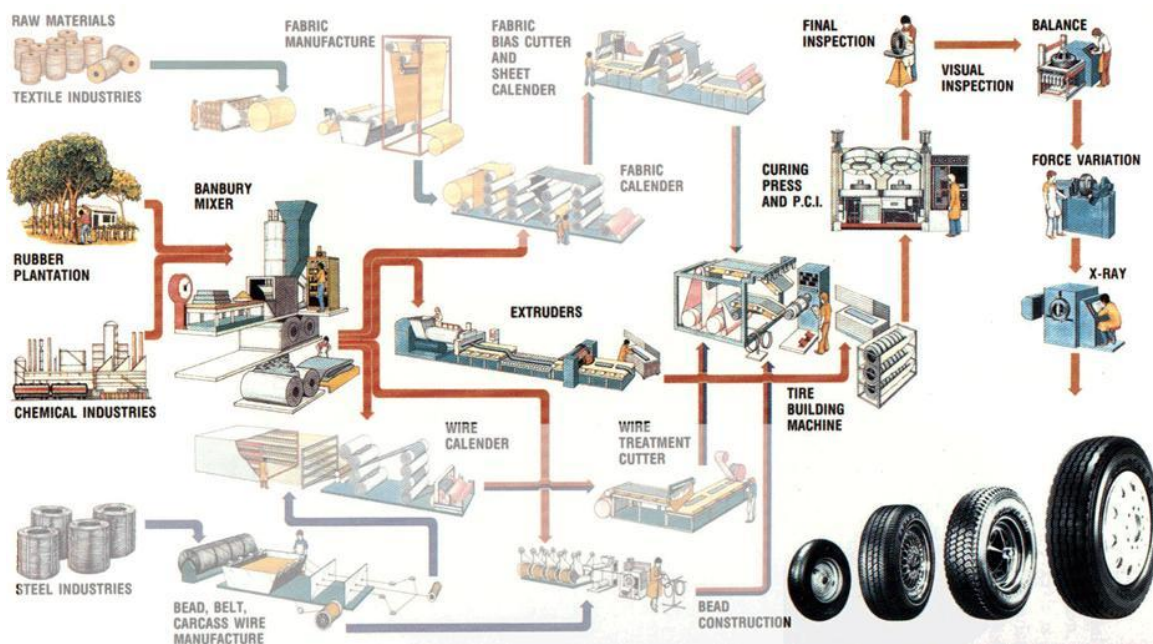


**Figure 2.12:** Scheme of the industrial processing of a tire from the raw materials

Without going into details into non-tread components, the tread formulation is the most important one, first for its presence<sup>36</sup> and second because is the part in direct contact with the asphalt, where the main energy dissipation occurs.

A commonly used representation for the tire tread performance is the magic triangle graph, where three

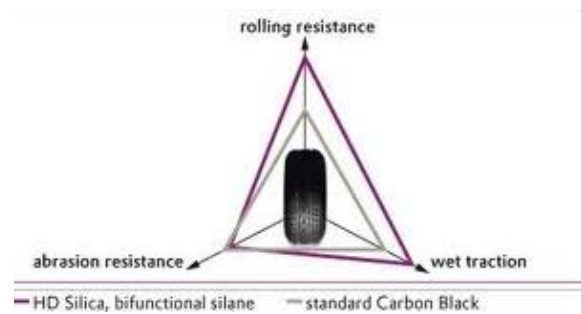


**Figure 2.13:** The magic triangle graph

main properties can be compared and related to the tread formulations examined.

These main indicators are:

\_ Rolling resistance: the resistance opposed by the asphalt to the tire movement. It is not just dependent on the kinetic friction coefficient, but also on the deformation of the tire, which is an energy dissipating event. Highly elastic tires feature a reduced rolling resistance. From the dynamo-mechanical point of view, the  $\tan\delta$  value in the tire marching conditions is a strong indicator of the rolling resistance.

\_Abrasion resistance: the ability of the tread to resist wear, which is a complex phenomenon, dependent among all on the properties at high deformation (for example: elongation at break).

\_Wet traction: the ability of the tread to guarantee good grip with the asphalt even in wet conditions. A good indicator of wet traction can be the high material hysteresis at low temperature.

Unfortunately it is rarely possible to elaborate a tread formulation improving all of these three indicators together. A compromise has to be reached for having a good balance of final material performance: for example, a stiff tread formulation (high storage modulus and low  $\tan\delta$ ) would reduce rolling resistance, but also decrease abrasion resistance of the tire<sup>37</sup>. In this context, the availability of new raw and modified nanomaterials is a promising starting point for rubber technologists that aim to improve the tire performance.

## References

- [1] P. M. Ajayan, L. S. Schadler, P. V. Braun, *Nanocomposites Science and Technology*, Wiley, **2003**
- [2] S. Lowell, Joan E. Shields, Martin A. Thomas, Matthias Thommes, *Characterization of Porous Solids and Powders: Surface Area, Pore Size and Density*, Kluwer Academic Publishers, **2004**
- [3] Patrick Judeinstein and Clément Sanchez *J. Mater. Chem.*, **1996**,6, 511-525
- [4] Clément Sanchez, Beatriz Julián, Philippe Belleville and Michael Popall *J. Mater. Chem.*, **2005**,15, 3559-3592
- [5] Alan N. Gent, *Engineering with rubber*, Hanser Publications, **2012**
- [6] [http://www.indiarubberdirectory.com/engineering/standard\\_rubber\\_formulations.asp](http://www.indiarubberdirectory.com/engineering/standard_rubber_formulations.asp)
- [7] Annemieke ten Brinke, *Silica Reinforced Tyre Rubbers*, PhD thesis, Twente University Press, **2002**
- [8] MacNaught, Alan D. and Wilkinson, Andrew R., ed. *Compendium of Chemical Terminology: IUPAC Recommendations* (2nd ed.). Blackwell Science, **1997**.
- [9] Anil K. Bhowmick, *Current Topics in Elastomer Research*, Taylor & Francis Group, **2008**

- [10] H. Mollet, A. Grubenmann, *Formulation Technology*, Wiley, **2001**
- [11] D. Stauer and A. Aharony, *Introduction to Percolation Theory*, Taylor & Francis, **1994**
- [12] C. W. Nan, Y. Shen, J. Ma, *Annu. Rev. Mater. Res.* **2010**, 40, 131–51
- [13] V. Favier, *Etude de Nouveaux Materiaux Composites Obtenus a Partire de Latexes Filmogenes et de Whiskers de Cellulose*, PhD thesis, Institut Politechnique de Grenoble, **1996**
- [14] K. Yurekli, R. Krishnamoorti, M. F. Tse, K. O. McElrath, A. H. Tsou, H. C. Wang, *Journal of Polymer Science: Part B: Polymer Physics*, **2001**, 39, 256–275
- [15] L. Giannini, M. Galimberti, V. Cipolletti, M. Coombs, L. Conzatti, M. Mauro, G. Guerra, *Rubber Vision Of High Aspect Ratio Nanofillers*, International Rubber Conference, Paris, 2013
- [16] L. Bokobza, E. Leroy, V. Lalanne, *European Polymer Journal*, **2009**, 45 996–1001
- [17] G. Heinrich, M. Kluppel, T. A. Vilgis, *Current Opinion in Solid State Materials Science*, **2002**, 6, 195-203
- [18] Shang W, Williams JW, Soderholm KJM. *J Mater Sci* **1994**, 29, 2406-16.
- [19] Nan CW, Shen Y, Ma J. *Annu Rev Mater Res* **2010**, 40, 131-51;
- [20] Xu J, Florkowski W, Gerhardt R, Moon K, Wong CP. *J Phys Chem B* **2006**, 110, 12289-92.
- [21] R. Scotti, L. Conzatti, M. D'Arienzo, B. Di Credico, L. Giannini, T. Hanel, P. Stagnaro, A. Susanna, L. Tadiello, F. Morazzoni, *Polymer* **2014**, 55, 1497-1506
- [22] K. W. Stockelhuber, A. S. Svistkov, A. G. Pelevin, and G. Heinrich *Macromolecules* **2011**, 44, 4366–4381
- [23] H.-D. Luginsland, J. Flohlich and A. Wehmeier, *Rubber Chem. Technol.*, **2002**, 75, 563–579
- [24] A. I. Medalia, *Rubber Chemistry and Technology* **1978**, 51, 437-523
- [25] Tsagaropoulos G., Eisenberg A., *Macromolecules* **1994**, 28, 6067-6077
- [26] Tsagaropoulos G., Eisenberg A, *Macromolecules* **1996**, 28, 396-398
- [27] Arrighi V., McEwen I.J., Qian H., Serrano Prieto M.B., *Polymer* **2003**, 44, 6259–6266
- [28] C. G. Robertson, C. J. Lin, M. Rackaitis, C. M. Roland, *Macromolecules* **2008**, 41, 2727-2731
- [29] Berriot J., Montes H., Lequeux F., Long D., Sotta P. *Macromolecules* **2002**, 35 (26), 9756–9762
- [30] Papon A., Saalwachter K., Schaler K., Guy L., Lequeux F., Montes H. *Macromolecules* **2011**, 44, 913–922
- [31] L. Wahba, M. D'Arienzo, S. Dirè, R. Donetti, T. Hanel, F. Morazzoni, M. Niederberger, N. Santo, L. Tadiello, R. Scotti *Soft Matter* **2014**, 10, 2234-2244
- [32] Montes H., Chaussee T., Papon A., Lequeux F., Guy L., *Eur. Phys. J. E* **2010** 31, 263–268
- [33] Schmoller K. M., Bausch A. R., *Nature Materials* **2013**, 278-281
- [34] Diani J., Fayolle B., Gilormini P., *European Polymer Journal* **2009**, 601-612

[35] Fukahori Y., *J. Appl. Polym. Sci.* **2005**, 95, 60–67

[36] <http://www.wrap.org.uk>

[37] B. Heissing, M. Ersoy, *Chassis Handbook*, Springer, **2011**

## **Chapter 3**

# **PREPARATION OF ROD-LIKE SHAPE-CONTROLLED SILICA (SCS) NANOPARTICLES AND RELATED STYRENE BUTADIENE RUBBER (SBR) NANOCOMPOSITES**



The chapter reports the preparation of spherical and rod-like anisotropic silica nanoparticles and the preparation of corresponding Styrene Butadiene Rubber (SBR) nanocomposites. First, the different methods for obtaining silica nanoparticles are described. Then, the synthetic methodology used for obtaining shape-controlled anisotropic silica nanoparticles having different aspect ratios is reported, as well as the preparation of nanocomposites of rubber filled with anisotropic silica nanoparticles.

### 3.1 Methods for obtaining silica nanoparticles

#### Precipitated silica

Precipitated silica is the most commonly used nanofiller in rubber industry, and it is prepared by acidification of an aqueous solution of sodium metasilicate.

A typical production plant for precipitated silica is schematically represented in figure 3.1

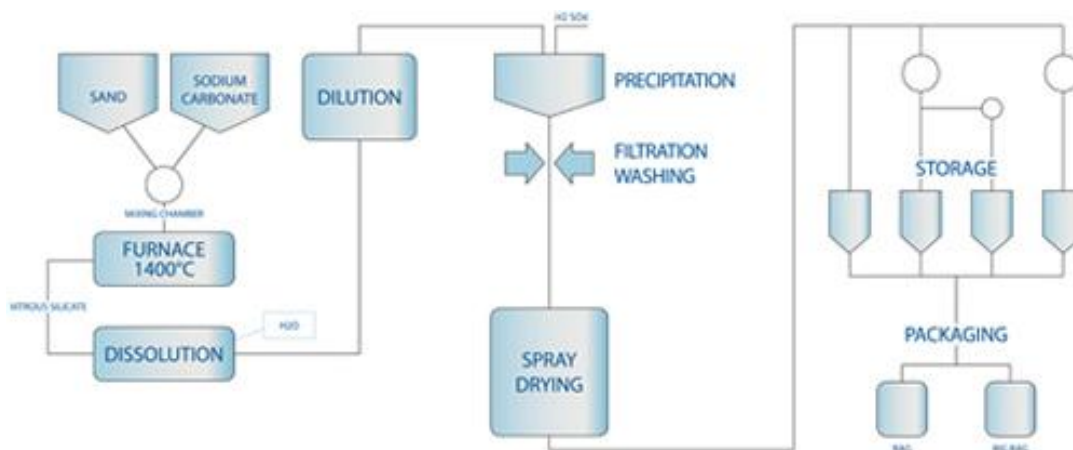


**Figure 3.1:** Industrial plant for the preparation of precipitated silica nanoparticles.

Sodium metasilicate  $\text{Na}_2\text{SiO}_3$  which is first produced from sand in a voltaic arc furnace; it is dissolved in highly basic solution ( $\text{pH} > 14$ ). When diluted in water, a white colloidal powder forms; after further addition of acid (most employed is diluted  $\text{H}_2\text{SO}_4$ ) the powder precipitates and can be filtered out from the reaction medium and dried. By controlling the reaction conditions, it is possible to tune the size of spherical particles, generally from 10 nm to microns, but not the shape, except for some patent that reports also the possibility of obtaining slightly ellipsoidal particles.

#### Sol-Gel silica

Sol-gel synthesis is the most versatile method to obtain metal oxide nanoparticles with defined properties. As regards silica, sol-gel synthesis is particularly useful for tailoring nanoparticle size, surface chemistry and shape just by controlling the reactions condition. The molecular precursors employed are generally alkoxysilanes with general formula  $\text{Si}(\text{OR})_4$ , where R can be methyl, ethyl, ecc., of which the most common is tetraethylorthosilicate (TEOS). The reaction is catalyzed by

acids or bases and can be carried out in water, in an organic solvent or in hydroalcoholic solution<sup>1</sup>. A typical reaction pathway is presented in figure 3.2:

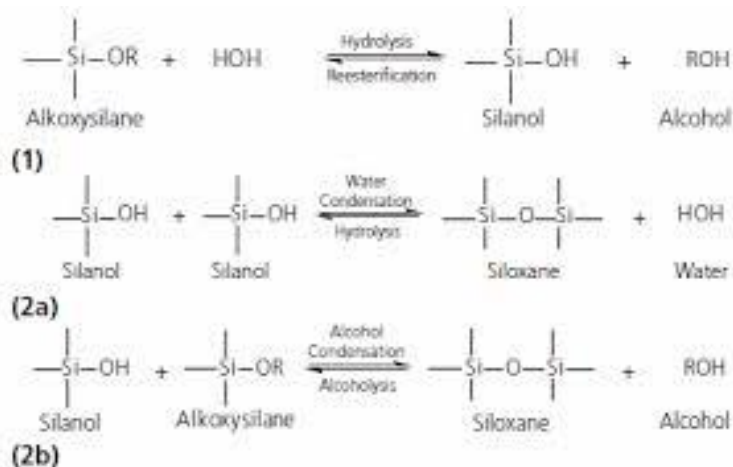


**Figure 3.2:** Schematic of the sol-gel process: hydrolysis (1), water condensation (2a), silanol condensation (2b).

Where the alkoxy silane undergo hydrolysis first (1) and condensation later (2). The obtained silica material is chemically similar to the silica obtained by precipitation, but thanks to the much higher possibility of controlling the reaction kinetics the control of the nanoparticle properties is more favorable.

Sol-gel silica production for rubber compounds allows also for preparing the filler nanoparticles directly inside the rubber matrix, via an *in-situ* approach. Many research groups studied this possibility<sup>2,3</sup>, obtaining nanocomposites with improved mechanical properties and a tailored growth of silica nanoparticles in the matrix. In a previous investigation in my research group, it was possible to tune the particle surface chemistry and also to slightly modulate the nanoparticle shape, obtaining a direct correlation between the *in-situ* sol-gel reaction conditions and the morphological and dynamo-mechanical properties of silica/rubber nanocomposites<sup>4,5</sup>. These studies were useful as model systems, in which the preparation conditions could be precisely controlled and gave straightforward indications for improving conventional silica/rubber nanocomposites.

Despite the great potential of sol-gel technique over silica precipitation, the industrial production of silica by this methodology is confined to high added value goods, like antireflective Amiran glasses, silica-microencapsulated avobenzone for sunscreen creams and different supports for catalysis and chromatography<sup>6</sup>. As regards the *in-situ* sol-gel synthesis, the topic is still an hot topic of academic research for understanding the reinforcement mechanism in real nanocomposites.

### 3.2 Synthesis of shape-controlled anisotropic silica nanoparticles

To obtain shape-controlled amorphous silica NPs with a controlled aspect ratio is not an easy task. The preparation methods of the oxide (e.g. hydrothermal, sol-gel, precipitation) yield spherical or slightly irregular NPs. Few preparation methods to obtain shape-controlled silica nanoparticles are reported here.

\_ Elongated silica particles have been obtained as the core-shell of other oxides, exploiting the shape of the native oxide (e.g.  $\text{Fe}_2\text{O}_3$ <sup>7</sup>) and coating the particles with a layer of few nanometers of silica.

\_ Silica nanofibers were produced by electrospinning<sup>8</sup> from a solution of TEOS; as a result, curly nanofibers were deposited on the target of the electrospinning device.

\_ Silica nanofibers were also produced by Chemical Vapor Deposition (CVD<sup>9</sup>) from silica precursors deposited in a vacuum chamber. Fibers with high aspect ratio (>20) were obtained by this procedure.

At the end, the most promising procedure for obtaining shape-controlled silica nanoparticles is the sol-gel synthesis assisted by a templating agent, which consists in a component of the reaction mixture that is intrinsically anisotropic, generally thanks to a process of self-assembling of the templating system in the reaction conditions.

Generally a templating or structure-directing agent (SDA) system exploits the formation of liquid/liquid interfaces that constrains the silica particle growth, which occurs just in the aqueous phase. Different examples can be anisotropic micellar systems, or immiscible two-solvents systems, in which the particle forms parallel<sup>10</sup> or orthogonal<sup>11</sup> to the interface between the two solvents.

The most versatile templating system consists in cylindrical micelles of cetyl trimethyl ammonium bromide (CTAB). This system was formerly employed for the preparation of MCM-41 silica nanoparticles for catalysis, as a scaffold for obtaining silica nanostructure with high surface area, leading to the formation of mesoporous channels due to the presence of the CTAB cylindrical micelle. Later, the system was studied more in depth and the different shapes of CTAB micelles were used to tune the morphology of the mesoporous channels. The reaction conditions (concentration, temperature) in which the CTAB molecule forms micelles in water having different shapes is reported in figure 3.2b. Furthermore, the reaction was carried out in the presence of a co-structure directing agent (co-SDA) able to act as a reaction starting point in proximity of the water/CTAB interface. In this way, combining the cylindrical shape of CTAB micelles and the nature and amount of co-SDA, not only the pore structure but also the nanoparticle shape could be controlled (figure 3.2a)<sup>12,13</sup>.

This last method<sup>13</sup> was chosen in the thesis for the preparation of shape-controlled silica nanoparticles with different aspect ratios.

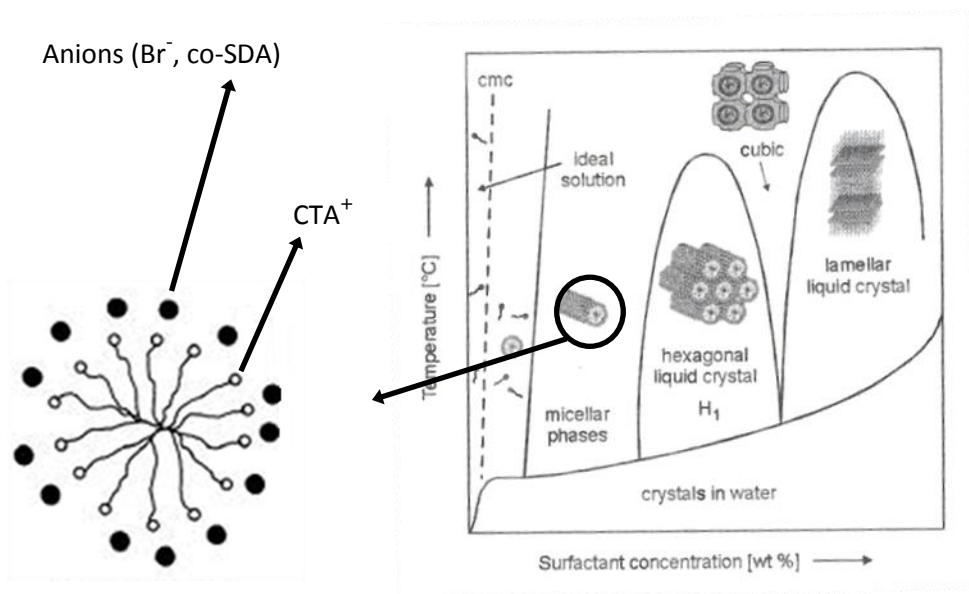


**Figure 3.3:** Schematic of the arrangement of anions around CTAB cylindrical micelle (section) (a); phase diagram of the shape of CTAB micelles

### 3.3 Shape-controlled silica nanoparticles preparation

Shape controlled silica nanoparticles have been prepared by sol-gel reaction in an aqueous basic medium using TEOS as molecular precursor. In a typical procedure, 4 g of CTAB were dissolved at 70°C in a solution of 14 mL of NaOH 2 M and 1920 mL of Milli-Q water. After 5 min of vigorous stirring, 24.0 mL of TEOS and a suitable amount of MPTMS (3-mercaptopropyl)trimethoxysilane (0, 1.0, 2.0, 2.5, 3.0 mL) were added. In this system, MPTMS is deprotonated and as an anion it replaces the bromide ions surrounding CTAB micelles: this interaction is crucial to obtain a structural control. The reaction was carried out for 2 hours for all the silica specimens<sup>13</sup>.

The reaction mixture work-up procedure consists in the following steps: the mixture was filtered and the powder was dispersed in a washing solution of 40 mL of HCl (37 wt%) and 300 mL of ethanol. By stirring the sample for 24 h at 60°C it was possible to remove up to 98% of the CTAB. Then, silica nanoparticles were suspended in water (5.0 wt %) and the slurry was equilibrated to pH  $7.0 \pm 0.2$  by small amounts of ammonium hydroxide. Finally, silica powder was filtered and dried in an oven at 120°C for 48 h. This protocol affords about 7 g of mesoporous silica nanoparticles ready for compounding. The obtained shape-controlled silica nanoparticles were labeled SiO<sub>2</sub>-X, where X stands for the aspect ratio of the filler nanoparticles.

Spherical and anisotropic silica nanoparticles have been synthesized by using tetraethylorthosilicate, TEOS, (99%) as the main silica precursor. It was employed a surfactant, cetyltrimethyl-ammonium bromide, CTAB, (98%), acting as a SDA. The control of the shape anisometry was possible by varying the amount of (3-mercaptopropyl)trimethoxysilane, TMSPM (95 %) in the reaction medium as a co-SDA. Milli-Q water with a resistivity  $> 18.2 \text{ M}\Omega\cdot\text{cm}$  was used in order to avoid impurities that may disturb the sol-gel reaction.

### 3.4 Shape-controlled silica nanoparticles characterization

Microscopy techniques operating on different scales give complementary information about the morphology of sol-gel obtained anisotropic silica nanoparticles.

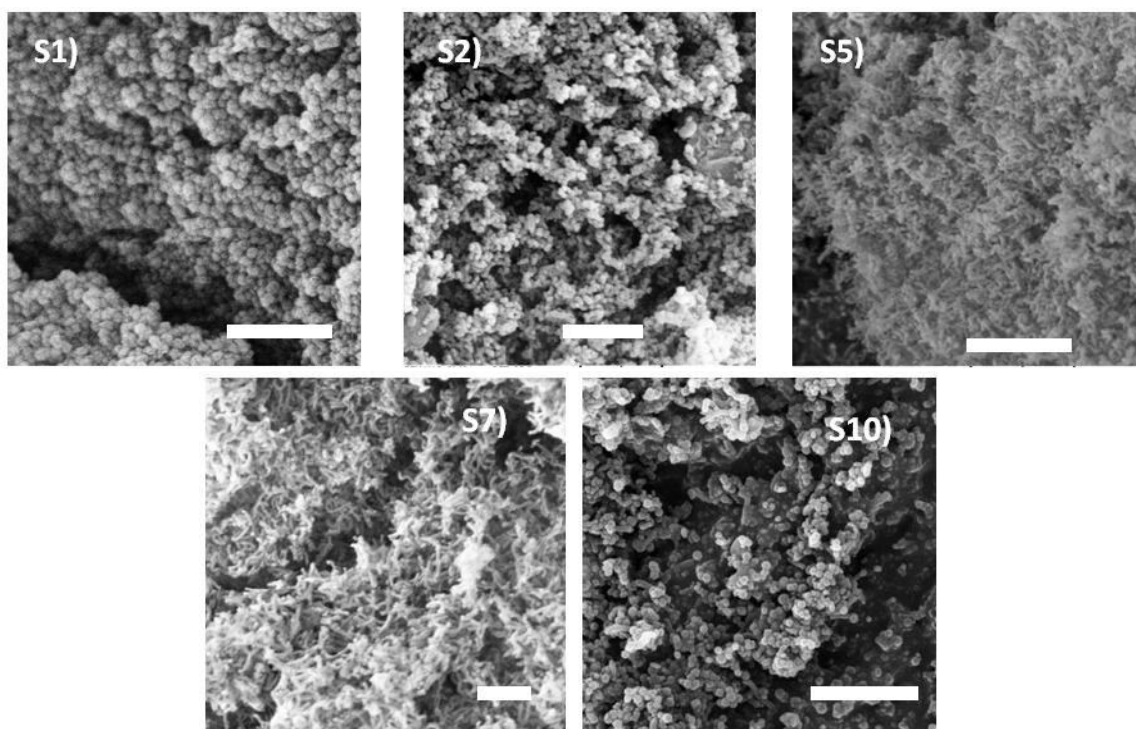


**Figure 3.4:** SEM images of a)  $\text{SiO}_2$ -1; b)  $\text{SiO}_2$ -2; c)  $\text{SiO}_2$ -5; d)  $\text{SiO}_2$ -7 e)  $\text{SiO}_2$ -10 samples. Scales bar are  $1 \mu\text{m}$

SEM images (figure 3.4) allows to evaluate qualitatively the shape distribution in a wide range of nanoparticles examined. In detail,  $\text{SiO}_2$ -1 consist in spherical silica nanoparticles, with diameter always around  $100\text{nm}$ .  $\text{SiO}_2$ -2 particles are all nonshperical, while in  $\text{SiO}_2$ -5 and  $\text{SiO}_2$ -7 particles are clearly rod-like. As regards  $\text{SiO}_2$ -10, the sample is constituted mainly by spherical particles and just by a small amount of rod-like particle.

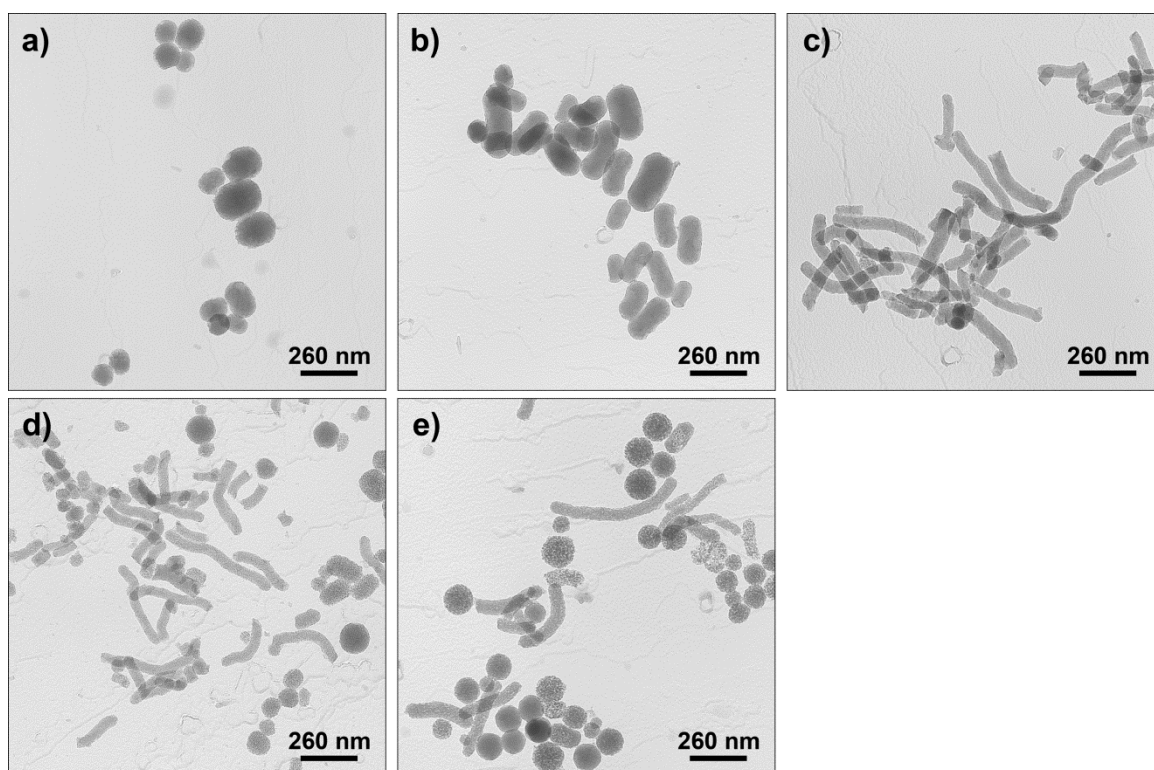


**Figure 3.5:** TEM images of a) SiO<sub>2</sub>-1; b) SiO<sub>2</sub>-2; c) SiO<sub>2</sub>-5; d) SiO<sub>2</sub>-7 e) SiO<sub>2</sub>-10 samples.

Images at higher resolution than SEM were obtained by Transmission Electron Microscopy on silica nanoparticles. TEM images of SiO<sub>2</sub>-X (Fig. 3.5) show that silica NPs are spherical or rod-like shaped, and that their aspect ratio depends on MPTSM/TEOS molar ratio. TEM microscopy also allows to precisely determine the nanoparticle aspect ratio, averaging the image analysis on a selected number of particles in a certain sample. From TEM images in figure 3.5, SiO<sub>2</sub>-1 particles are mainly spherical with  $\sim 80$  nm diameter or slightly elongated with cross section  $\sim 80$  nm and  $120 \pm 20$  nm length (Figure 3.5 a). SiO<sub>2</sub>-2 samples (Figure 3.5 b) exhibit elongated particles. The cross section of the rods is  $80 \pm 10$  nm, equal to SiO<sub>2</sub>-1, while the longest dimension is  $200 \pm 40$  nm (aspect ratio, AR,  $\sim 2.5$ ). Accordingly, SiO<sub>2</sub>-5 particles (Figure 3.5 c) and SiO<sub>2</sub>-7 (Figure 3.5 d) are rod-like shaped with  $70 \pm 10$  nm cross section,  $380 \pm 80$  nm (AR  $\sim 5$ ) and  $480 \pm 100$  nm (AR  $\sim 7$ ) length, respectively.

As regards SiO<sub>2</sub>-10 the TEM image (Figure 3.5 e) shows a mixture of spherical particles with larger diameter (100 - 150 nm) and a minor amount of rod-like particles with AR  $\sim 10$ . This particular morphology already evidenced in SEM investigations is due to the fact that when the MPTSM/TEOS ratio becomes  $> 0.15$ , the shape control is lost.

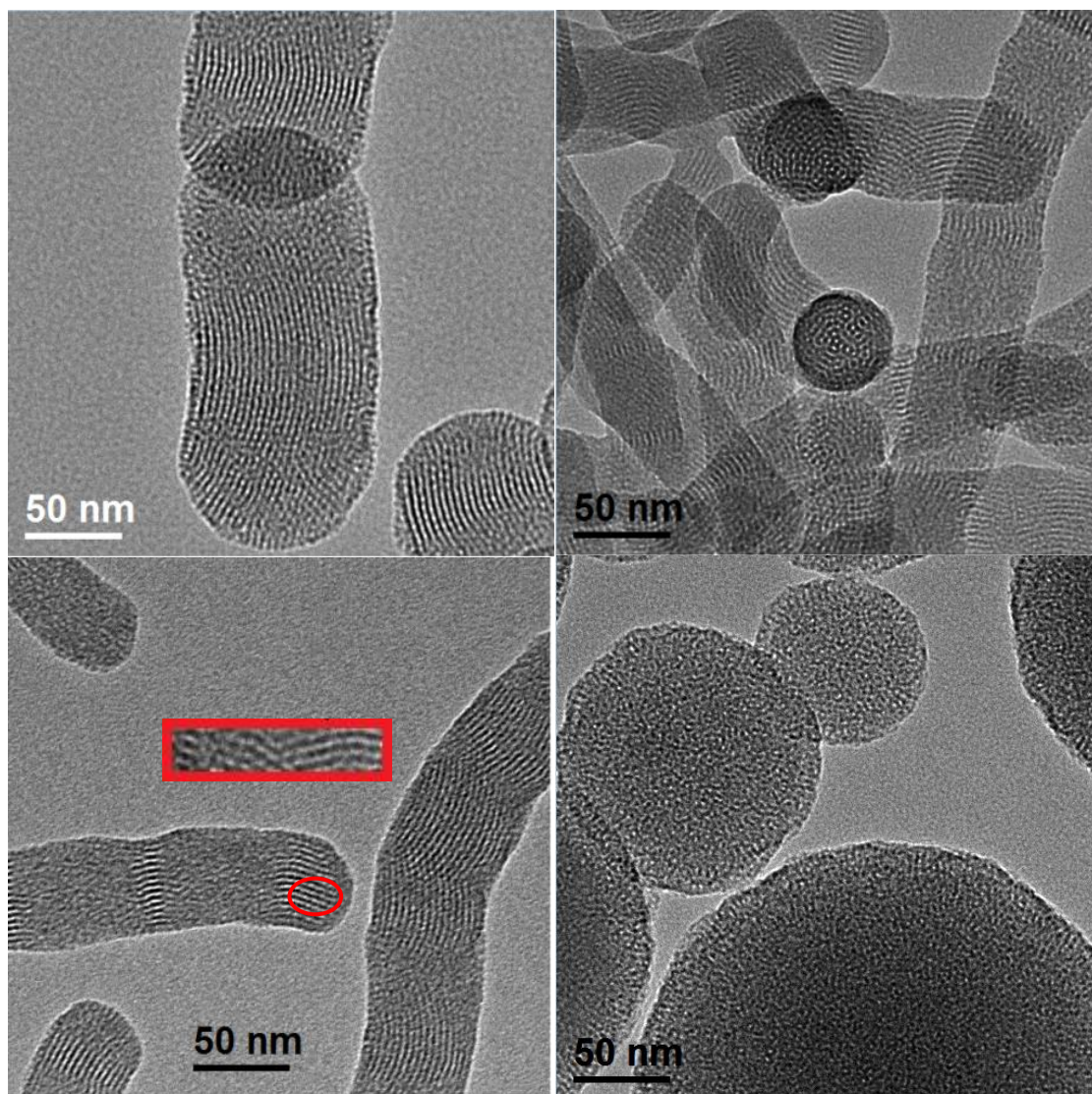


**Figure 3.6:** HR TEM images of SiO<sub>2</sub>-2 (a), SiO<sub>2</sub>-5 (b), SiO<sub>2</sub>-7 (c) SiO<sub>2</sub>-10 (d).

Finally, HRTEM in figure 3.6 images show the internal structure of the anisotropic silica nanoparticles, which is the witness of the silica growth mechanism in this micellar system. As shown by HRTEM images, samples SiO<sub>2</sub>-2 (a), SiO<sub>2</sub>-5 (b), SiO<sub>2</sub>-7 (c) show ordered mesoporous channel structure of few nanometers diameter, generated by the self assembled CTAB, around which silica particles grow assisted by TMSPM. The appearance of periodical lattice fringes (inset of fig. c) along the rods indicates the presence of helical channels inside the rods<sup>13</sup>. Conversely, spherical nanoparticles formed by TMSPM excess in SiO<sub>2</sub>-7 and particularly SiO<sub>2</sub>-10 (d) does not possess any periodicity.

Actually, the formation of spherical nanoparticles without orientation of the mesoporous channel was already observed at high concentrations of MPTMS as a co-SDA, and it was interpreted as a result of an increase of electrostatic repulsive force, as the CTAB micelles are increasingly

surrounded by MPTMS. This would trigger a random disposition of the tubular micelles, which results in a complete loss of the shape control.

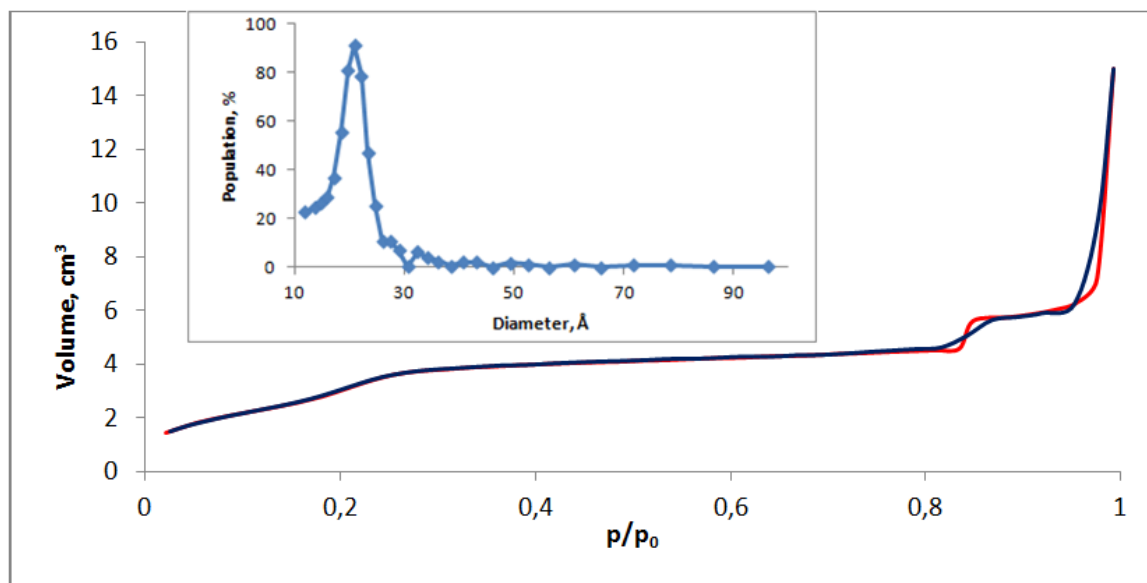


**Figure 3.7:** N<sub>2</sub> adsorption-desorption analysis of SiO<sub>2</sub>-5. The inset represent the pore size distribution

The N<sub>2</sub> adsorption-desorption isotherm of SiO<sub>2</sub>-X confirmed that all powders are mesoporous, with a type IV isotherm. The adsorption-desorption curve and the pore distribution is reported for SiO<sub>2</sub>-5 as an example in Figure 3.7.

The mesopores have an average diameter of ~ 2 nm and the specific surface area (SSA) is very large due to high mesoporosity of silica samples. Nonetheless, external surface area values ( $S_{\text{ext}}$ ) are much lower and similar between different powders. They were estimated from the values of density, Specific Surface Area (SSA) and Desorption Cumulative Pore Volume DCPV, modeling the shapes of SiO<sub>2</sub>-X as perfect spheres or cylinders with dimensions (main cross section and length) obtained by TEM observations. These values are reported in table 3.1

	SSA [m <sup>2</sup> /g]	DCPV [cm <sup>3</sup> /g]	$S_{\text{ext}}$ [m <sup>2</sup> /g]	Density [g/cm <sup>3</sup> ]
SiO <sub>2</sub> -1	1107	1.54	159	1.74
SiO <sub>2</sub> -2	949	1.21	140	1.72
SiO <sub>2</sub> -5	1336	2.52	170	1.70
SiO <sub>2</sub> -7	1434	3.61	224	1.70
SiO <sub>2</sub> -10	1571	3.43	n.d.	1.70

**Table 3.1:** Characteristics of silica nanoparticles



Through elemental analysis it was possible to confirm that the amount of mercaptosilane present in the silica nanoparticles is close to the nominal value. Values of sulphur amount are reported in table 3.2.

	SiO <sub>2</sub> -1	SiO <sub>2</sub> -2	SiO <sub>2</sub> -5	SiO <sub>2</sub> -7	SiO <sub>2</sub> -10
Amount of S [wt%]	0.00	2.08	3.78	4.87	5.20

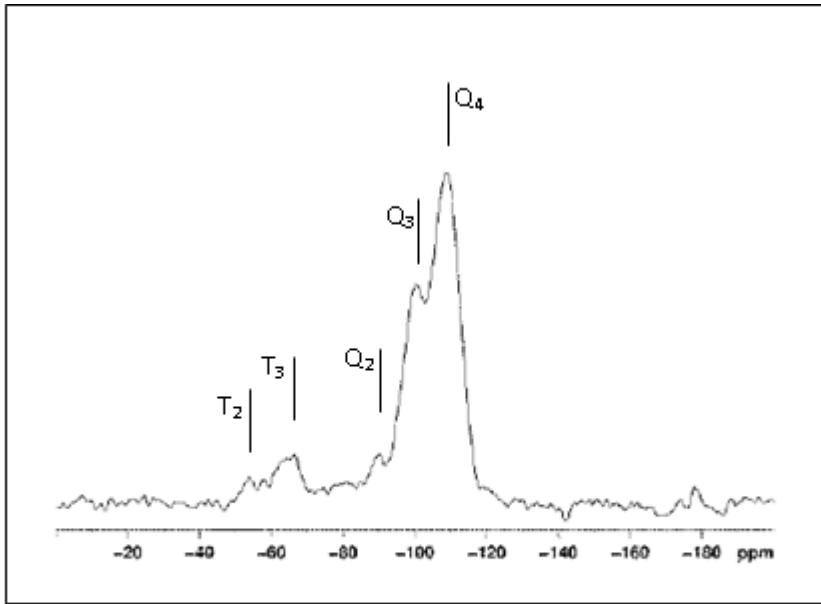
**Table 3.2:** Sulfur content of silica nanoparticles

The condensation degree of silicon atoms was verified with solid state CP MAS NMR of the <sup>29</sup>Si nuclei. The <sup>29</sup>Si CP MAS NMR analysis was performed on SiO<sub>2</sub>-X to measure the condensation degree of the silica.

Figure 3.8 of <sup>29</sup>Si NMR spectrum of SiO<sub>2</sub>-5 is shown as an example; chemical shifts, their assignments and the percentage of every species were therein reported. The degree of condensation (DOC) was calculated according the following equation<sup>14</sup>:

$$(1) \quad DOC = \frac{\sum_i^4 iQ_i + \sum_j^3 jT_j}{4\sum_i^4 Q_i + 3\sum_j^3 T_j} \times 100$$

where Q<sub>i</sub> stands for tetrafunctional SiO<sub>i</sub> units and T<sub>j</sub> for trifunctional SiCO<sub>j</sub> units where i (1-4) and j (1-3) are the number of the oxo-bridges. The DOC value is ~ 88 % for all SiO<sub>2</sub>-X samples, in the range of the sol-gel amorphous silica with low density (see table)<sup>15</sup>. The presence of T<sub>j</sub> centers is due to the alkyl chains of the MPTMS precursor.



Si unit	T2	T3	Q2	Q3	Q4	DOC, %
$\delta$ (ppm)	-55.0	-64.8	-90.0	-100.0	-109.0	88,1
A %	3,4	8,2	6,1	30,7	51,6	

**Figure 3.8:**  $^{29}\text{Si}$  NMR spectrum of  $\text{SiO}_2$ -5 sample. The chemical shifts, the assignments and the percentage of every species calculated by the signal deconvolution are reported in the table.

### 3.5 Shape controlled silica/SBR nanocomposites preparation and curing

Nanocomposites of SBR and shape-controlled anisotropic silica particles were obtained by mechanical mixing. In the tire industry, internal mixers and two-rolling mills are the preferred solutions according to the mixing requirements, see figure 3.9.

In internal mixers, two twins screws rotate counterwise inside an enclosure chamber, which on the top has a ram that apply a certain pressure on the mixing formulate. The addition of ingredients is executed by raising the ram, and effective mixing occurs just when the ram is applying pressure; some advantage of the internal mixer are the possibility of applying a broad range of temperatures and to achieve good mixing in a shorter time and with a lower amount of volatile organic compounds (VOCs) released in atmosphere than two-rolling mill. Conversely, two-rolling mill is more indicated for low-temperature mixing stages (for example the introduction of curatives) and allows to obtain good homogeneity of the final material.

Particularly for nanofillers, mixing conditions are crucial for obtaining the desired materials properties: first, shearing forces should be enough to break

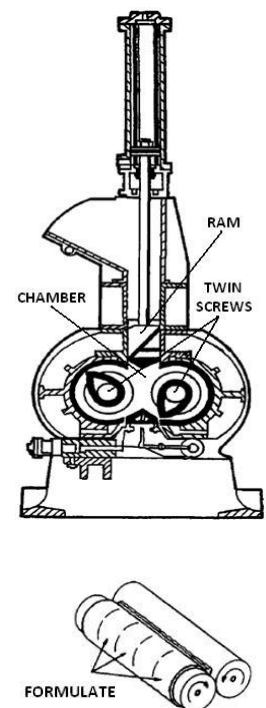


**Figure 3.9:** Mixers used in rubber industry

down the particle agglomerates. In the case of silica, the control of temperature and time allows for a complete compatibilization with silane coupling agents of the hydrophilic oxide surface; in fact, silica is typically added in an internal mixer step.

In the compounding recipes we used: styrene butadiene rubber, SLR 4630 from Styron Europe GmbH. Bis (3-triethoxysilylpropyl) disulfide, TESPD, was purchased from Aldrich; this coupling agent is able to react with silica surface during compounding, thus favouring nanoparticle distribution throughout the matrix. Furthermore, it can react with rubber double bonds

during vulcanization creating sulphur-carbon bonds and improving the filler-rubber interaction. N,phenyl-N'-alkyl-p-phenyldiamine, 6 PPD, used as an antidegradant was Santoflex-6 PPD from Flexsys; stearic acid was Stearina TP8 from Undesa; sulphur was S<sub>8</sub> (soluble sulphur) from Zolfoindustria; zinc oxide was from Zincol Ossidi; N-cycloesil-2-benzothiazole sulfenamide, CBS, was Vulkacit CZ/C from Lanxess.

Ex-situ synthesis of nanocomposites was performed by blending technique in an internal twin-screw mixer for incorporating the shape-controlled silica nanoparticles in styrene-butadiene rubber matrix. The technique is well-known in the tire industry and described in various ASTM standards for preparation of rubber nanocomposites for tire application (for example, D 3188, D 3185 1A, ecc.). The whole procedure is separated in three mixing steps at different temperature, according to the thermal stability of the ingredient: for example, silane coupling agents and silica are mixed in the high temperature step, in order to obtain complete silica surface functionalization, while curatives must be added in the low temperature step to avoid premature vulcanization.

In the first step, rubber is masticated at 140°C and 60 rpm twin screw speed, then silica nanoparticles are included in three subsequent aliquots together with the silane. The same was for preparations of composites containing a mixture of fillers of different shape. The liquid silane coupling agent TESPD was deposited on the first fraction of silica prior to addition in rubber. Two minutes after the last silica addition 6PPD, Zinc oxide and stearic acid are added; this lag time avoids secondary reaction between ZnO with silica silanols<sup>16</sup>. The amounts of compounding ingredients are listed in table 3.3a and expressed in phr (parts per hundred rubber).

Event	Elapsed time
Mastication of SBR rubber	0 min
Addition of 1/3 of silica and TESPD	1 min
Addition of 1/3 of silica	1 min 30"
Addition of 1/3 of silica	2 min
Addition of ZnO, stearic acid and 6PPD	4 min
Unload	6 min

Event	Elapsed time
Mastication material from stage 1	0 min
Addition of CBS and sulfur	1 min
Unload	3 min

**Table 3.4** compounding method of SBR-SX-W nanocomposites

In the second step, the material obtained in stage 1 is reloaded in the internal mixer operating at 90°C at 60 rpm. CBS and sulfur are then added and mixed for 2 minutes (table 3.3b). The obtained material is finally processed in a two-rolling mill as a third step at 50°C for 3' to improve filler distribution in the sample.




Ingredients	Amount (phr)
S-SBR	100
Ex situ-SiO <sub>2</sub>	45-35-25-12
TESPD	3,6-2,8-2-0,96
Stearic acid	0,85
6 PPD	1
ZnO	2,7
Sulfur	2
CBS	1,5

**Table 3.5** compounding receipt of SBR-SX-W nanocomposites

The amounts of ingredients are listed in tab. 3.4 for nanocomposites containing 12, 25, 35 and 45 phr of silica; the silane amount depends on the amounts of silica, while the amount of all the other ingredients is relative to rubber, so it is the same for all the silica concentrations explored. Composites were further molded in a two-roll mill for 2 min to produce sheets of about 2 cm thick, suitable for the vulcanization process. Hereafter uncured nanocomposites are labeled SBR-SX-W.

Cured composites were vulcanized in mould in a hydraulic press at 170°C, under the pressure of 200 bar at their optimum vulcanization time (see curing kinetics in appendix A). The shape of the mould depends on the

dynamo mechanical analysis requested as reported in table 3.6.

Analysis	DMA	Compression Dynamics	Tensile/Mullins
Shape			
Size	2,5 x 54 x 91 mm	1,8 mm x 1,2 mm Ø	ISO 4 - Dumbbell

**Table 3.6:** Shape of vulcanized V-SBR-SX-W samples for dynamo-mechanical tests

In the following cured nanocomposites are called V-SBR-SX-W.

## References

- [1] J. Brinker, G. W. Scherer, *Sol-gel Science: The Physics and Chemistry of Sol-gel Processing*, Gulf Professional Publishing, **1990**
- [2] M. Messori and M. Fiorini, *J. Appl. Polym. Sci.*, **2011**, 119, 3422–3428
- [3] S. Kohjiya and Y. Ikeda, *Rubber Chem. Technol.*, **2000**, 73, 534–550
- [4] R. Scotti, L. Wahba, M. Crippa, M. D'Arienzo, R. Donetti, N. Santo and F. Morazzoni, *Soft Matter*, 2012, **8**, 2131–2143
- [5] L. Wahba, M. D'Arienzo, R. Donetti, T. Hanel, R. Scotti, L. Tadiello and F. Morazzoni, *RSC Advances*, **2013**, 3, 5832
- [6] L. M. Ilharco, M. Pagliaro, *Chem. Rev.* **2013**, 113, 6592–6620
- [7] Sanchez-Ferrer AS, Reufer M, Mezzenga R, Schurtenberger P, Dietsch H. *Nanotechnology* **2010**, 21, 185603
- [8] An GH, Jeong SY, Ahn HJ. *Mater Lett* **2011**, 65, 2377-80
- [9] Choi CS, Yoon JH. *Appl Phys A*, **2012**, 108, 509-13
- [10] J Zhang, M Liu, A Zhang, K Lin, C Song, X Guo, *Solid State Sciences* **2010**, 12, 267–273
- [11] J. Wang, J. Zhang, B. Y. Asoo, G. D. Stucky, *JACS* **2003**, 125, 13966-13967
- [12] S. Sadasivan, D. Khushalani, S. Mann, *J. Mater. Chem.*, **2003**, 13, 1023–1029
- [13] X Du, J He *Dalton Trans.*, **2010**, 39, 9063-9072
- [14] S. Dirè, V. Tagliazucca, E. Callone, A. Quaranta, *Mater. Chem. Phys.* **2011**, 126, 909-917
- [15] V. Gualandris, F. Babonneau, M. Janicke, B. Chmelka, *J. Sol-Gel Sci. Technol.*, **1998**, 12, 75-80
- [16] N. Hewitt, P. Ciullo, *Compounding precipitated silica in elastomers*, William Andrew publishing, Norwick, NY

## **Chapter 4**

# **MORPHOLOGY AND PHYSICO-CHEMICAL PROPERTIES OF SCS/SBR NANOCOMPOSITES**

The chapter reports the morphology and physico-chemical characteristics of SBR nanocomposites containing shape controlled anisotropic NPs with different ARs.

The morphology of the nanocomposites and the topography of the bound rubber were investigated by an integrated approach combining Transmission Electron Microscopy (TEM) and AFM, to visualize the stiffest elastomer zone at the interphase. Bound rubber amounts were measured by swelling experiments on crude samples, while filler immobilization capability was evaluated by swelling experiments on vulcanized samples. Time Domain (TD) NMR experiments allowed to detect either the amount of rubber strongly immobilized at the filler/rubber interface or the polymer chains with higher mobility.

#### **4.1 Morphology of silica/SBR composites by TEM**

The effect of the anisotropy of silica particles on the filler dispersion was investigated by TEM both on uncured SBR-SX-35 and cured V-SBR-SX-35 composites. TEM images show:

- \_ The distribution of silica nanoparticles in the polymeric matrix
- \_ The connectivity between neighboring silica nanoparticles
- \_ The reciprocal position of silica nanoparticles

TEM images of uncured SBR-SX-35 taken at low magnification (figure 4.1) testify the particle distribution in a largest area of the nanocomposites. A continuous network of particles is extended throughout the whole rubber matrix for all the materials with some differences in their distribution.

Indeed in SBR-S1-35 the particle distribution is rather continuous and isotropic, whereas it appears more inhomogeneous by increasing showing some voids, lacking in filler particles. That is, the network is more continuous in samples containing spherical or near spherical particles than in samples with anisotropic particles.

The TEM images at high magnification, reported in Figure 4.2, allowed detailed micro-structural examination.

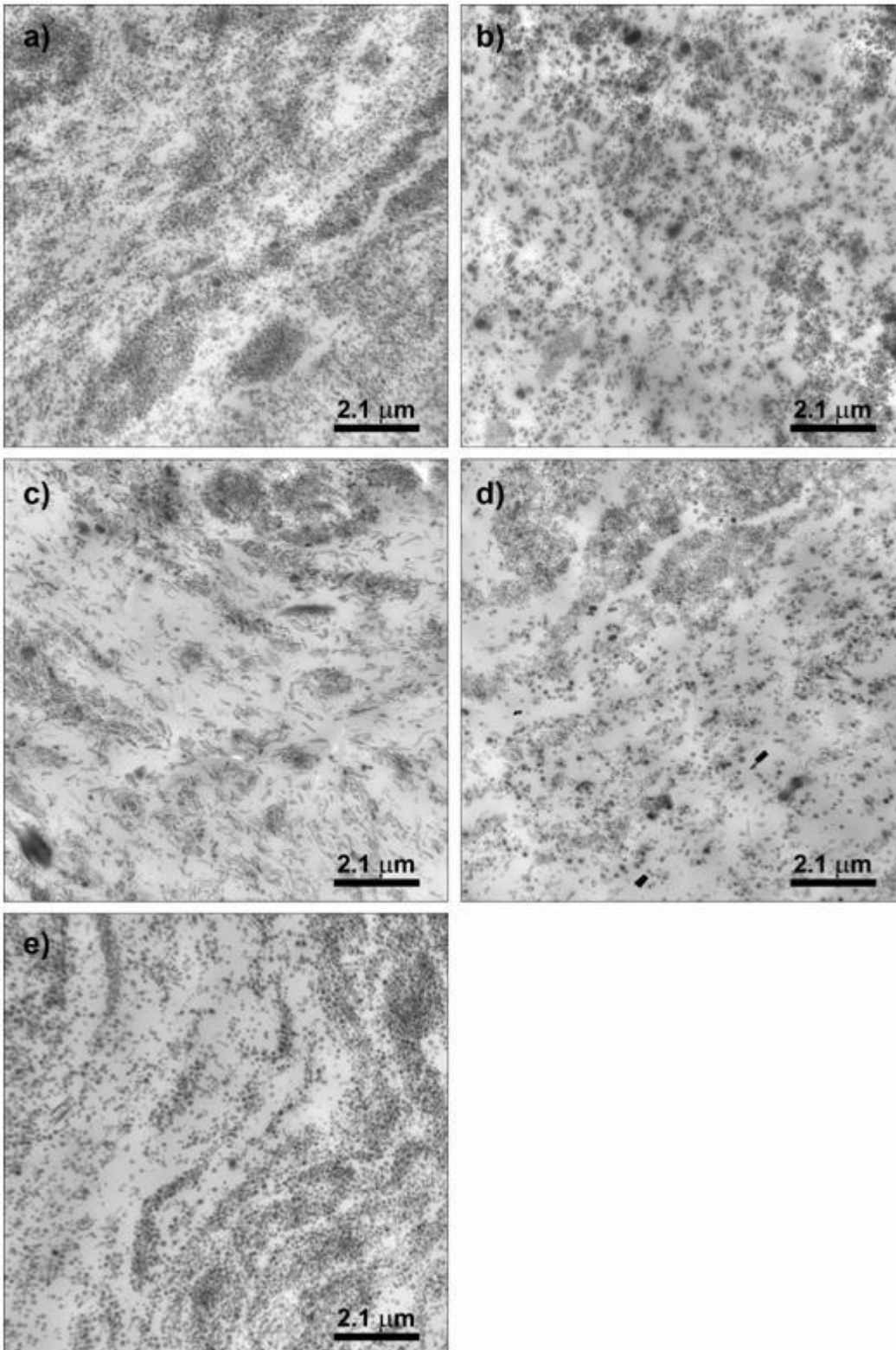


**Figure 4.1:** TEM images at low magnifications of crude SBR-SX-35 composites: a) SBR-S1-35; b) SBR-S2-35; c) SBR-S5-35; d) SBR-S7-35; e) SBR-S10-35



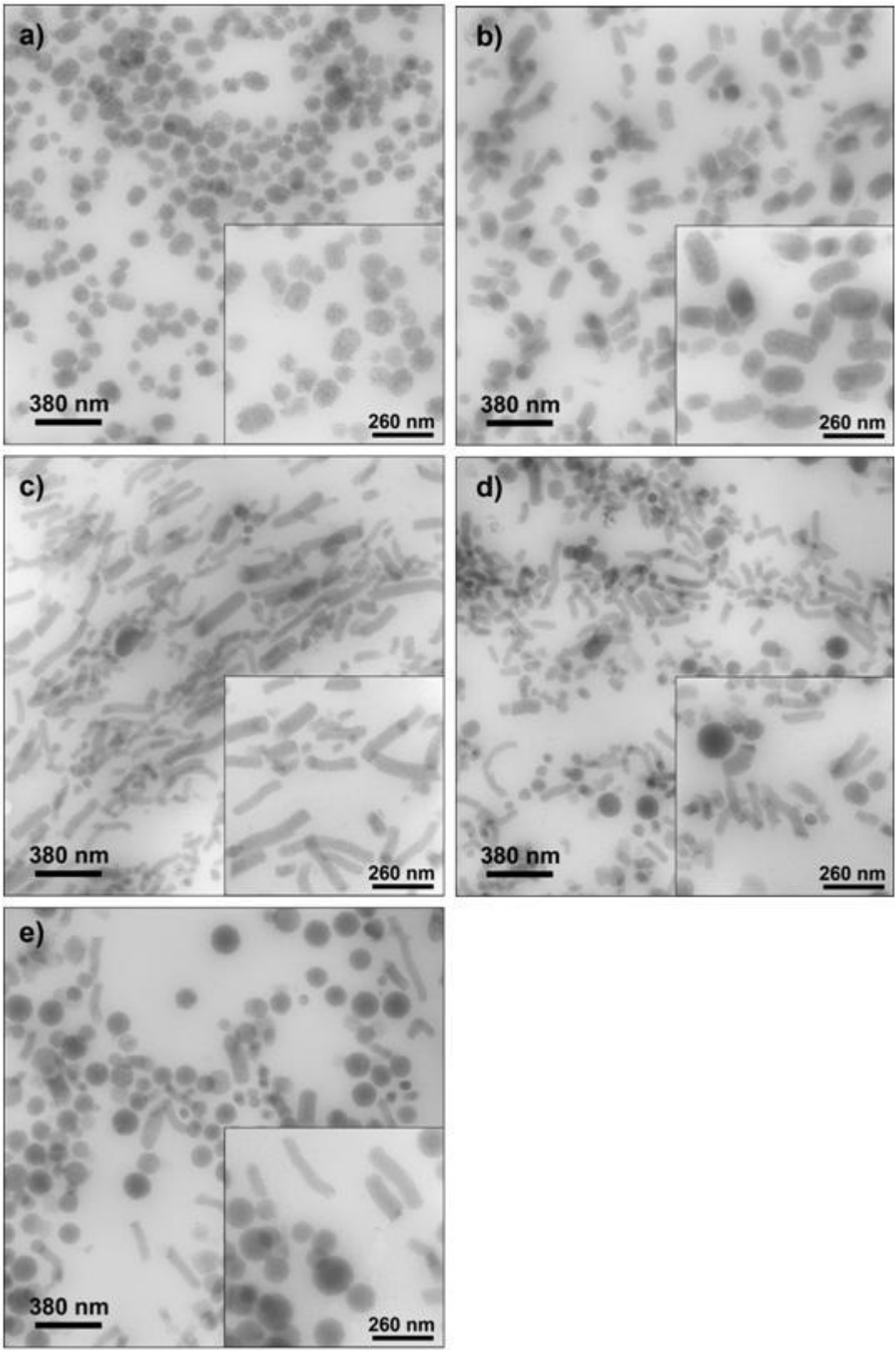


**Figure 4.2:** TEM images at high magnifications of crude SBR-SX-35 composites: a) SBR-S1-35; b) SBR-S2-35; c) SBR-S5-35; d) SBR-S7-35; e) SBR-S10-35.

TEM images of uncured SBR-SX-35 at higher magnification in Figure 4.2 confirm that the shape and the dimensions of silica particles are preserved in nanocomposites after incorporation into the rubber matrix. In all samples silica NPs are separated by a rubber layer which highlights the silica particle dispersion in the matrix, thanks to the use of the compatibilizer TESPd that prevents particles aggregation.

The presence of some shorter and thinner particles in the figures are due to the sectioning of the samples that have undergone TEM analysis. In fact the specimens have a thickness of about 40 nm, so longest particles might be cut in different ways by the cryo-ultramicrotome (see appendix A), according to their orientation. In detail, TEM images of SBR-S1-35 show that the primary particles, spherical or slightly ellipsoidal, with a diameter  $\sim 80$  nm, (Figure 4.2 a), form the very well known string-of-pearls network, in a similar way to commercial spherical silica systems.

In SBR-S2-35 (4.2 b), SBR-S5-35 (4.2 c) and SBR-S7-35 (4.2 d) the anisotropic rod-like particles still form a continuous network throughout the matrix. However, it is noteworthy that when the particles length increases, a preferential alignment along their main axis occurs. This effect is more evident for the longest rods in SBR-S5-35 and SBR-S7-35 ( $AR > 2$ ), while it is less marked in SBR-S2-35. Anisotropic particle alignment is diffuse in the whole rubber matrix; nevertheless, particles are not oriented in only one direction, but oriented domains of self-assembled particles are randomly distributed. It is remarkable to note that this particle organization occurs in spite of the mixing process used to obtain the composites and though no external or internal procedure was performed to drive the particle arrangement<sup>1</sup>. A possible explanation can be the larger organic/inorganic interface exhibited by the single rod-like nanoparticles, compared to spherical or slightly anisotropic particles, which induces the formation of aggregates with extended regions of entrapped rubber between particles aligned along the main axis.

Conversely, TEM images of SBR-S10-35. (4.2 e) show the aggregation of large spherical particles of 150 - 200 nm of diameter with a small amount of elongated rods having  $\sim 650$  nm length. Moreover, a continuous network of particles bridged by thin rubber layer formed also in this case but no preferential orientation of the anisotropic particles is found, probably because of the high amount of spherical particles in the mixture.

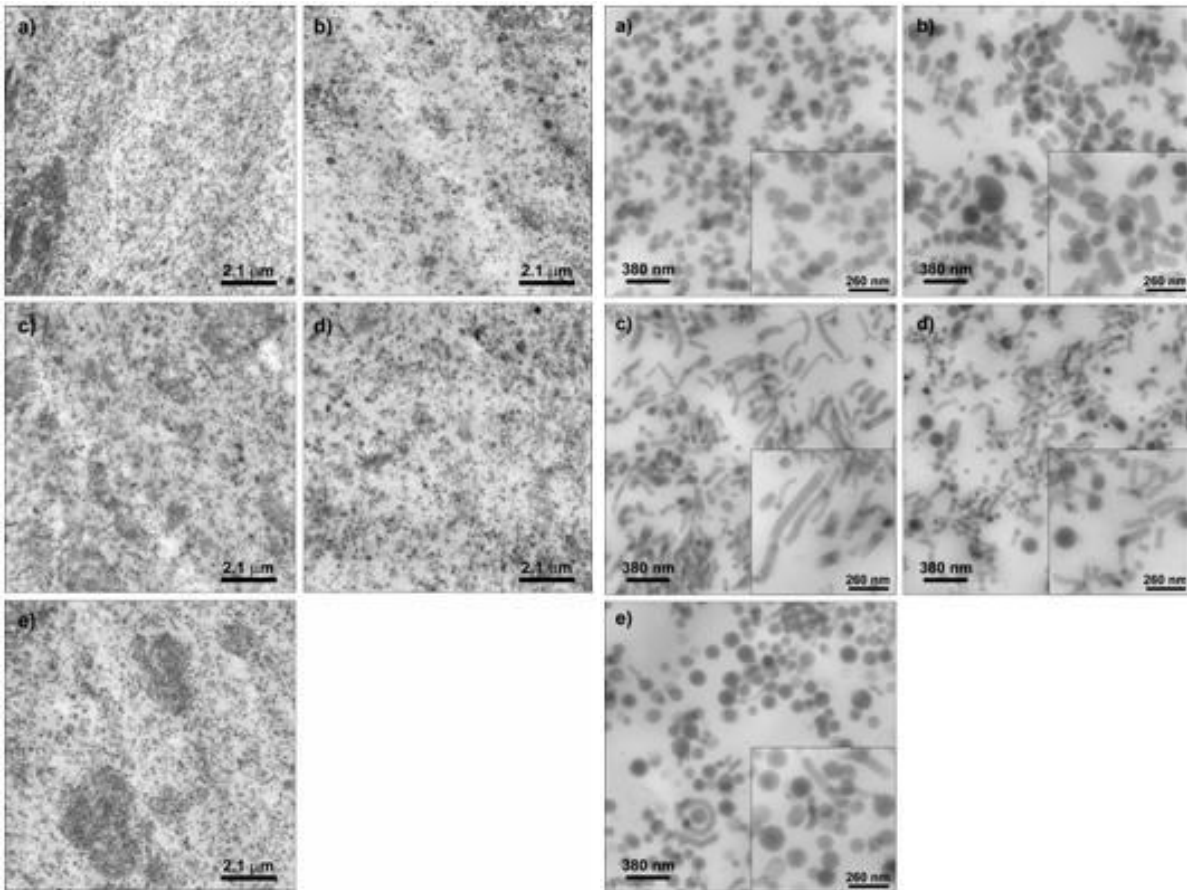


**Figure 4.3:** TEM images at high magnifications of cured V-SBR-SX-35 composites: a), a') V-SBR-S1-35; b), b') V-SBR-S2-35; c), c') V-SBR-S5-35; d), d') V-SBR-S7-35; e) e') V-SBR-S10-35.

Representative TEM images of the cured composites V-SBR-SX-35 taken at different magnification are shown in Figures 4.3. A better filler dispersion compared to uncured composites is evidenced in all the dimensional scales examined, probably as a consequence of the further mixing steps necessary for introducing the vulcanization agents. Anyway, the TEM images confirm the ability of the longest nanorods of V-SBR-S5-35 and V-SBR-S7-35 to form a network of partially aligned particles bridged by rubber layers. Moreover, the network structure do not show remarkable differences compared to the corresponding uncured samples SBR-SX-W.

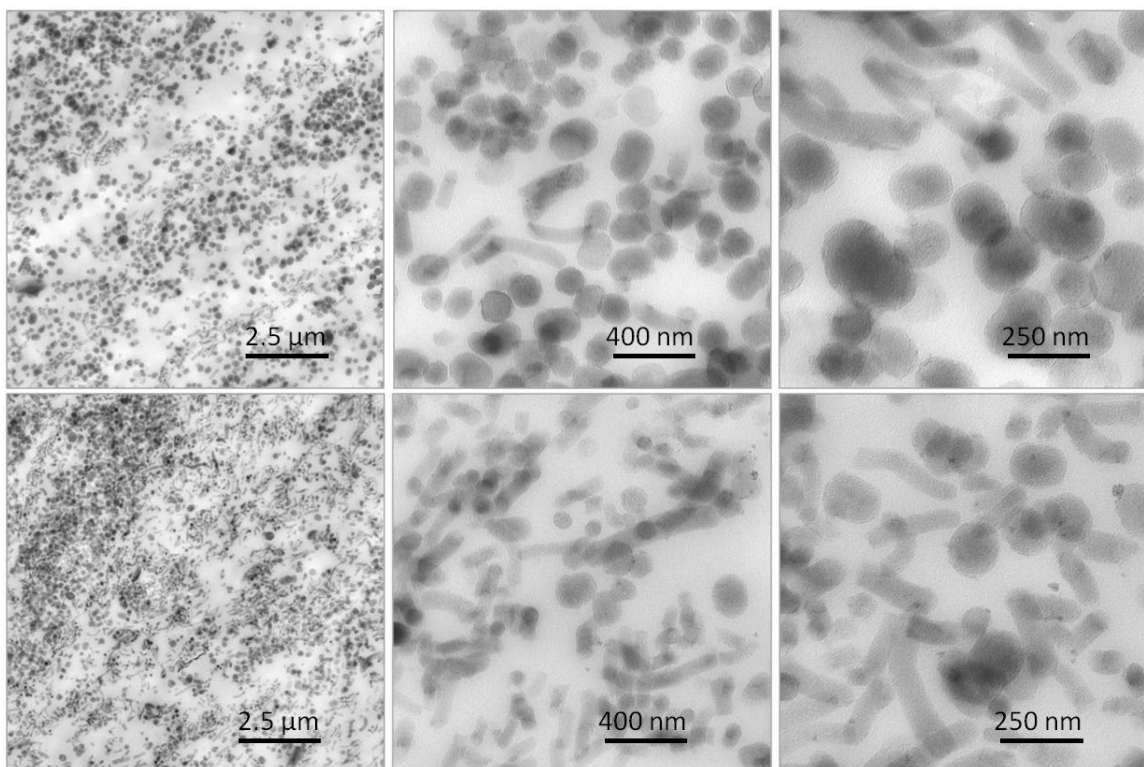


**Figure 4.4:** TEM images at different magnifications of cured V-SBR-MA-35 (a, b, c) and V-SBR-MD-35 composites (d, e, f).

TEM images at low magnification of cured V-SBR-MA-35 (a) and V-SBR-MD-35 (d) testify the continuous particles network extended throughout the whole rubber matrix, in both cases evenly distributed. TEM images at higher magnification of V-SBR-MA-35 (b, c) and V-SBR-MD-35 (e, f) confirm that the shape and the dimensions of silica particles are preserved in nanocomposites after incorporation into the rubber matrix. As in pure-shape nanocomposites, silica NPs are separated by a rubber layer which highlights the silica particle dispersion in the matrix, thanks to the TESP that prevents particles aggregation. Anisotropic SiO<sub>2</sub>-S5 silica nanoparticle alignment is much reduced for both samples, with respect to V-SBR-S5-35. Both with dominant presence of SiO<sub>2</sub>-S1 (V-SBR-MA-35) and of SiO<sub>2</sub>-S5 (V-SBR-MD-35) in the filler mixture, anisotropic particle alignment is hindered by the presence of spherical particles, that are often separating anisotropic particles domains. It can be concluded that the presence of a dual-shape filler system (SiO<sub>2</sub>-S1 and SiO<sub>2</sub>-S5) results in the formation of an hybrid network regardless the ratio between the differently shaped nanoparticles, which is expected to further enhance the rubber immobilization.

#### 4.2 Heterogeneities detection in silica/SBR composites by AFM

The nanocomposite morphology related to the rubber/particle interphase were investigated by AFM

operating in tapping mode in air. The analysis was performed on fresh surfaces after freeze-fracturing the materials. First, AFM imaging is a surface technique and the freeze-fractured specimen preparation causes the longest silica particles to be cut, lowering the probability that high AR silica particles completely lie on the fractured surface. This actually represents a useful tool to evidence morphological characteristics not accessible by TEM on cryo-cut nanocomposites. Not only conventional height images but also amplitude error images were used, because the amplitude error originates from the vertical deflection of the AFM tip, that shows sharper contrast at the edges of materials heterogeneities than height signal.

V-SBR-S1-35 3D image (Figure 4.5 a) shows homogeneous dispersion of particles, with small contact zone between the neighbor particles. This distribution is similar to that reported in the literature for spherical silica particles in rubber nanocomposites and described as string-of-pearls<sup>2</sup>. 2D amplitude error image (Figure 4.5 a') evidences well distinguishable rubber layers around particles, slightly overlapping at the particle contact points.

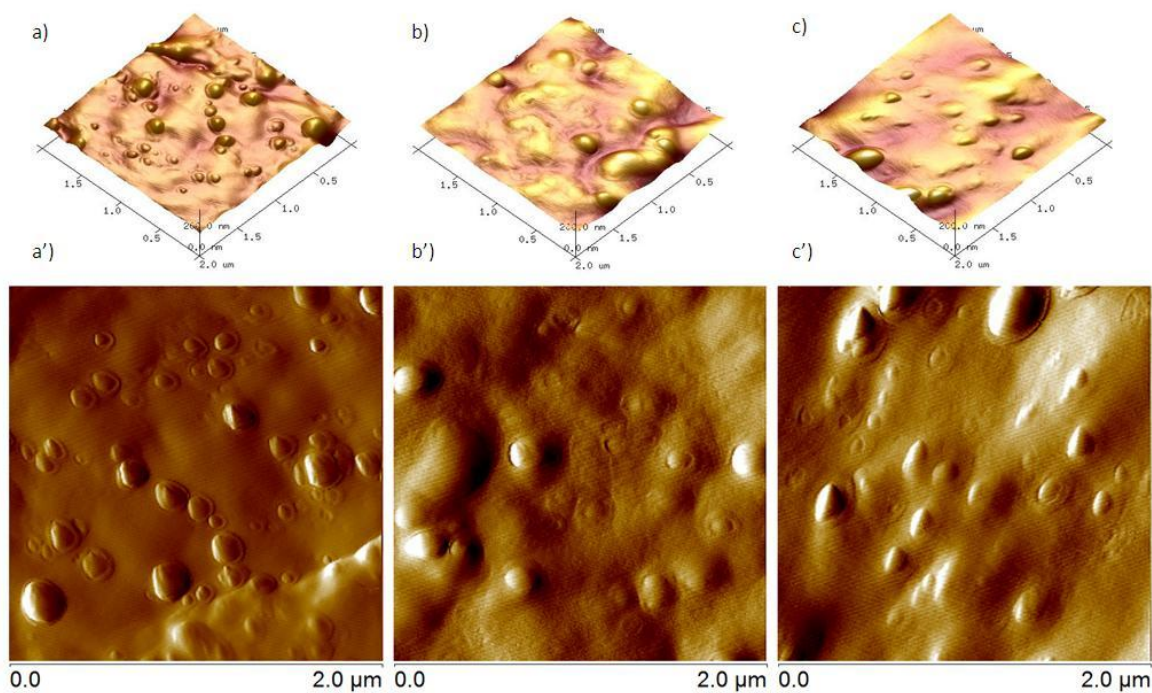


**Figure 4.5.** 3D height (up) and 2D amplitude error (down) AFM images of a, a') V-SBR-S1-35; b, b') V-SBR-S2-35; c, c') V-SBR-S5-35 nanocomposites.

In the case of V-SBR-S2-35 and, mainly, V-SBR-S5-35, 3D images show less homogeneous particle dispersion (Figure 4.5b and 4.5c). Most silica particles are aggregated, showing rubber lacking zones. The aggregates are differently shaped and their image corresponds to the cross-section of the aligned anisotropic particle domains previously described by TEM, as shown in the schematic model of Figure 4.6.

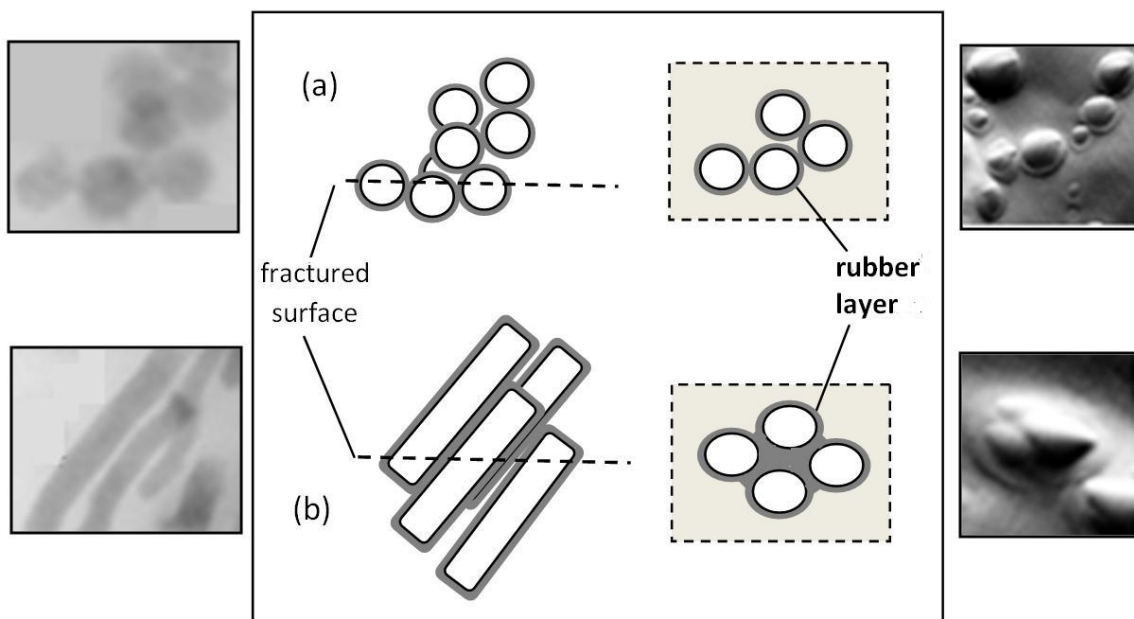


**Figure 4.6.** Model representing the self-assembly of differently shaped particles and the corresponding fractured surfaces in (a) V-SBR-S1-35 loaded with spherical particles and (b) V-SBR-S5-35 loaded with rod-like particles (AR=5). The models are compared with significant TEM (left) and 2D AFM (right) images of the same samples.

Amplitude error images of V-SBR-S2-35 and V-SBR-S5-35 (Figure 4.5 b' and c') show rubber layers completely surrounding both the particle aggregates and the residual single particles in the matrix. Moreover, the aligned anisotropic particles share the rubber layers and in addition entrap a larger amount of rubber in the particle domains than the spherical ones do (Figure 4.6). From these observations, it seems that the particle alignment favors an enlargement of the immobilized rubber region.

In order to evaluate the thickness of the rubber layer surrounding silica particles, AFM phase images of nanocomposites were recorded. The phase signal is related to the energy dissipated by the tapping tip while scanning the surface, and gives information at the nanometric scale about the size and the shape of local rubber heterogeneities, identifying regions with different stiffness<sup>3</sup>. According to recent studies<sup>4</sup>, the thickness of the rubber layer surrounding isolated silica particles can be measured by the difference between the particle section detected in the phase images and that which is measured in the height images.

Height and phase images of V-SBR-SX-35 are reported in figure 4.7. For isolated nanoparticles the rubber heterogeneous layer thickness ( $T_r$ ) can be calculated by the expression<sup>4</sup>:

$$(1) \quad T_r = \frac{W_{Ph} - W_{He}}{2}$$

where  $W_{Ph}$  and  $W_{He}$  are the particle section widths from phase and height image, respectively, as

indicated by the insets in Figure 4.6 (Values are reported in Table 4.1 ). For all samples the layer thickness resulted  $15 \pm 5$  nm, irrespective of the different SX particle shapes.

The volume of heterogeneous rubber in the layers surrounding isolated silica particles can be roughly estimated by modeling the shapes of  $\text{SiO}_2\text{-X}$  as perfect spheres or cylinders having dimensions (main cross section and length) obtained by TEM observations. The volume resulted  $32 \pm 12\%$  of the total rubber for S1,  $28 \pm 11\%$  for S2 and  $25 \pm 9\%$  for S5, slightly dependent on the particle shape. This suggests that the larger amount of rubber immobilized in the domains of the anisotropic silica NPs, evidenced by the AFM images (Figures 4.5 and 4.6), cannot be related to the shape of the isolated particles, but it results from the alignment of the rod-like particles. No direct indications about the different mobility of the rubber chains and, consequently, about the nature of the rubber interactions can be directly obtained by AFM images. They will be investigated and discussed in Time Domain NMR paragraph (4.4).

V-SBR-S1-35			V-SBR-S2-35			V-SBR-S5-35		
149	180	15	63	94	15	125	157	16
143	173	15	63	99	18	134	162	14
127	155	16	64	90	13	174	215	20

**Table 4.1:** Particles widths from height  $W_{He}$  and phase  $W_{Ph}$  images and calculated rubber layer thickness  $T_r$ .

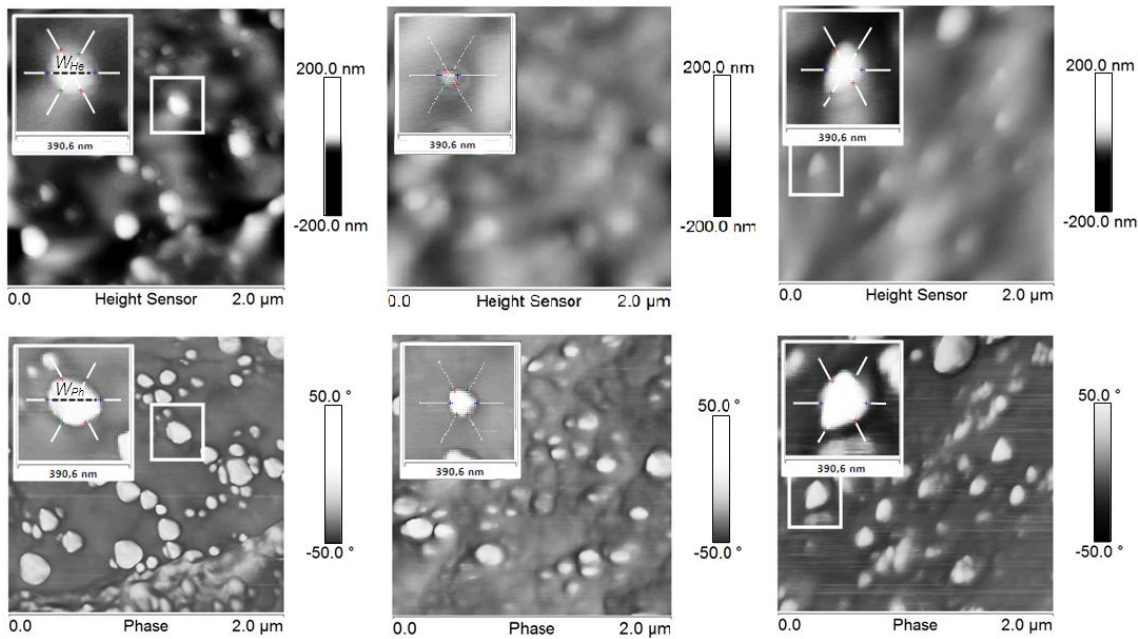


**Figure 4.7.** Height and phase images of a, a') V-SBR-S1-35, b, b') V-SBR-S2-35 and c, c') V-SBR-S5-35 freeze-broken surfaces. The insets represent the image analysis of isolated NPs. Particle width from phase ( $W_{Ph}$ ) and height ( $W_{He}$ ) images are indicated.

### **4.3 Physico-chemical properties of rubber nanocomposites**

#### **4.3.1 Thermogravimetric analysis: effective filler introduction**

TGA analysis were conducted on uncured SBR-SX-35 nanocomposites to verify the effective filler insertion in rubber, hence confirming the comparison of nanocomposites with same silica loading differing only by nanoparticle shape. An oxidative gas flow was used as reported in appendix A.

Weight losses in the high temperature range (200-1000°C) are in accordance with the complete oxidation of the organic components of the nanocomposites. The residual at 1000°C accounts for the 22.1%, 22.5% and 23.2% of the dry weight respectively in V-SBR-S1-35, V-SBR-S2-35 and V-SBR-S5-35, in good accordance with the original silica loading (35 phr), considering also the degradation of filler surface functionalities (silanols, TESPD, ecc.).

#### **4.3.2 Swelling experiments**

Solvent extraction experiments were performed on uncured SBR-SX-35 samples to estimate the amount of rubber immobilized inside and around the nanoparticles domains. Extractable fractions (f%) and bound rubber ( $B_r$ %) calculated according to method described in appendix A are reported in Table 4.2 for SBR-SX-35 samples. The results demonstrate that in all uncured composites a large amount of rubber is significantly immobilized. Furthermore, this amount increases by increasing the shape factor of the silica particles and is highly marked in composites containing elongated NPs, as evidenced by the decrease of the f value and the increase of  $B_r$ %. The high percentage of bound rubber is indicative of a high interaction with silica and is related to a high degree of reinforcement by the filler<sup>5</sup>. Measurements were not possible on nanocomposites with lower filler amounts (SBR-SX-25 and SBR-SX-12) because they disgregate in the presence of solvent: this is related to the lack of a filler network diffuse throughout the whole material<sup>5</sup>.



Swelling experiments were performed also on cured V-SBR-W-SX samples to obtain indications about the filler capability of immobilized rubber. The absolute swelling ratios ( ) and the equilibrium swelling ratios of the rubber phase ( ) of V-SBR-SX-W nanocomposites were calculated according to equations in appendix A and are reported in Table 4.3.

	SBR-S1-35	SBR-S2-35	SBR-S5-35
f %	62.6	55.7	56.0
B <sub>r</sub> %	15.5	24.8	24.4

**Table 4.2:** Extractable and bound rubber fractions of SBR-SX-35 from swelling measurements on crude composites

The f % values are much lower than for uncured samples because of the crosslinking provided by the vulcanization process, that hinders rubber dissolution in toluene. In fact, swelling data on cured nanocomposite do not allow direct calculation of the bound rubber amount, but allow to estimate the filler immobilization capability according to the swelling ratios. In fact, according to the Kraus methodology for treating swelling measurement of nanocomposites containing different nanofillers, at increasing filler amount the restriction imposed by the filler to rubber increase<sup>6</sup>. The extent to which this increase takes place can be related to a parameter *c* that depends only on the nature of filler. Parameter *c* can be calculated by the slope of the straight line obtained from the plot of  $Q_r/Q_{r0}$  against  $\frac{\Phi}{1-\Phi}$ .

**Table 4.3:** Extractable fraction, absolute and relative swelling ratios of V-SBR-SX-W nanocomposites.

	V-SBR-S1-12	V-SBR-S2-12	V-SBR-S5-12	V-SBR-S1-25	V-SBR-S2-25	V-SBR-S5-25	V-SBR-S1-35	V-SBR-S2-35	V-SBR-S5-35
$Q$	5,08	5,97	8,83	4,90	4,46	6,78	4,12	4,12	3,88
$Q_r$	5,32	6,28	9,33	5,43	4,93	7,57	4,75	4,76	4,46
$Q_r/Q_{r0}$	0,547	0,643	0,951	0,528	0,481	0,730	0,443	0,444	0,418
f %	22	21	23	19	17	13	8	7	8

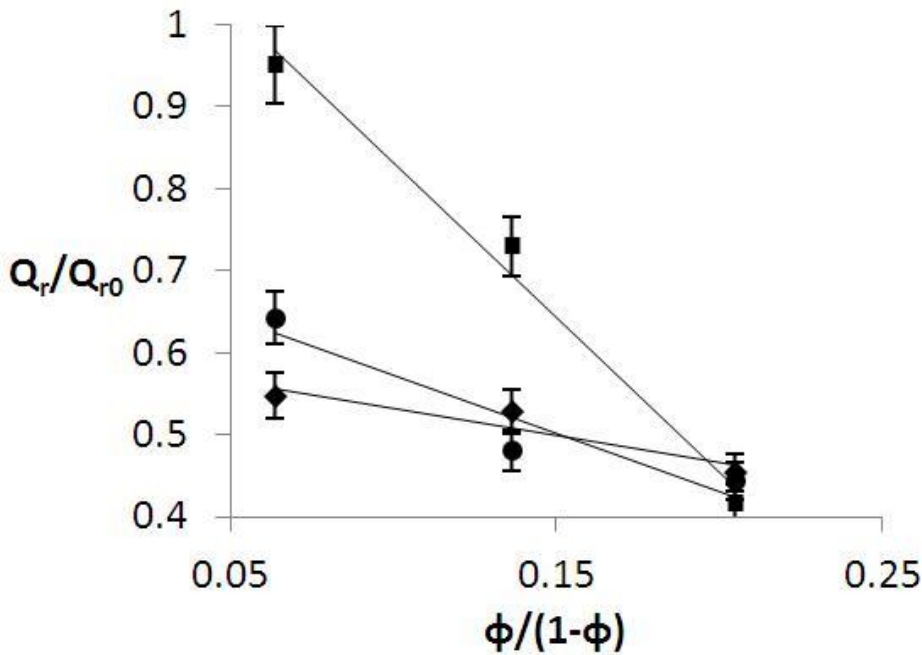


**Figure 4.8:** Reduced values of swelling ratios  $Q_r/Q_{r0}$  plotted against reduced filler volume fraction  $\phi/(1-\phi)$ , for V-SBR-S1-W ( $\diamond$ ), V-SBR-S2-W ( $\bullet$ ) and V-SBR-S5-W ( $\blacksquare$ ) nanocomposites.

The values of  $c$  for V-SBR-SX-W composites calculated by the slopes of the plots reported in Figure are 0,123 for V-SBR-S1-W; 0,176 for V-SBR-S2-W and 0,532 for V-SBR-S5-W. The values of  $c$  increase with the AR of the nanofillers showing that the swelling restriction is more extended in the presence of nanorods in comparison with the spherical particles. This result is consistent with an increasing immobilization capability at the highest ARs.

The high values of  $Q_r/Q_{r0}$  in V-SBR-S5-W at low silica loading compared to V-SBR-S2-W and V-SBR-S1-W, are related to its higher swelling degree due to the easier penetration of the solvent into the crosslinked composites. We suggest that this effect may be due to higher free volume due to a decrease of the packing density of the unbound rubber matrix induced by the formation of domains of aligned particles. This makes the composite more accessible to the solvent and more swellable. At the highest silica loading, the swelling restriction due to immobilized rubber prevails, and  $Q_r/Q_{r0}$  of V-SBR-S5-W strongly decrease.

#### 4.4 Time domain (TD) NMR: mobility regimes of polymer chains

Low field  $^1\text{H}$  NMR measurements were performed using Magic Sandwich Echo (MSE) to investigate the mobility of rubber chains close to the filler particles, distinguishing between the motional regimes of tightly immobilized and more loosely interacting and free rubber. To better characterize these less immobilized fractions of rubber matrix, excluding possible contributions

due to the curing process (e.g different crosslinking degree), Hahn-Echo (HE) and Multiple Quantum (MQ) techniques were also used.

#### 4.4.1 MSE (Magic Sandwich Echo) experiments

Low field TD-NMR of filled V-SBR-SX-W and of the unfilled reference V-SBR-REF-0 were used to investigate the dynamics of the polymer matrix as modified by the presence of the filler particles<sup>7</sup>. <sup>1</sup>H NMR MSE experiments provided information about the fractions of rubber chains having slower dynamics and they allowed correlating the dynamic behavior of the macromolecular chains with the strength of the rubber-silica interaction. The rubber was considered as composed of strongly bound chains with solid-like local mobility and of more mobile rubber phases. The estimation of the more rigid fraction was performed by quantitative detection of the signal obtained by implementing the MSE refocusing block<sup>8</sup>. Direct decomposition of the acquired FID provides the rigid fraction  $f_r$  by using the following equation:

$$(2) \quad \frac{FID(t)}{FID(0)} = f_r \exp\left(-\left(\frac{t}{T_{2r}^*}\right)^2\right) + (1-f_r) \exp\left(-\left(\frac{t}{T_{2m}^*}\right)^v\right)$$

where  $T_{2x}^*$  are the apparent longitudinal relaxation times for the rigid (r) and mobile (m) phases, respectively, and  $v$  parameterizes the deviation of the more slowly relaxing signals from purely exponential shape. Equation (2) provided very good fitting of all MSE refocused FIDs even by fixing the adjustable exponential parameter to 1, thus using a purely exponential form for the effective decay of the mobile part (See example of FID fit in Figure S2 of Supporting Information).  $T_{2r}^*$  values ranged between 22 and 30  $\mu$ s at 310 K while  $T_{2m}^*$  was no less than 0.6 ms and increased with temperature (1.8 ms for V-SBR-S1-35, 1.6 ms for V-SBR-S2-35 and V-SBR-S5-35 and 2.4 ms for the unfilled V-SBR-REF-0 at the highest temperature 393 K). The values indicate the presence of a rigid phase that could be associated either to immobilized rubber or to the proton content of nanoparticles SX (e.g. protons of residual surface hydroxyl groups)<sup>13</sup>. In order to isolate the fraction of rigid protons  $f_r^*$  due only to the immobilized rubber in V-SBR-SX-W, the proton content in SX,  $f_{r(SiO_2)}$ , was measured after removing H<sub>2</sub>O as described in paragraph 2.4 and subtracted from the  $f_r$  values obtained by equation (2). The resulting proton content in SX was: 1.2 % wt/wt in S1, 2.1% in S2 and 2.3% in S5 corresponding to  $f_{r(SiO_2)} = 0,007, 0,014$  and  $0,01$  in the respective V-SBR-SX-35 nanocomposites, where the total fractions of rigid protons are  $f_r = 0.072, 0.095$  and  $0.098$ .

The amount of  $f_r^*$  of V-SBR-SX-35 as a function of temperature is shown in figure 4.9.

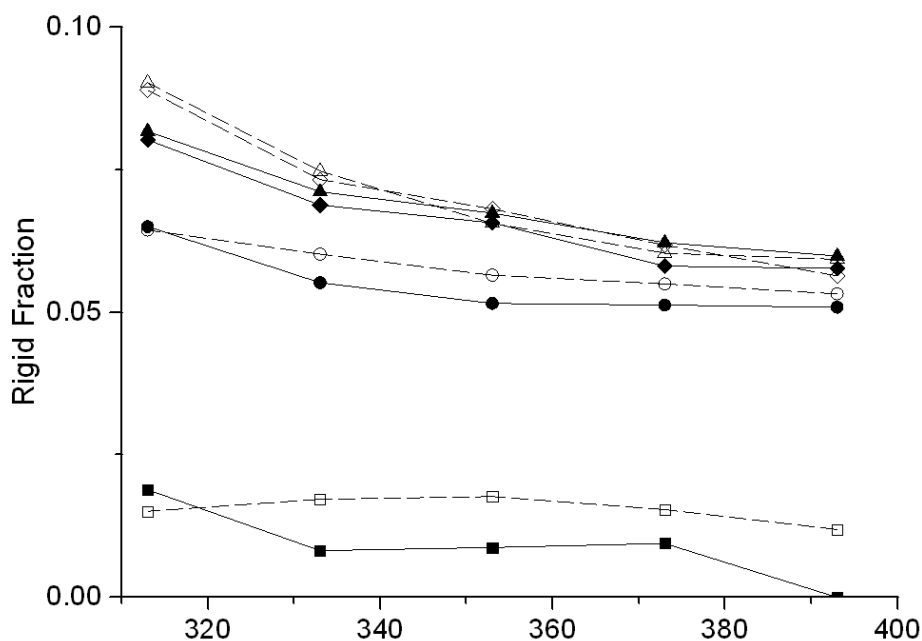


**Figure 4.9:** immobilized polymer fraction  $f_r^*$  as a function of temperature of cured V-SBR-SX-35 (black symbols) and uncured SBR-SX-35 (white symbols) nanocomposites loaded with S1 (●,○), S2 (◆,◇) and S5 (▲, △) silica particles compared to  $f_r$  of unfilled compound V-SBR-REF-0 (■) and SBR-REF-0 (□). Lines are guides for the eye. Error bars of the rigid fraction (omitted) are  $\pm 0.01$ .

The data strongly evidence that the quantity of rigid protons in the rubber surrounding silica NPs varies with the particle AR. The large amount of the rigid fraction even at  $T > T_g + 100$  K, indicates a strong interaction between rubber chains and the fillers.

Considering the error  $\leq 0.01$  for the calculated rigid fraction, there is no significant difference between V-SBR-S2-35 and V-SBR-S5-35 having the highest amounts of rigid proton (respectively 8,1 % and 8.3 % of the total rubber at 313 K), while V-SBR-S1-35 loaded with spherical particles shows a lower amount of it (6,5 %). The rigid component of rubber is substantially absent in unfilled V-SBR-REF-0.

Modeling the shapes of  $\text{SiO}_2\text{-X}$  as perfect spheres or cylinders, the thickness of rubber immobilized as homogeneous layer around isolated silica particles can be roughly estimated. It resulted 3-5.5 nm, in agreement with similar systems reported in the literature<sup>9</sup>. This thickness is associated with a primary layer of tightly bound rubber, strongly interacting with the silica particles through TESPd grafted on the silica surface<sup>10</sup>.

The difference in the rigid fraction between spherical and rod-like particles is in principle attributable to the formation of an interparticle domain which, in the presence of anisotropic particles, immobilizes larger amounts of rubber. This result was supported by the MSE NMR

experiments performed at different silica loading. In figure 4.10, the values of  $f_r^*$  vs the filler loading (expressed as volume fraction of silica in the nanocomposite) of SBR-SX-12, SBR-SX-20, SBR-SX-25 and SBR-SX-35 measured at 313 K are reported. In the composites with the lowest silica content, 12 phr, where filler particles are highly dispersed in the rubber without any alignment<sup>34</sup>,  $f_r^*$  values are similar for both isotropic and anisotropic particles. Instead increasing the amount of filler (20, 25 and 35 phr) the difference in  $f_r^*$  value between spherical and rod-like shape increases.

The non-linearity of the rigid fraction against the silica loading, may possibly be explained by the overlap of the rubber layers of neighboring particles (both spherical and anisotropic), observed also in AFM and TEM images. The larger rubber confinement in the rod domains compared to that in the presence of spherical particles is confirmed by the different slopes of the  $f_r^*$  trends of V-SBR-S1-W, V-SBR-S2-W and V-SBR-S5-W.

The difference between the fraction of the immobilized rubber evaluated by the MSE NMR, compared to that by AFM, suggests that the latter technique, which shows the size and the shape of local heterogeneous rubber zones surrounding the particles, reveals a layer constituted by both tightly immobilized and outermost rubber chains, cross-linked or entangled with the primary layer<sup>17</sup>,

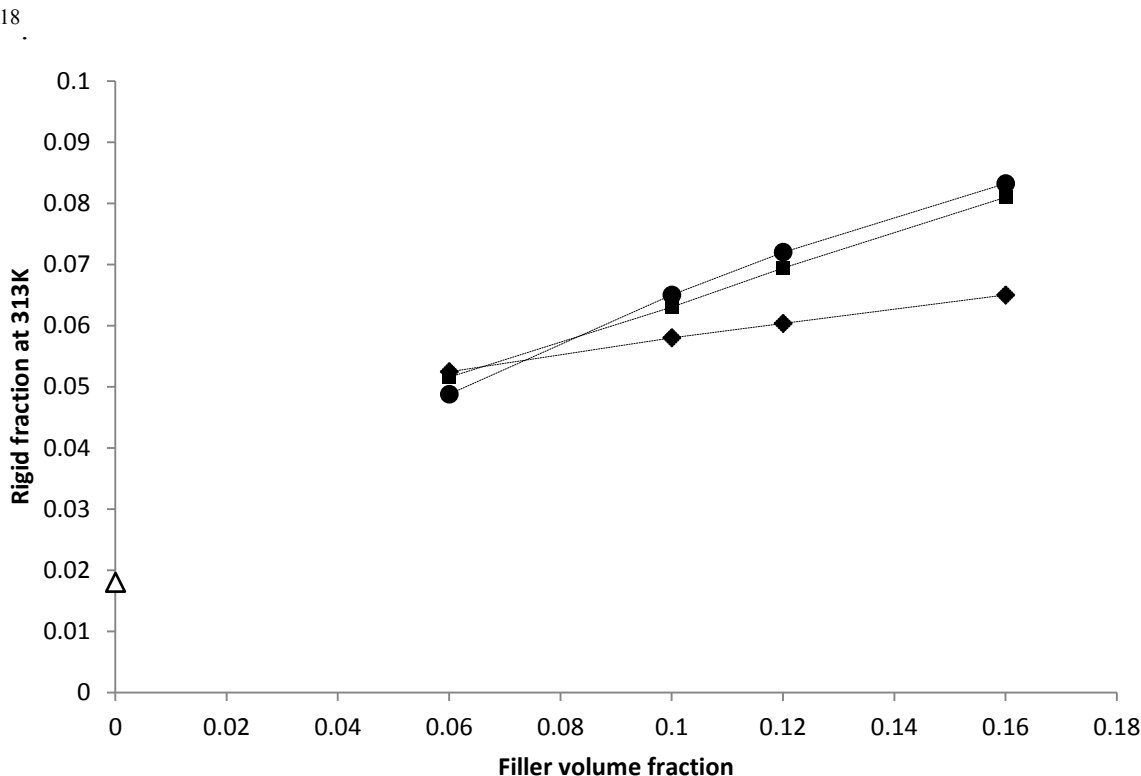


**Figure 4.10.** Immobilized polymer fraction  $f_r^*$  at 313 K as a function of filler volume of V-SBR-S1-W(◆),V-SBR-S2-W (■) and V-SBR-S5-W (●) nanocomposites at different filler loading

(W=12, 20, 25, 35) and of unfilled cured rubber V-SBR-REF-0 ( $\Delta$ ). Error bars of the rigid fraction (omitted) are  $\pm 0.01$ . Dotted lines are guides for the eye.

The absence of significant difference in the rigid rubber fraction between S2 and S5 (Figure 4.10), indicates that the total amount of rigid rubber in the primary layers around these anisotropic fillers is about the same.

MSE experiments were performed also on the compounds SBR-SX-35 and SBR-REF-0 before vulcanization. Interestingly, the amount of rigid rubber is very similar to that calculated for V-SBR-SX-35 (Figure 4.9). This confirms that the effect on the relaxation time is not due to a diffuse hardening of the rubber, but it is a local effect active even before the curing, relatable to the immobilization of the polymer chains interacting with the silica particle.

#### 4.4.2 HE (Hahn echo) experiments

In order to better investigate both the outermost rubber chains more loosely interacting with the primary layer of tightly immobilized rubber and the other less immobilized rubber fractions, the dynamics of the rubber chains were studied by Hahn echo NMR<sup>25</sup> measurements performed on V-SBR-SX-35 and on the uncured compound SBR-SX-35<sup>25, 26</sup>. The fitting of Hahn echo decay allows evidencing the protons with relaxation rates slower than those of the extremely rigid fractions detected by MSE. The decay curves were fitted with a multi parameter function<sup>51</sup> which describes the rubber as composed by three rubber populations A, B and C (expressed as fraction of (A+B+C) rubber) with increasing mobility :

$$(3) \quad \frac{I}{I_0} = A \exp\left\{-\frac{9}{40} D_{res}^2 t^2\right\} + B \exp\left\{-\frac{t}{T_{2B}}\right\} + C \exp\left\{-\frac{t}{T_{2C}}\right\}$$

A is the fraction usually attributed to less mobile chains that are part of a network, whose relaxation is mostly due to residual dipolar interactions  $D_{res}$ ; B is the fraction constituted by chains with a dangling end, with relaxation time  $T_{2B}$ ; C is due to free chains (sol) with high conformational freedom and to extender oil, with relaxation time  $T_{2C}$ <sup>51</sup>.

Detailed analysis of V-SBR-SX-35 was performed at T= 313 K and 393K, far above the  $T_g$ , in order to exclude localized dynamic inhomogeneities that can be present even several tens of degrees above the  $T_g$  itself<sup>52</sup>. Instead, experiments for uncured SBR-SX-35 were performed only at T= 313 K in order to avoid the sample vulcanization at the highest temperatures.

The fitting of the Hahn Echo decay was satisfactory for all samples (an example is given in figure 4.11) and the fitting parameters of all samples are reported in **Errore. L'origine riferimento non è stata trovata**.4.

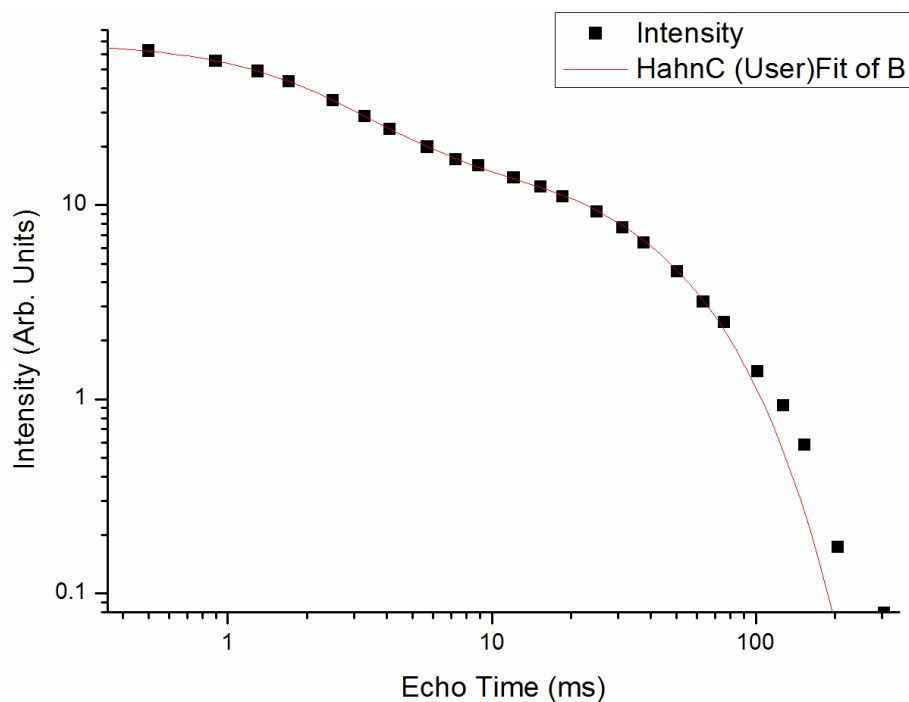


**Figure 4.11:** MSE fitting relative to sample V-SBR-S5-35.

All V-SBR-SX-35 samples present a mainly exponential decay, with a prevalence of the rubber populations B and C, due to a curing degree of V-SBR-SX-35 much lower than highly cured SBR systems reported in the literature<sup>11</sup>. Besides, unfilled V-SBR-REF-0 shows a higher curing degree, possibly due to the adsorption of curing agents on the mesoporous particles in V-SBR-SX-35.

This is confirmed also by the slight increase of A population upon vulcanization compared to uncured SBR-SX-35 in the experiments performed at 313 K. This suggests that the less mobile fraction A, also present in uncured samples, may be constituted not only by the cross-linked chains due to the curing process and by entangled chains of rubber but also by rubber chains interacting with the primary layer of the tightly immobilized polymer detected by MSE. The amount of the different contributions cannot be separated. Moreover the amount of A as fraction of (A+B+C) is underestimated due to the presence of the extender oil in the fraction C.

<i>Sample</i>	<i>Temperature K</i>	<i>A%</i>	<i>B%</i>	<i>C%</i>	<i>D<sub>res</sub> ms</i>	<i>T<sub>2B</sub> ms</i>	<i>T<sub>2C</sub> ms</i>
V-SBR-S1-35	393	13.0	58.4	28.6	1.0	2.5	50.9
V-SBR-S2-35		11.8	60.0	28.2	1.0	2.6	43.4
V-SBR-S5-35		11.8	59.5	28.7	0.9	2.5	40.8
V-SBR-REF-0		19.4	46.4	34.2	1.2	1.8	55.7
V-SBR-S1-35	313	9.6	75.8	14.6	0.7	0.7	9.4
V-SBR-S2-35		9.7	74.0	16.3	0.8	0.7	8.7
V-SBR-S5-35		10.1	74.6	15.3	0.8	0.7	8.9
V-SBR-REF-0		9.6	71.2	19.2	7.1	0.9	8.2
SBR-S1-35	313	7.7	73.4	18.9	6.3	1.0	10.1
SBR-S2-35		7.2	75.4	17.4	7.1	0.9	8.4
SBR-S5-35		8.5	74.8	16.7	5.9	0.9	9.5
SBR-REF-0		6.1	73.5	20.4	5.0	1.0	11.8

**Table 4:** Hanh Echo NMR decay fitting parameters.

In conclusions, HE-NMR analysis evidenced the presence of rubber chains interacting with the primary rubber immobilized at the filler surface but the amount of this fraction cannot be evaluated. Thus it is not possible to trace a direct relationship between the A population and the layers detected by AFM. The rubber chains in the outermost rubber zone observed by AFM around the filler particle may include chains with relaxation times higher than those of the less mobile fraction A and probably part of B population, thus explaining the larger layer detected by AFM.

#### 4.4.3 MQ (Multiple Quantum) experiments

Further analysis of the polymer network was performed by MQ-NMR<sup>41</sup> on V-SBR-SX-35 in comparison with the unfilled V-SBR-REF. MQ-NMR is a recent method for studying networks in polymeric materials, more reliable than Hahn Echo, since it avoids fitting artifacts associated to transverse relaxometry experiments.

The experimental raw Double Quantum (DQ) function  $I_{DQ}$  and the sum MQ decay  $I_{\Sigma MQ} = (I_{DQ} + I_{ref})$ , where  $I_{ref}$  is the raw experimental reference decay function, are reported as a function of the pulse sequence duration  $\tau_{DQ}$  in Figure 4.12 a. The build-up normalized DQ function  $I_{nDQ} = (I_{DQ} / I_{\Sigma MQ})$  for the same samples V-SBR-SX-35 and V-SBR-SX-REF are reported in Figure 4.12 b.



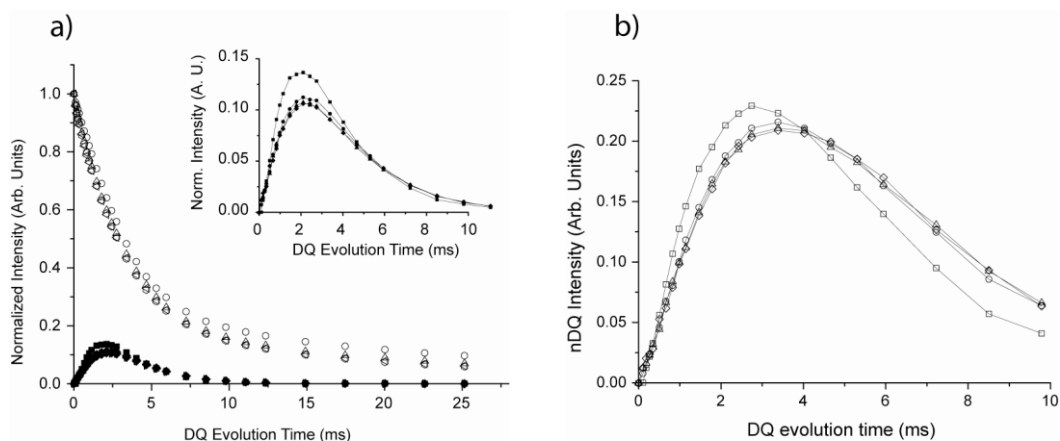


**Figure 4.12:** (a) MQ functions vs. DQ evolution time of (●,○) V-SBR-S1-35; (◆,◇) V-SBR-S2-35 and (▲, △) V-SBR-S5-35 nanocomposites compared to unfilled V-SBR-REF-0 (■, □). Black symbols indicate  $I_{DQ}$ , white symbols  $I_{\Sigma MQ}$ . The inset magnifies  $I_{DQ}$  plots. (b) Normalized MQ functions  $I_{nDQ}$  of (○)V-SBR-S1-35; (◇)V-SBR-S2-35 and (△) V-SBR-S5-35 compared to V-SBR-REF-0 (□). Lines are guides for the eye.

It was demonstrated that  $I_{nDQ}$  intensity increases up to 0.5 in fully crosslinked rubber. The  $I_{nDQ}$  intensity of all V-SBR-S5-35 samples increase up to value of about 0.2 (Figure 4.12), indicating a low cross-linking degree. This hinders the possibility of properly fitting the curve using Tichonov regularization<sup>12</sup> or other simplified models in order to differentiate between the less immobilized rubber population of the system.

$I_{nDQ}$  values of V-SBR-SX-35 presents a slightly lower maximum than unfilled V-SBR-REF-0 indicating a lower crosslinking degree, possibly due to the adsorption of curing agents on the mesoporous particles. On the other side, the curves of V-SBR-SX-35 samples display negligible differences, thus indicating a very similar efficiency of vulcanization in the presence of fillers with different shapes. This results are in agreement with the conclusions of Hahn Echo investigation and point out that the differences in the mechanical reinforcement of V-SBR-SX-35 samples (see chapter 5, Dynamic Mechanical Analysis) are not significantly related to the modifications of the rubber matrix induced by curing.

## References

- [1] R. A. Vaia and J. F. Maguire *Chem. Mater.* 2007, 19, 2736-2751
- [2] Brewer A. K., Striegel A. M. *Analytical chemistry* **2011**, 83, 3068–3075
- [3] Di Nardo N. J., *Nanoscale Characterization of Surfaces and Interfaces*, VCH, **1994**
- [4] Qu M., Deng F., Kalkhoran S. M., Gouldstone A., Robisson A., Van Vliet K. J. *Soft Matter* **2011**, 7, 1066–1077
- [5] B. Meissner, *Rubber Chem Technol*, **1995**, 68, 297-310
- [6] L. Bokobza, A.L. Diop, *eXPRESS Polymer Letters* **2010**, 4, 355–363
- [7] Papon A., Saalwachter K., Schaler K., Guy L., Lequeux F., Montes H. *Macromolecules* **2011**, 44(4), 913-922
- [8] Mauri M., Thomann Y., Schneider H., Saalwächter K. *Solid State Nuclear Magnetic Resonance* **2008**, 34, 125-141
- [9] Mujtaba A., Keller M., Ilisch S., Radusch H. J., Beiner M., Thurn-Albrecht T., Saalwachter K., *ACS Macro Lett.* **2014**, 3, 481
- [10] Valentín J. L., Mora-Barrantes I., Carretero-González J., López-Manchado M. A., Sotta P., Long D. R., Saalwächter K., *Macromolecules* **2010**, 43, 334
- [11] Saalwachter K., *Progress in Nuclear Magnetic Resonance Spectroscopy* **2007**, 51, 1-35
- [12] Chassé W, Valentín JL, Genesky GD, Cohen C, Saalwächter K, *The Journal of Chemical Physics* **2011**;134



## **Chapter 5**

# **DYNAMO-MECHANICAL PROPERTIES OF SCS/SBR NANOCOMPOSITES**

The chapter is dedicated to the discussion of dynamo-mechanical properties of nanocomposites whose preparation, morphology and chemical properties were described in the previous chapters. Here, both uncured and cured nanocomposites were characterized first with an Oscillating Disk Rheometer (ODR) operating in shear mode. Dynamo-mechanical thermal analysis (DMTA) gave quantitative information about the rubber immobilization operated by differently shaped nanoparticles and mixed-filler systems. Selected cured samples were more deeply investigated, in particular through tensile analysis, Mullins effect and compression dynamics, in order to describe the implications on rubber reinforcement given by anisotropic rather than spherical silica nanoparticles.

### 5.1 Rheological properties by ODR (Oscillating Disk Rheometry)

Rheological measurement were first conducted on uncured SBR-SX-35 nanocomposites (figure 5.1) in order to assess the reinforcement effect provided by the differently shaped nanofillers SiO<sub>2</sub>-SX on uncured nanocomposites without considering the vulcanization reaction. The addition of silica NPs to the SBR matrix provide composites with viscoelastic behavior, characterized by a non linear dependence of the storage modulus  $G'$  on the applied strain (Payne effect, see chapter 2). In fact, the storage modulus  $G'$  at low strain ( $G'_0$  at 2%) decreases rapidly by increasing the strain amplitude, and at large strain amplitude ( $G'_\infty$  at 100%) approaches the lowest value. The breakdown of the filler inter-aggregate network is responsible to this stress softening.

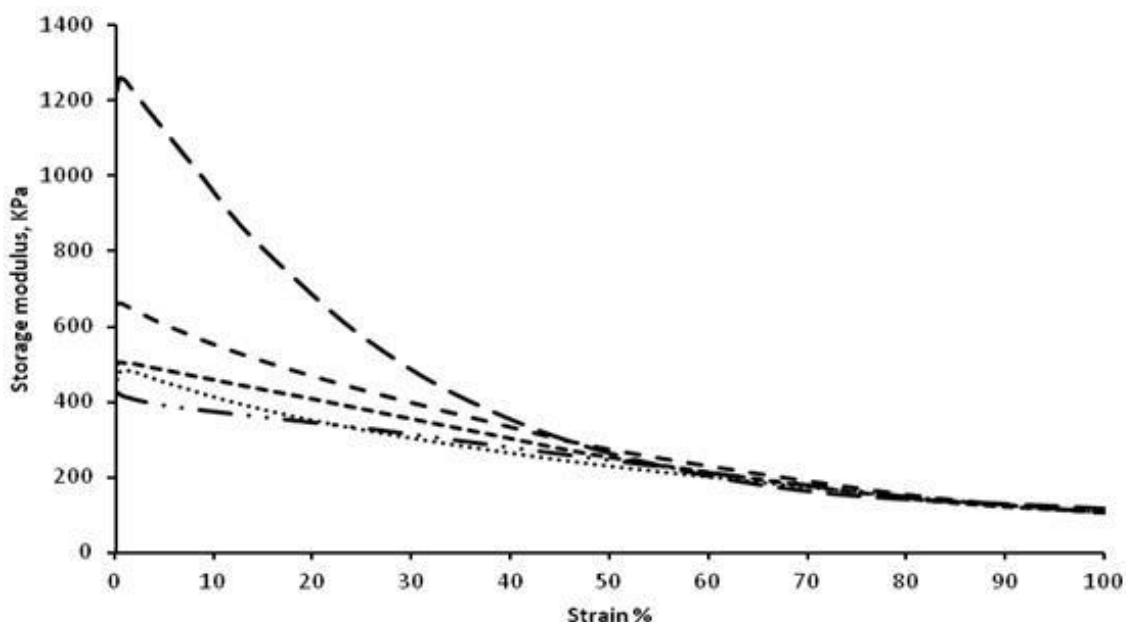


**Figure 5.1:** Storage modulus  $G'$  vs strain of uncured SBR-SX-35 composites: a) SBR-S1-35(•••); b) SBR-35-S2(---); c) SBR-35-S5(- - -); d) SBR-35-S7(— — —); e) SBR-35-S10(— ••).

According to the widely accepted mechanistic interpretation that the Payne effect is related to the

destruction of filler network upon oscillatory shear, the higher  $G'_0$  values obtained in the presence of anisotropic particles point out a stronger reinforcing effect. In fact, SBR-S2-35, SBR-S5-35 and SBR-S7-35 show  $G'_0$  values higher than those of SBR-S1-35 and SBR-S10-35 whose fillers are totally or mostly spherical. The modulus values at the highest deformation ( $G'_{\infty}$ ) are very similar for all SBR-SX-35 composites. This means that differences in reinforcement are less effective once the network is broken down. In fact, the filler synthesis has been targeted to obtain NPs homogeneous in surface chemistry and only different in their shapes.

The trend of the elastic modulus  $G'_0$  of the composites can be correlated to the shape of silica particles.

The reinforcing effect of SBR-SX-W increases with the AR of the rod-like particles. This behavior can be associated both to the self assembling properties of the particles, which are aligned along the major axis and to the very large contact area between anisotropic filler and polymer. As regards the alignment, this effect becomes more evident for the longest rods in SBR-S5-35 and SBR-S7-35 than for the slightly anisotropic SBR-S2-35.

It is well known that the oriented arrangements of particles in a polymer matrix enhance the composite modulus compared to a random distribution, hence in the case of 1D rods the reinforcement is more effective along their main dimension<sup>1</sup>.

This effect can be evaluated by simple geometrical observation, comparing the effective surface area  $Y=A/V$  of the spherical particles with that of the cylindrical rods with high AR<sup>2</sup>.  $V$  is the volume of the filler and  $A$  is the surface area normal to the direction of the major axis, which is the portion of the total particle surface interacting with the other aligned particles. The values of  $Y$  are  $3/2d$  and  $4/d$ , respectively<sup>2</sup>, where  $d$  is the diameter of the sphere or the cross section of the rods. As  $d$  is quite the same for spheres and rods in all SBR-SX-W nanocomposites (70-80 nm), the reinforcement efficiency due to orientation is higher for the rods.

The modulus improvement in SBR-SX-W can also be associated to the polymer layer arrangement around particles. In all samples the thin layers surrounding the filler particles, evidenced by TEM images and provided by the bifunctional coupling agent TESPT, cause immobilization of the polymer chains near the particle surface in comparison with those in the rubber matrix. When the rubber layers of different particles overlap, the reinforcement effect increases with the extent of rubber overlapping area. In SBR-SX-35 the distances between particles are small for both spherical and rod-like fillers. Thus, the thin layers around filler particles overlap and build bridges between the fillers, enhancing the reinforcement of rubber<sup>3</sup>. In addition, the anisotropic shape and the alignment of the rod-like particles provide a larger interface between the silica and the rubber, further enhancing the amount of overlapping rubber layers and thus improving the mechanical

properties.

Results of dynamic-mechanical analysis performed after thermal treatment of SBR-SX-35 (150°C, 10 min) are reported in Figure 5.2.

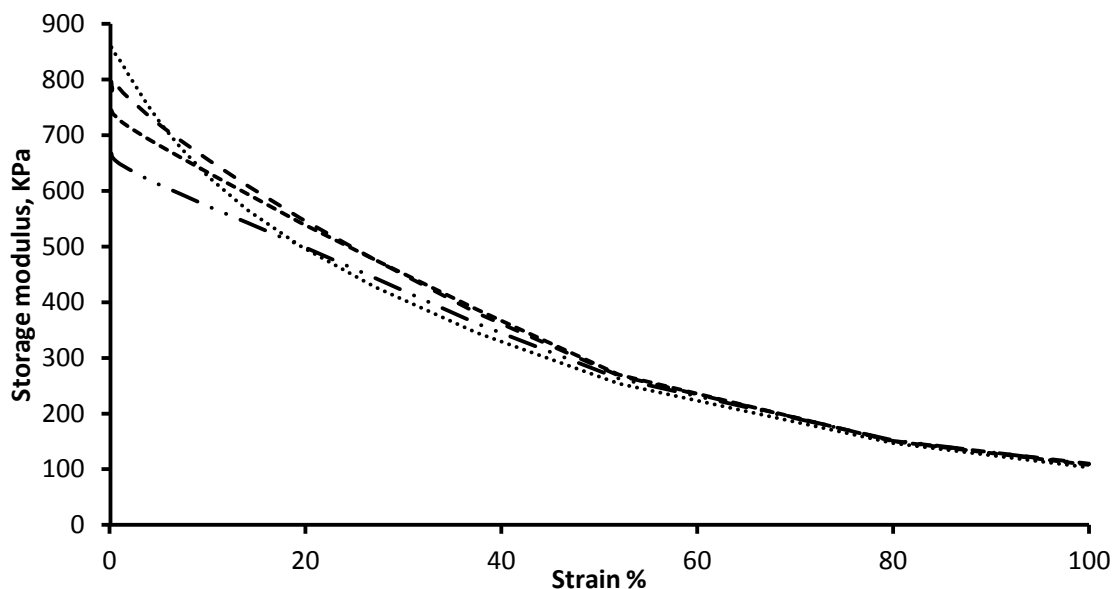


**Figure 5.2:** Storage modulus  $G'$  vs strain of the uncured SBR-SiO<sub>2</sub>-X composites after thermal treatment at 150°C for 10'. a) SBR-S1-35(•••); b) SBR-S2-35(---); c) SBR-S5-35 (- - -); d) SBR-S10-35(—••).

These experiments were aimed to assess the thermal stability of the uncured compounds. Upon heating in absence of curatives, filler agglomeration occurs as demonstrated by the increase of modulus in all samples. It is interesting to note that the spherical NPs of SBR-S1-35 show the highest modulus increase at low strain. This may be ascribed to less immobilized rubber in the as prepared uncured SBR-S1-35 sample, compared to the other SBR-SX-35 composites, producing higher filler mobility and easier flocculation.

Stress-strain measurement on uncured nanocomposites containing 35 phr of a mixture of spherical SiO<sub>2</sub>-S1 and anisotropic SiO<sub>2</sub>-S5 NPs are reported in figure 5.3 and compared with pure-shape SBR-S1-35 and SBR-S5-35. The reinforcement effect linearly increase from pure-shape SBR-S1-35 to SBR-S5-35 going through SBR-MX-35 at increasing relative amount of SiO<sub>2</sub>-S5 nanoparticles content, confirming that low-strain modulus takes advantage of the presence of anisotropic nanoparticles.

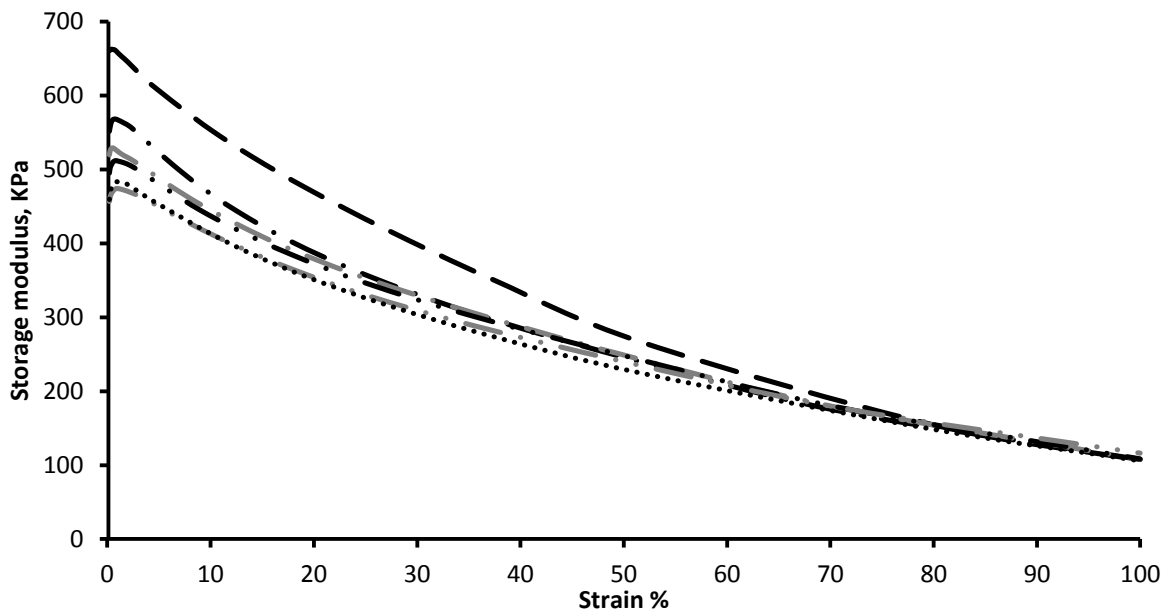


**Figure 5.3:** Storage modulus  $G'$  vs strain of the uncured mixed-shape SBR-MZ-35 composites compared with pure-shape SBR-S1-35 ( $\bullet\bullet\bullet$ ) and SBR-S5-35 ( $- - -$ ). a) SBR-MA-35( $- \cdot \cdot \cdot$ ); b) SBR-MB-35( $- \cdot \cdot \bullet$ ); c) SBR-MC-35 ( $- - \cdot$ ); d) SBR-MD-35( $- - \bullet$ ).

The strain dependence of the loss modulus  $G''$  obtained for of SBR-SX-35 is reported in Figure 5.4. The trend of  $G''$  indicates a strong impact of the particle shape on  $G''$  maximum. In fact, SBR-S2-35, SBR-S5-35 and SBR-S7-35 show a broad maximum at strain between 50 - 60% , while the maximum for SBR-S1-35 is at strain  $<10\%$ . SBR-S10-35, containing both elongated and spherical particles, has an intermediate behaviour with a maximum at high strain but with a value lower than SBR-SiO<sub>2</sub>-2, SBR-SiO<sub>2</sub>-5 and SBR-SiO<sub>2</sub>-7 where all NPs are anisotropic. The result can be rationalized as follows.

The loss modulus  $G''$  depends on the rates of network breakdown and reformation, due to the strain amplitudes. Loss modulus curves identify the maximum strain at which the composite is able to withstand to the dynamic-mechanical solicitation without breakage of the filler network. At lower strain the network is still able to reform after each deformation, thus showing an elastic behaviour<sup>4</sup>. At higher strain, the strain amplitude is high enough to destroy the filler network, which cannot reforms in the time scale of the dynamic strain, and the effect of filler network on  $G''$  disappears<sup>4</sup>. In the investigated silica-rubber composites, the higher the  $G''$  values and the strain at which  $G''$  is maximum, the stronger the network. The highest  $G''$  values of SBR-S7-35, SBR-S5-35 and SBR-S2-35 confirm that the anisotropic particles form a strong network entrapping a large amount of rubber which enhances the reinforcing effect.



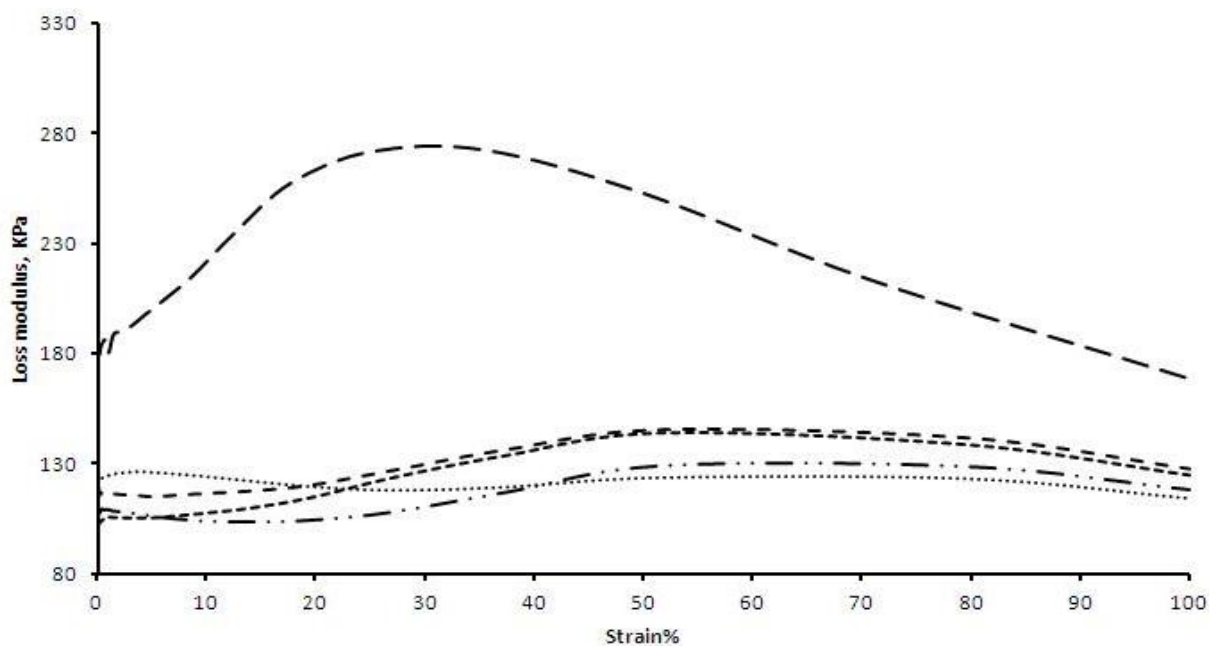


**Figure 5.4:** Loss modulus  $G''$  vs strain of the uncured SBR-SX-35 composites: a) SBR-S1-35( $\bullet\bullet$ ); b) SBR-S2-35 (---); c) SBR-S5-35 (- - -); d) SBR-S7-35 (— — —); e) SBR-S10-35 (— $\bullet\bullet$ ).

After checking optimal curing conditions by MDR analysis (see Appendix A), uncured SBR-SiO<sub>2</sub>-X samples were vulcanized according to the procedure reported in the experimental section. The  $G'$  vs strain plots of V-SBR-SX-35 are reported in figure 5.5.

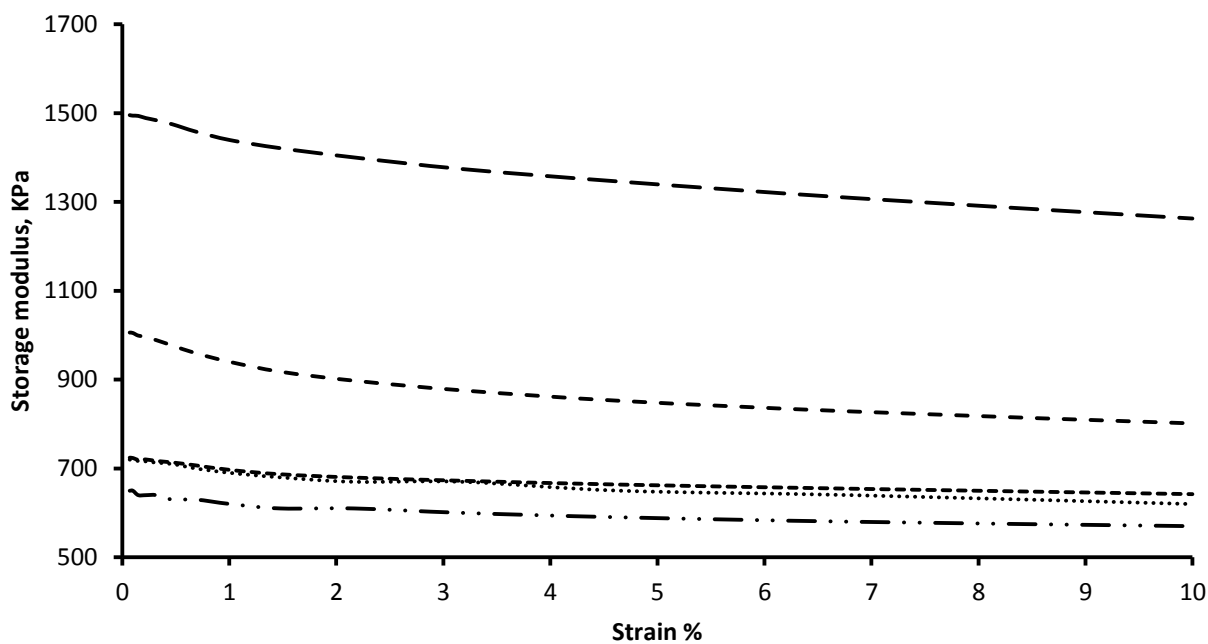


**Figure 5.5:** Storage modulus  $G'$  vs strain of the cured V-SBR-SX-35 composites. a) V-SBR-S1-35 ( $\bullet\bullet\bullet$ ); b) V-SBR-S2-35(---); c) V-SBR-S5-35(- - -); d) V-SBR-S7-35 (— — —); e) V-SBR-S10-35 (— $\bullet\bullet$ ).

$G'$  values have similar trends with respect to SBR-SX-35 as demonstrated by the  $G'_0$  at low strain reported in Figure. This demonstrates that after vulcanization, which strongly improves the mechanical properties of the rubber, the effect of the filler anisotropy remains significant.

### 5.2 Rheological behaviour rationalization by the Einstein-Guth-Smallwood equation

The reinforcement effect can be rationalized by considering the reinforcing particulate as a modifier of the regular flow properties of a viscoelastic material such as rubber. This is the concept of the rheological equations employed for the prediction of final material properties, which consider different filler properties as a contributors to reinforcement. The effect of the shape factor can be predicted by the Einstein equation modified by Guth-Smallwood

$$(1) \quad G'_0(\varphi) = G'_0(0) \times (1 + \varphi \times AR + \varphi^2 \times AR^2)$$

where  $\varphi$  is the filler volume fraction,  $G'_0(\varphi)$  the modulus of the composite and  $G'_0(0)$  the modulus of the rubber. The filler volume fraction ( $\varphi$ ) is kept constant to study the low strain dependence of  $G'_0$  on the AR.

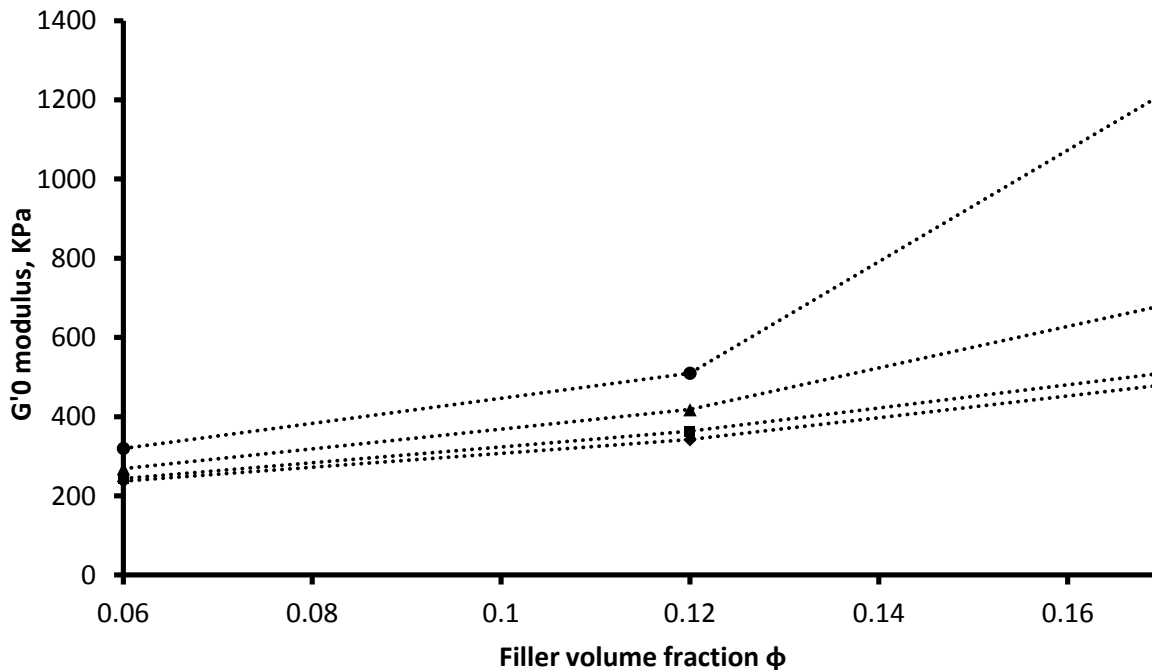


**Figure 5.6** Plot of  $G'_0$  values vs filler volume fraction ( $\varphi$ ) of composites SBR-S1-W ( $\blacklozenge$ ), SBR-S2-W ( $\blacksquare$ ), SBR-S5-W ( $\blacktriangle$ ), SBR-S7-W ( $\bullet$ ). Dashed lines helps the reader.

The plot of measured  $G'_0$  vs filler volume fraction ( $\varphi$ ) of silica particles is reported in figure 6 for SBR-SX-W nanocomposites.

This graph highlights the modulus improvement that occurs at the filler volume fraction. The effect is particularly marked in the case of nanocomposites of highest aspect ratios nanofiller, confirming their high capability of forming a strong network and suggesting a lowered percolation threshold with respect to spherical nanoparticles as reported in literature for similar systems.

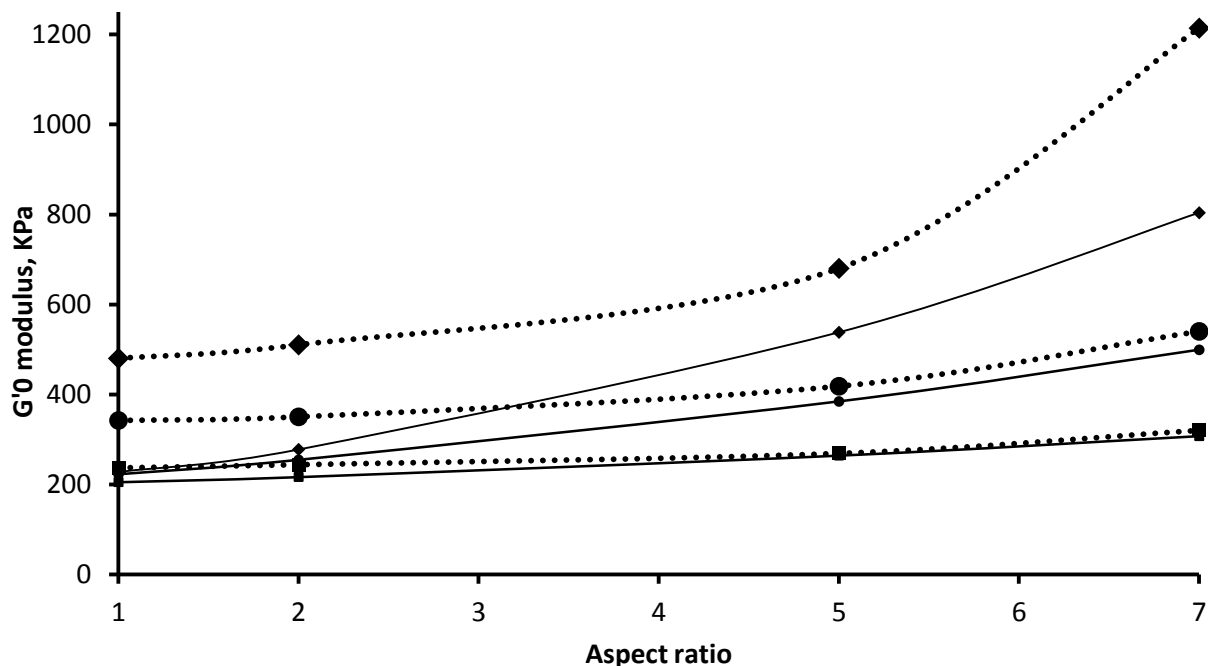


**Figure 5.7** Plot of  $G'_0$  values vs particle aspect ratio for SBR-SX-35 (◆), SBR-SX-25 (●), SBR-SX-12 (■) of silica NPs (dashed lines), compared with the trend of the Einstein-Guth-Smallwood equation calculated for 35, 25 and 12 phr (straight lines).

The plot of measured  $G'_0$  vs AR of silica particles is reported for SBR-SX-35 ( $\phi = 0.20$ ) in figure 5.7, in comparison with the curve derived from equation (eq.1). The experimental values result always higher than the theoretical ones, although  $G'_0$  values increase by increasing the AR value. Since the Einstein-Guth-Smallwood equation for filled systems considers only the hydrodynamic effects, and not aggregative or networking phenomena, the results confirm the formation of a percolative filler network in SBR-SX-35.

In Figure 7 experimental and theoretical trends of  $G'_0$  vs AR for SBR-SX-12 ( $\phi = 0.067$ ) are also reported.  $G'_0$  values are much lower and vary slightly with AR. In agreement with the lower reinforcing effect, the values correspond to those calculated from the model equation, indicating that at this loading, the particles are isolated and do not interact significantly within SBR matrix.

SBR-S10-35 as well as SBR-MX-35 samples were excluded from the comparison with the Einstein-Guth-Smallwood model, since the filler shape is not uniform.

### 5.3 Compression dynamics experiments

Compression dynamic experiments were also performed at 70°C and 10 Hz on a selected number of cured samples in order to verify the performances of the composite materials in conditions that mimic the compressive forces sustained during usage. In Table 1 the storage and loss modulus  $E'$  and  $E''$  and the values of  $\tan\delta$  measured in the strain range 3.5 - 25% are reported for all V-SBR-SX-35 samples. In Figure 5.8,  $E'$  values obtained at the lowest strain ( $E'_0$ ) are reported for V-SBR-SX-35 composites and compared with  $G'_0$  values obtained in shear mode.

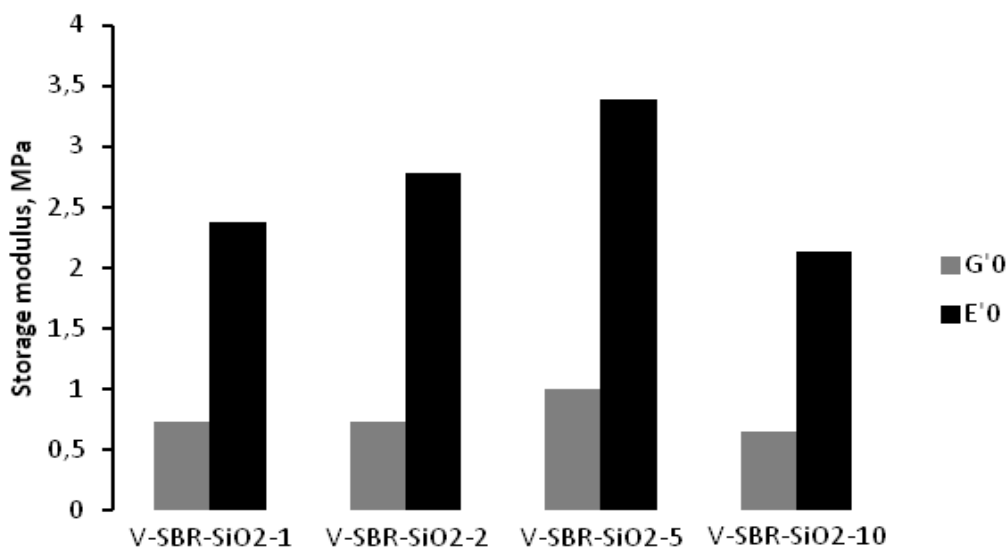


**Figure 5.8:** Storage modulus at low strain of cured compounds V-SBR-SX-35 measured in dynamic compressive ( $E'_0$ ) and static shear ( $G'_0$ ) mode.

The trend is similar in dynamic compression and static shear mode for all the investigated materials, confirming that the effect of the anisotropic shapes on the mechanical properties is also relevant for the final rubber material. A direct comparison of these results is given by the equation

$$(2) \quad E = 2G \times (1 + \nu)$$

Where  $\nu$  is the materials' Poisson ratio, which is about 0.35 for both rubber and rubber nanocomposites (rif. Ferry). The equation is well-matching the results, because compressive moduli are approximatively three times higher than corresponding shear moduli.

It must be noted that samples for compression dynamics experiments undergo applied strain in the normal direction of the strain applied in shearing mode on the same samples. Since the compressive moduli are consistent with the moduli in shearing mode, we have an indication the material is mechanically isotropic. In other words, the same sample gives the same mechanical response if strained at different orientations. This is consistent with TEM observation, in which anisotropic

nanoparticle alignment was localized in the self-assembled nanoparticle domains and not extended throughout the whole matrix.

**Table 5.1** Storage modulus  $E'$ , loss modulus  $E''$  and  $\text{Tan}\delta$  by compression dynamic experiments

	V-SBR-SiO <sub>2</sub> -1	V-SBR-SiO <sub>2</sub> -2	V-SBR-SiO <sub>2</sub> -5	V-SBR-SiO <sub>2</sub> -10
$E'$ (MPa)	2.376	2.779	3.385	2.124
$E''$ (MPa)	0.232	0.281	0.380	0.224
$\text{Tan}\delta$	0.098	0.101	0.112	0.105

#### 5.4 Temperature dependent dynamo-mechanical studies (DMTA)

DMTA analyses of cured V-SBR-SX-W composites were performed in order to correlate the filler morphology to storage ( $G'$ ) and loss ( $G''$ ) modulus and to  $\text{tan}\delta$ , in the temperature range from -80 to +120 °C. The measurements showed the effect of rubber immobilization on the mechanical properties of the nanocomposites.

The trends of the storage modulus  $G'$  and  $\text{tan}\delta$  vs temperature are plotted in Figure 5.9 for V-SBR-SX-35 compared with the unfilled V-SBR-REF-0. The storage modulus in the rubbery region (Figure 5.9 a) increases with increasing the particle AR at the same filler content in agreement with ODR measurements. The trend of  $\text{tan}\delta$  with the temperature separates the energy dissipative events occurring in a range of temperature between -80 and 120°C. Plots (Figure 5.9 b) show a main maximum corresponding to the rubber glass transition temperature (peak 1) and a secondary relaxation peak at higher temperature (peak 2), in accordance to similar systems<sup>5</sup>.

This secondary peak is generally attributed to the rubber fraction interacting with the filler that

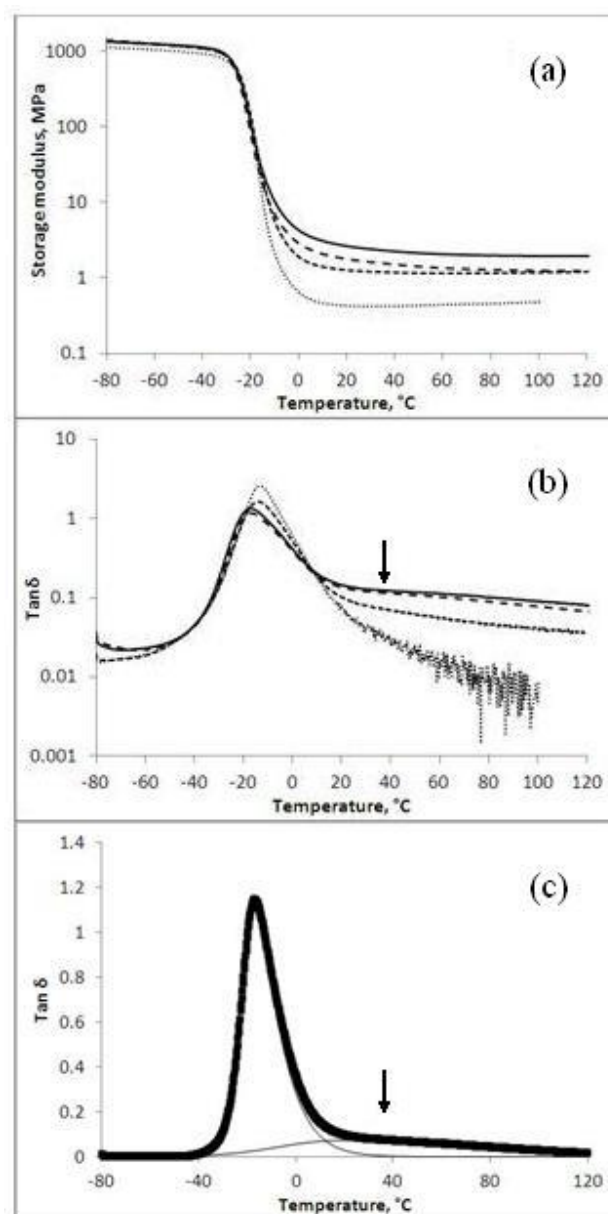


**Figure 5.9.** Plots of a) storage modulus  $G'$  and b)  $\text{tan}\delta$  vs. temperature for V-SBR-S5-35 (full line), V-SBR-S2-35 (—) and V-SBR-S1-35 (-) nanocomposites, and V-SBR-REF-0 (•).

causes a greater slowdown of polymer dynamics at the filler/rubber interface, compared to the rubber chains far from the particle interface. Increasing the nanoparticle AR, the intensity of the secondary relaxation peak in the region above the main glass transition increases. The trend is confirmed also for the less loaded nanocomposites V-SBR-SX-25 and V-SBR-SX-12 (plots not reported in the figure). The values of  $\tan\delta$  are generally influenced by the values of the elastic modulus  $G'$ . However, as the two relaxation peaks belong to the same system, their relative area can be considered independent of  $G'$  and approximately corresponding to the relative fraction of the free and immobilized rubber components.

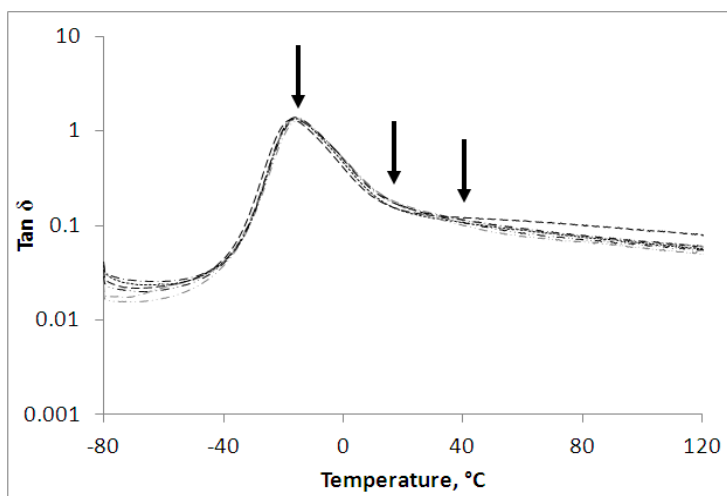


**Figure 5.10.** Plots of  $\tan\delta$  vs. temperature for V-SBR-MX-35 composites compared with pure-shape V-SBR-S1-35 ( $\bullet\bullet\bullet$ ) and V-SBR-S5-35 (- - -). a) V-SBR-MA-35(- -  $\bullet\bullet$ ); b) V-SBR-MB-35(- -  $\bullet\bullet$ ); c) V-SBR-MC-35 (- -  $\bullet$ ); d) V-SBR-MD-35(- -  $\bullet$ ).

The trends of  $\tan\delta$  vs temperature are plotted in Figure 5.10 for V-SBR-MX-35 compared with the pure-shape V-SBR-S1-35 and V-SBR-S5-35. While the first and third arrow from the left indicate relaxation events already discussed for pure-shape nanocomposites, the second arrow from the left indicate a shoulder of the secondary relaxation peak that is present just for V-SBR-MX-35 nanocomposites. Even if the position of the maximum is different from pure-shape V-SBR-SX-35 nanocomposites, it contributes to the dissipation event not related to the main glass transition; furthermore, rubber immobilized in V-SBR-MX-35 has lower relaxation temperature, indicating an higher mobility. It can be considered as a first evidence of the formation of a dual-filler network, different from the pure-shape materials.

In order to evaluate the amount of the immobilized rubber,  $\tan\delta$  curves were deconvoluted into two asymmetric double sigmoid curves according to the approach of Arrighi *et al.*<sup>6</sup>. The immobilized

rubber content ( $R_i\%$ ) was calculated as a ratio of the area of the peak 2 with respect to the sum (peak1 + peak 2) for V-SBR-SX-W with different silica loading and different particle AR.

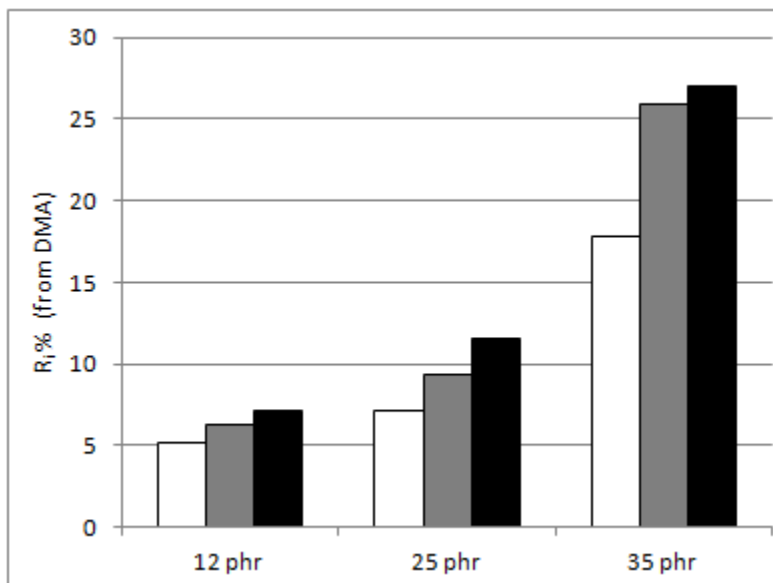


**Figure 5.11.** Percent of immobilized rubber ( $R_i\%$ ) calculated by DMA curves integration for V-SBR-SX-W with a different silica loading and particle aspect ratio: (grey) V-SBR-S1-W; (dark grey) V-SBR-S2-W; (black) V-SBR-S5-W.

The results clearly show that the amount of immobilized rubber increases both with the filler content and the particle AR (Figure 5.11), the highest values resulting for V-SBR-SX-35 in the loading range 18-27 %. It is noteworthy that in V-SBR-SX-12, where silica particles are isolated and no aggregations form, the amount of immobilized rubber only slightly increases with the AR, unlike V-SBR-SX-25 and mainly V-SBR-SX-35. Even if a contribution due to a lower percolation threshold for the anisotropic particles at the highest silica loading cannot be excluded, this confirms that the self assembled long particles in the V-SBR-S2-35 and V-SBR-S5-35 composites are able to immobilize a large amount of rubber if compared to V-SBR-S1-35 containing spherical particles. As regards mixed-shape filled nanocomposites V-SBR-MX-35, the calculated  $R_i\%$  values are centered around the value of  $23\pm 0.5$ . The distinctly high immobilized rubber amount for all the mixed-shape nanocomposites can be thus associated with the formation of a dual filler network, capable of entrapping efficiently macromolecular chains. In fact, Bokobza reported a similar effect in case of a dual-filler system containing spherical silica with anisotropic Sepiolite nanoparticles. In this systems, the bound rubber amount measured with a classical solvent extraction method improved from the single-filler system. In addition, in our series of mixed-shape silica nanocomposites, the  $R_i\%$  amount depend little from the relative quantities of  $\text{SiO}_2\text{-S1}$  and  $\text{SiO}_2\text{-S5}$ ,

since the curves are almost super imposable (figure 5.10); this again confirm that the result of combining SiO<sub>2</sub>-S1 and SiO<sub>2</sub>-S5 nanoparticles is cooperative and non-additive.

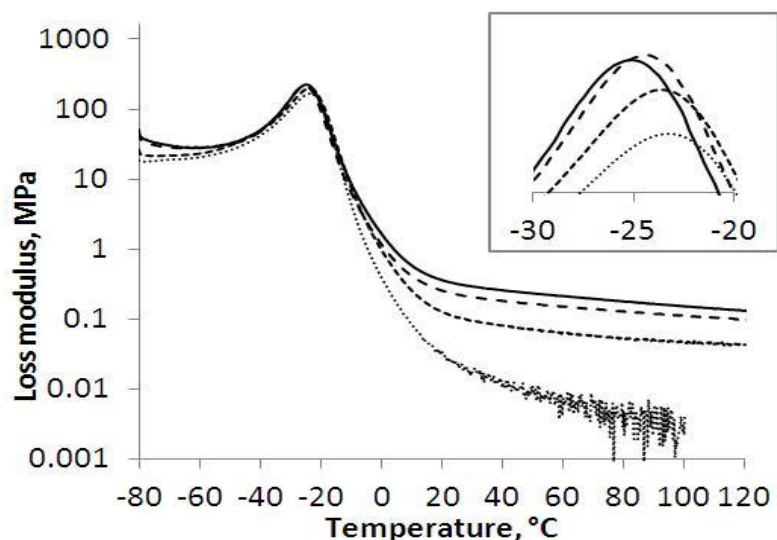


**Figure 5.12.** Plot of loss modulus against temperature for V-SBR-S5-35 (full line), V-SBR-S2-35 (—) and V-SBR-S1-35 (-) nanocomposites, and V-SBR-REF-0 (•); in the inset, a zoom on the main glass transition peak to highlight the curves maxima.

The temperature dependence of the loss modulus  $G''$  is reported in Figure for V-SBR-SX-35 nanocomposites.  $G''$  plots allow to compare the glass transition of rubber in the composites more reliably than the  $\tan\delta$  plot does, since in this case the maximum of the curve is not influenced by the value of  $G'$ . The main glass transition gradually shifts to a lower temperature by increasing AR (inset in Figure 12). SBR-S1-35 has a  $T_g = -23.3$  °C, quite similar to that of unfilled reference V-SBR-REF-0 ( $T_g = -23.0$  °C) while V-SBR-S2-35 and V-SBR-S5-35 have  $T_g$  of  $-24,3$  and  $-25,3$  °C, respectively. These results are consistent with the so called “plasticization” effect of the bulky rubber already proposed by the literature<sup>7</sup> to explain the different dynamics of the rubber layers remote from those close to the constrain. According to this effect, increasing the amount of immobilized rubber at the polymer filler interface, a decrease of the packing density of the unbound bulk polymer is observed. The increase of the free volume within the rubber matrix improves the chain freedom degree and, consequently, reduces the glass transition temperature. In our case, the presence of an increased fraction of low molecular weight products has been excluded in nanocomposites with high ARs NPs. Therefore, the extent of these effects in V-SBR-S5-35 may be related to the formation of domains of aligned anisotropic NPs which immobilize higher rubber amount by increasing their ARs.



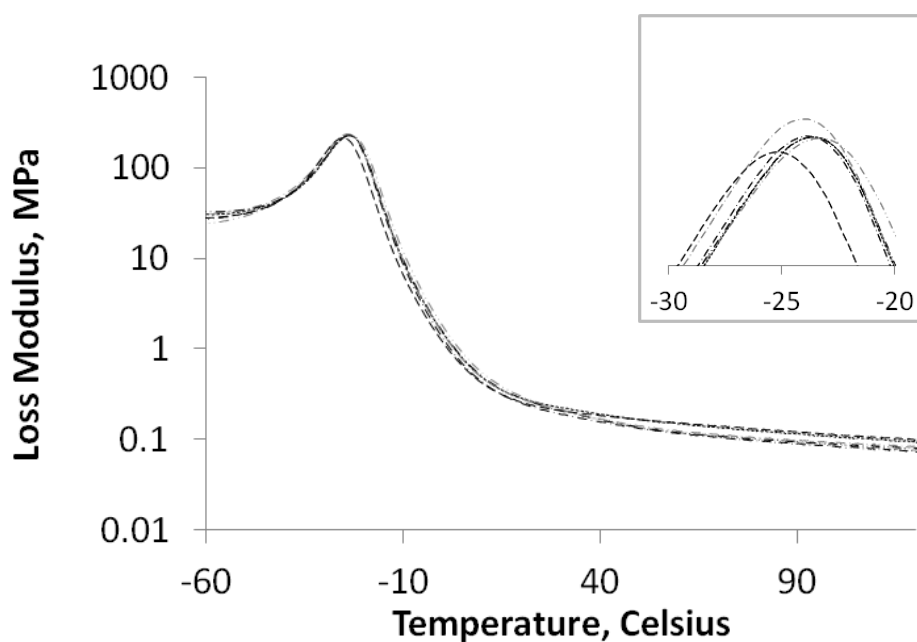


**Figure 5.13:** Loss modulus  $G''$  vs Temperature of the cured mixed-shape V-SBR-MZ-35 composites compared with pure-shape V-SBR-S1-35 ( $\bullet\bullet\bullet$ ) and V-SBR-S5-35 ( $- - -$ ). a) V-SBR-MA-35( $- - \bullet\bullet$ ); b) V-SBR-MB-35( $- - \bullet\bullet$ ); c) V-SBR-MC-35 ( $- - \bullet$ ); d) V-SBR-MD-35( $- - \bullet$ ).

The temperature dependence of the loss modulus  $G''$  is reported in Figure 13 for V-SBR-SX-35 mixed-shape nanocomposites, and compared with with pure-shape V-SBR-S1-35 and V-SBR-S5-35. The  $T_g$  results in all cases to lay in between the values for pure-shape nanoparticles with a slight tendency to increased with increasing amount of spherical nanoparticles (table 5.2).

Compound	V-SBR-MA-35	V-SBR-MB-35	V-SBR-MC-35	V-SBR-MD-35
Measured $T_g$	-23,5	- 23,8	- 24.0	-24.3

**Table 5.2:** Main glass transition temperature of V-SBR-MZ-35 nanocomposites.

Nevertheless, the values are quite similar, indicating a specific plasticization effect that can be ascribed just to the formation of a dual shape network, with characteristics different from the network formed by its pure constituents, with just little dependency on the relative amount of  $\text{SiO}_2$ -S1 and  $\text{SiO}_2$ -S5 in the mixture.

### 5.5 Tensile tests and Mullins effect

Tensile stress-strain tests of V-SBR-SX-35 were performed to study the material's behavior under high deformation. Stress strain profiles and the values of elongation/stress at break are reported in Figure 14 and Table 3.

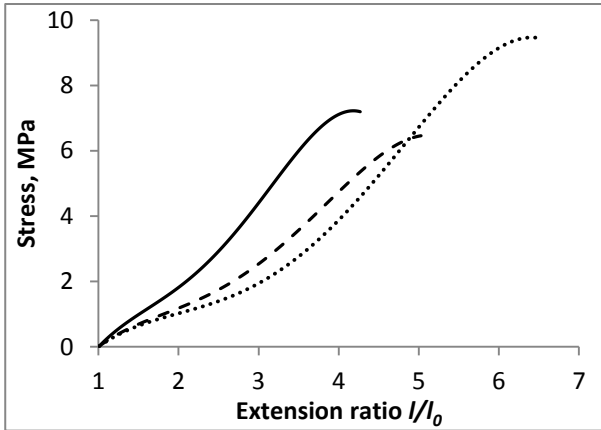


**Figure 5.14:** Tensile stress-strain profile for V-SBR-S5-35 (full line), V-SBR-S2-35 (—) and V-SBR-S1-35 (-) nanocomposites

	V-SBR-S1-35	V-SBR-S2-35	V-SBR-S5-35
Stress at break[MPa]	9.45	6.46	7.19
Elongation at break[%]	551	403	328

**Table 5.3:** Stress and elongation at break from tensile stress-strain measurements for V-SBR-SX-35 nanocomposites.

V-SBR-S5-35 showed the highest stress value for the whole strain range, confirming the higher reinforcement when increasing the particle anisotropy. On the other hand, the values of elongation at break decreased by increasing the particle AR. Therefore, in order to further investigate the tensile properties of the nanocomposites, the strain induced topological changes in the composites were studied by testing the pre-strained specimens. The so called Mullins effect describes the pre-strain induced softening. This test consists in a set of elongation-retraction cycles providing information on the changes of structure with increasing strain. The cycles of stress/strain measurements at increasing strain (from 5% to 45 %) for V-SBR-S1-35 and V-SBR-S5-35 are shown in Figure 15 a and b. The stress values of V-SBR-S5-35 samples are always higher than those of V-SBR-S1-35 at every strain value. By stepwise increasing deformation up to 25 % strain, both samples exhibit viscoelastic behavior, and the next stress-strain elongation curves (full lines in Figure 15) are superimposable with the previous ones. After the pre-strain of V-SBR-S5-35 at 30 %, the next curve shows strain softening and a lower stress value in the strain region up to 30 % due to non-Gaussian effects. This softening is the result of the filler-filler break-down and the filler-

polymer contact sliding at the critical strain of 30 %. The Mullins softening is more significant in the further elongation steps at increasing strain. The area between the curves of the two subsequent elongation steps corresponds to the energy loss per volume unit at the Mullins softening. For example, V-SBR-S5-35 pre-strained at 40% results in a stress decrease ( $\Delta\sigma$ ) with respect to the next elongation, 45%, of 40 kPa (i.e. 6 % of the stress value measured at the same strain, 35%) (see Fig. 15 d). This effect is much smaller in the case of V-SBR-S1-35 where the pre-strain at 40% leads to the stress softening by 15 kPa, i.e. 2.4% (see Fig. 15 c).

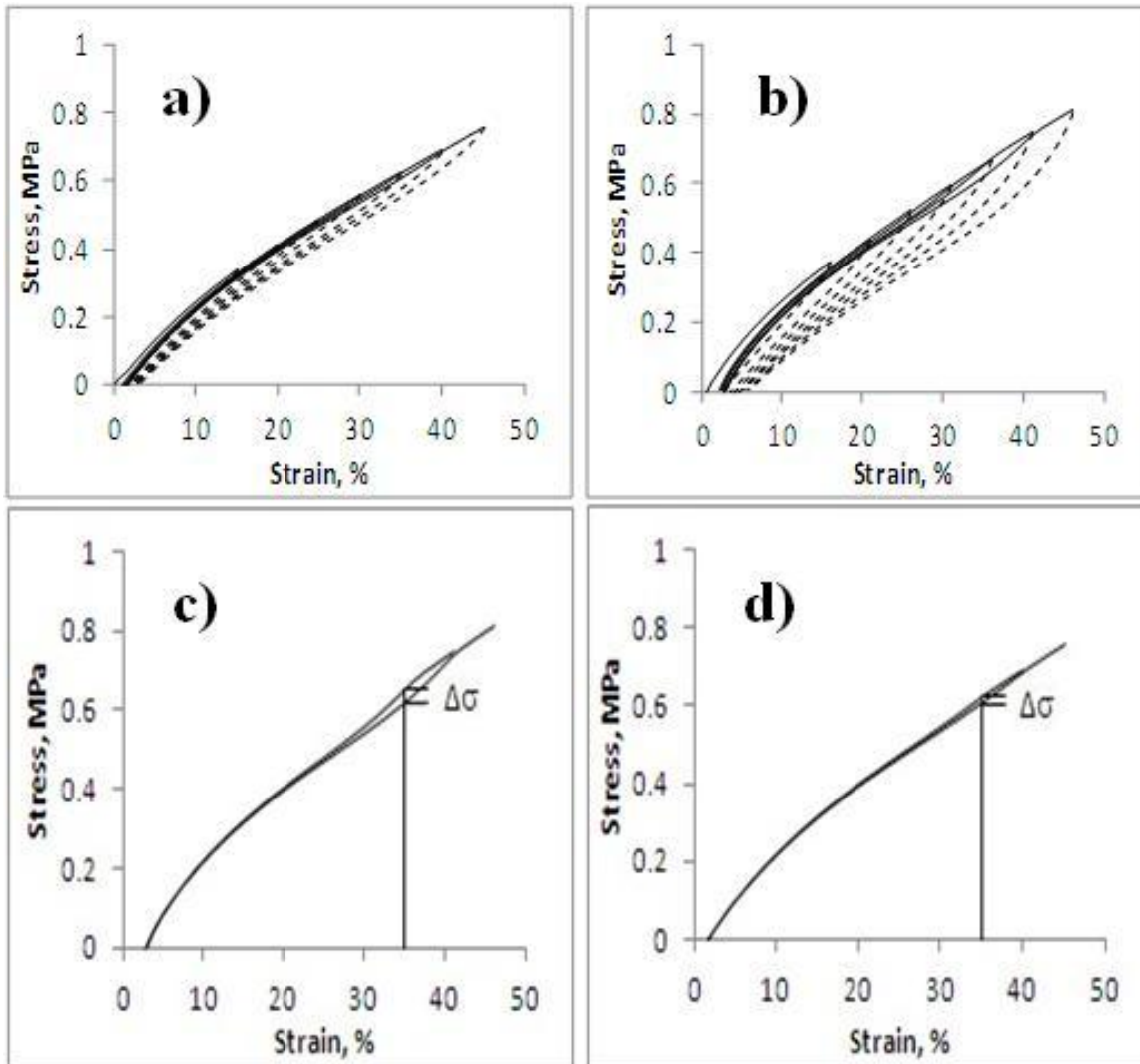


**Figure 5.15.** Loading (full line)/unloading (—) cycles for (a) V-SBR-S1-35 and (b) V-SBR-S5-35. The stress decrease ( $\Delta\sigma$ ) measured at 35 % strain of (c) V-SBR-S1-35 and (d) V-SBR-S5-35 pre-strained at 40% and 45%.

The higher extent of strain softening in V-SBR-S5-35 implies a greater amount of reinforcing physical interactions. Moreover, both samples display a quasi-permanent deformation (tension set) of 1-3 %, even after relaxation at rest, being higher in the case of V-SBR-S5-35. These results confirm that V-SBR-S5-35 filled with anisotropic particles and having a network with a higher

amount of immobilized rubber, presents higher stress value compared to V-SBR-S1-35. This more efficient reinforcement was proved to be brought about by stronger physical interaction broken down at the critical strain. In fact, the observed Mullins effect in the region of small strains (35-45%) is mainly a result of breaking the filler aggregates and, to a smaller extent, of an interface sliding mechanism which is dominant at higher strains<sup>8</sup>. The Mullins curve for V-SBR-MA-35 (not reported) is almost super imposable on the curve of V-SBR-S5-35, even if the composition of V-SBR-MA-35 is much closer to V-SBR-S1-35 than to V-SBR-S5-35. The pronounced hysteretical loss  $\Delta\sigma$  together with the high reinforcement are similar in V-SBR-S5-35 and V-SBR-MA-35, which possess an higher amount of bound rubber in comparison to V-SBR-S1-35 nanocomposite. This result endorse the hypothesis that the Mullins effect observed is a result of an interphase breaking mechanism that involve the presence of a certain amount of immobilized rubber.

## References

- (1) R. A. Vaia and J. F. Maguire *Chem. Mater.* **2007**, 19
- (2) H. Hua, L. Onyebuekea, A. Abatan, *Journal of Minerals & Materials Characterization & Engineering*, 2010, **9**, 275-319
- (3) H. Montes, T. Chaussée, A. Papon, F. Lequeux, and L. Guy, *Eur. Phys. J. E*, 2010, **31**, 263–268
- (4) A. P. Meera, *J. Phys. Chem. C* 2009, **113**, 17997–18002
- (5) Varghese S., Karger-Kocsis J., Gatos K.G., *Polymer* **2003**, 44, 3977–3983
- (6) Arrighi V., McEwen I.J., Qian H., Serrano Prieto M.B., *Polymer* **2003**, 44, 6259–6266
- (7) Barut G., Pissis P., Pelster R., Nimtz G., *Phys Rev Lett* **1998**, 80, 3543
- (8) Bokobza L. *Rubber Chemistry And Technology* **2013**, 86, 423–448



## **Chapter 6**

## **CONCLUSIONS**

## Conclusions

Shape controlled spherical and rod-like silica NPs with different aspect ratios (1-10) were synthesized by a sol-gel method using TEOS and MPTSM as silica precursors and the surfactant CTAB as structure directing agent. NPs were used to prepare silica/SBR composites by blending method. In all nanocomposites SBR-SX-W both spherical and anisotropic rod-like NPs formed a network of particles bridged by thin rubber layers throughout the whole SBR matrix. The network is more homogeneous in samples containing spherical or near spherical particles than in samples with rod shape particles due to the anisotropic interactions between the elongated particles. In fact differently oriented domains of rods preferentially aligned along the main axis occurred when the length of the particles increases ( $AR > 2$ ). Dynamic-mechanical properties of SBR-SX-W composites indicate that the anisotropic rod-like particles provide stronger reinforcement of the rubber if compared to the spherical ones and that the effect increases by increasing the particle aspect ratio, up to 35 phr of silica content.

The morphology influence on the reinforcement was preserved also in V-SBR-SX-W after the vulcanization process. The mechanical reinforcing effect is basically related to the formation of a continuous percolative network of silica nanoparticles, connected by thin polymer films, throughout the rubber matrix. In detail, the increase of the reinforcing effect of the rod-like particles by increasing their aspect ratio is related to both the self-alignment of anisotropic particles along the major axis direction and to their very large filler/polymer interface, compared to that of spherical particles. This strong interaction originates a significant reinforcement even if the anisotropic particle form a network less continuous than in samples containing spherical or near spherical particles. The combined use of TEM and AFM tapping mode analyses revealed that in all the V-SBR-SX-W nanocomposites, spherical and anisotropic NPs are surrounded by a layer of immobilized rubber, stabilized at the particle interface. Spherical or nearly spherical particles show small contact zones sharing thin rubber layers. Rod shaped particles ( $AR > 2$ ) show instead oriented domains of rods preferentially aligned along the main axis, where an increase of rubber fraction trapped between the aligned particles is evident.

Low field  $^1\text{H}$  NMR measurements evidence that polymer chain dynamics of the rubber layers tightly bound to the silica particles are restricted by the interaction with the filler, increasing the stiffness with respect to that of polymer far from the particles. The thickness of this layer, named primary one, is smaller than that detected by AFM which includes also the outermost rubber chains crosslinked or entangled with the primary layer. The highest values of the rubber rigid fractions were observed in the case of anisotropic filler particles.

From DMTA data resulted that this is related to the self-alignment of anisotropic particles which immobilize larger amounts of rubber in the interparticle region than spherical particles. DMTA measurements evidence also that the presence of the rod-like silica domains induces a decrease of the packing density of the unbound polymer chains compared to the spherical particles, increasing the free volume in the rubber matrix and, consequently, reducing its glass transition temperature. The strong correlation between the results of the integrated multi-technique approach allows to visualize at the nanoscale level the immobilized rubber at the silica-rubber interface, and evidences the modulating role of the immobilized rubber on the macroscopic mechanical properties. The control of the silica shapes proposed in this thesis allowed to study the influence of the particle shape on the reinforcing effect independent of the surface chemistry and considering the aspect ratio as the only geometrical variance. The study confirmed that the filler particle anisotropy is crucial to vary the amount of immobilized rubber at the filler/rubber interface and the reinforcing effect, and that beyond maximizing the nanoparticle dispersion in the rubber matrix, the control of filler morphology is mandatory to obtain the desired modulation of the mechanical properties.





## **Appendix A**

### **CHARACTERIZATION METHODS**

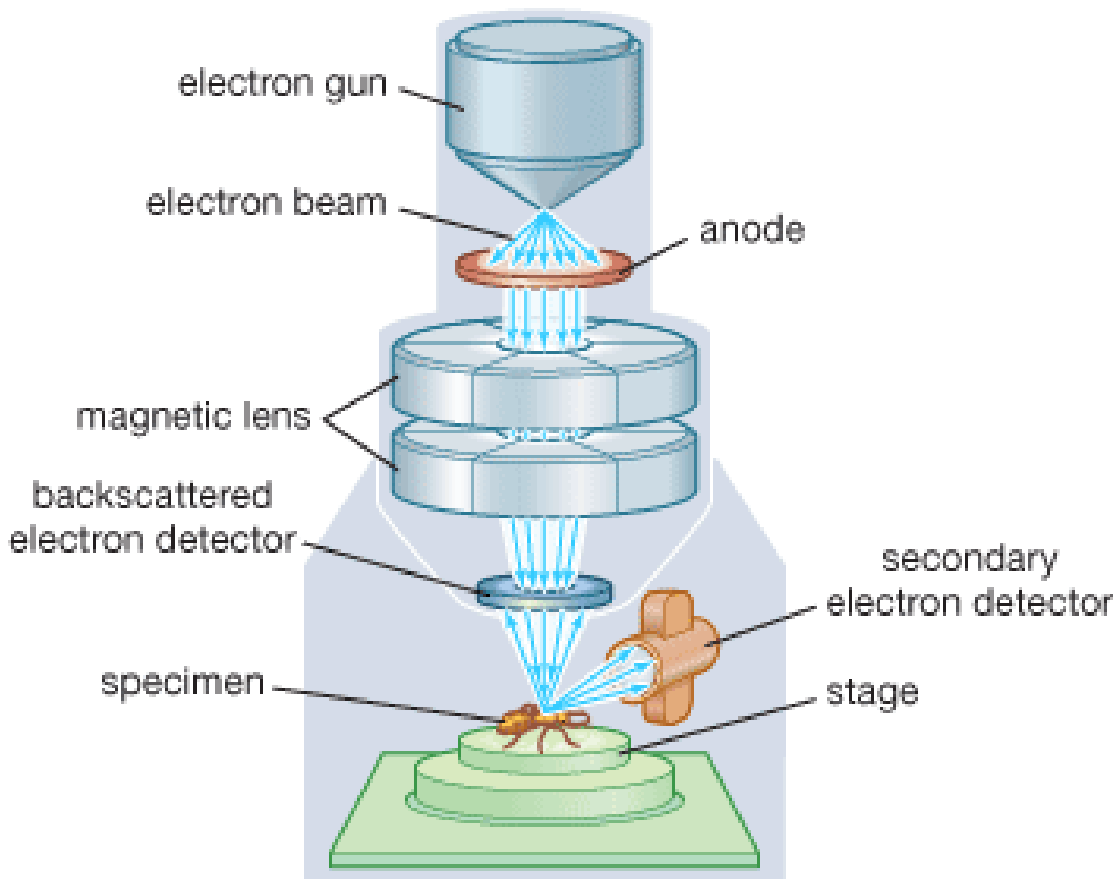
The aim of this appendix is to resume the analytical techniques employed in order to understand the structure-properties relationship of our materials. It will be divided into two main sections: first, characterization of bare nanofiller (3.1), prior to rubber compounding, and second characterization of the obtained nanocomposites (3.2). The techniques are grouped, for both cases, by morphological (3.1.1, 3.2.1) and materials properties (3.1.2, 3.2.2).

## **A.1 Filler characterization**

### **A.1.1 Morphological analysis**

#### **A.1.1.1 Scanning Electron Microscopy (SEM)**

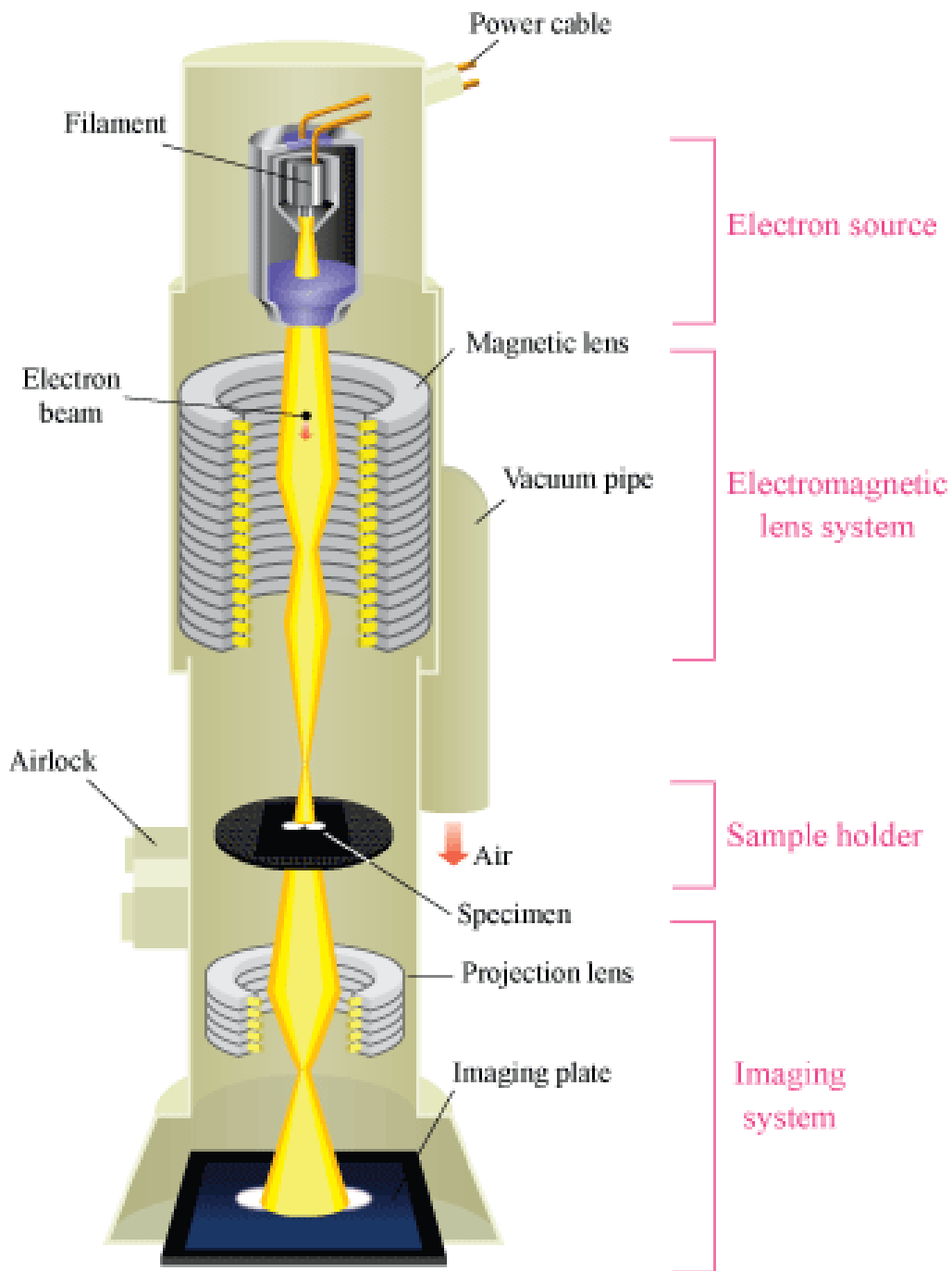
SEM is based on the emission of electrons from the surface of a sample to generate signals, and an image is formed. The apparatus consists in a column in which the electron beam is accelerated, a sample chamber in UHV condition to avoid collision of the beam with air molecules, a secondary electron detector (SED), and a computer connected with the instrument. A CCD camera is used to verify the sample Z position of the sample. In particular, a focused high-energy electron beam is pointed to the sample, in a repeated rectangular array. Secondary electrons with much lower energy (at least 10 thousand times less energetic than the original beam) are then back emitted by the interference of the surface atom of the sample with the incident beam. These are collected using a SED, which consists in a Faraday cage with a 300 volts positive charge connected to a collection target. The digital signal is converted in a grayscale image and shown in a monitor. The resolution depends mainly on the scanned area and allows to visualize objects as little as a hundred of nanometers. Measurements of the powders were done by a Vega TS5136 XM Tescan microscope in a high-vacuum configuration. The electron beam excitation was 30 kV with a beam current of 25 pA. Prior to SEM analysis, samples were stucked to a metallic target through a tape and gold-sputtered in order to improve the conductivity of the electrons through the material.



© 2008 Encyclopædia Britannica, Inc.

#### A.1.1.2 High-Resolution Transmission Electron Microscopy (HRTEM)

HRTEM is a technique that allows to obtain images of a nanostructured material at a much higher resolution than SEM. The apparatus is made of an electron beam source, a series of electromagnetic lenses (at least 5) to accelerate the electron beam at very high speed (up to 100KeV), and an imaging system of the electrons going through the sample, which converts the diffraction pattern into a 2D image. Going into detail, the technique makes use of both transmitted electrons and electrons generated by interaction of the beam with the sample, that are elastically scattered in the direction of the imaging system.

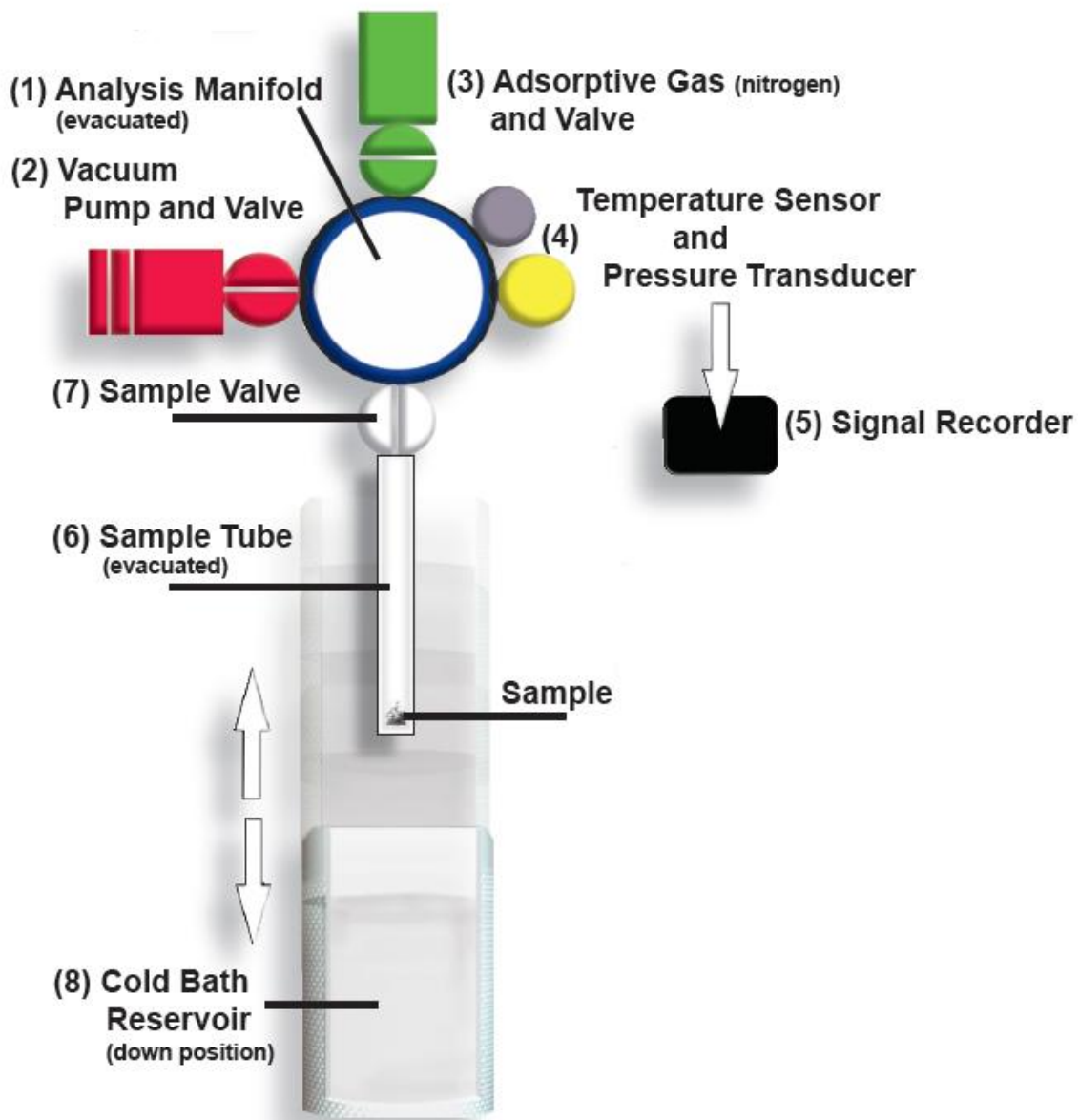


This means that the imaging system receives a diffraction pattern, that is reconstructed by the projection lens into a 2D image of the sample. Finally, the imaging plate on the bottom converts the incident electrons into visible light by fluorescence, and the visible image is detected by a CCD camera. The resolution depends mainly on the speed of the electron beam used, and modern HRTEM apparatus are able to resolve features as small as few nanometers. Morphological characterization of powders was performed on a Jeol 3010 High Resolution Transmission Electron Microscope (HRTEM) operating at 300 kV with a high-resolution pole piece (0.17 nm point to

point resolution) and equipped with a Gatan slow-scan 794 CCD camera. The powders were suspended in isopropanol, and a 5 mL drop of this suspension was deposited on a holey carbon film supported on 3 mm copper grid for HRTEM investigation.

### **A.1.1.3 Nitrogen adsorption (BET)**

Morphology of nanostructured materials can also be described by surface area and pore structure, and the technique of choice is nitrogen physisorption analysis according to the method described by Brunauer, Elmet and Teller (BET analysis). The apparatus consists in a main chamber (manifold) which is connected to a  $p_0$  tube at the saturation pressure of nitrogen, a tube containing the sample at pressure  $p$  and at the temperature of liquid nitrogen (77K), a vacuum pump, a gaseous nitrogen reservoir, pressure and temperature measurement systems. The analysis consists in the addition to the sample tube (previously evacuated and initially in high vacuum) of increasing amount of gaseous nitrogen from the manifold. The volume of input gas in order to reach a certain pressure in the sample tube and manifold is checked at every pressure step until saturation ( $p = p_0$ ), and an isothermal curve of volume against pressure at constant temperature (77K) is obtained. On the basis of the profile six kinds of curves and four kinds of hysteresis can be depicted for materials with different pore structure and surface morphology, as reported by the UPAC classification. Considering the space occupied by the adsorbate molecule on the surface, different geometrical models can be used to obtain values of specific surface area (SSA), pore volume (DCPV) and pore size distribution (PSD).

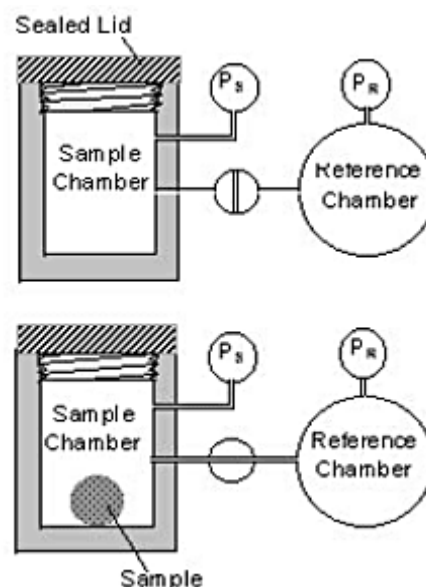


The external surface area can also be calculated by subtracting the surface area of the pores (obtained by DCPV) from the SSA. SSA and DCPV and pore size distribution of powders were measured by nitrogen physisorption using a Quantachrome Autosorb-1 apparatus according to BET and BJH methods. Powder samples were evacuated at 200°C for 16 h before the analysis.

## A.1.2 Bulk and surface properties

### A.1.2.1 Pycnometry

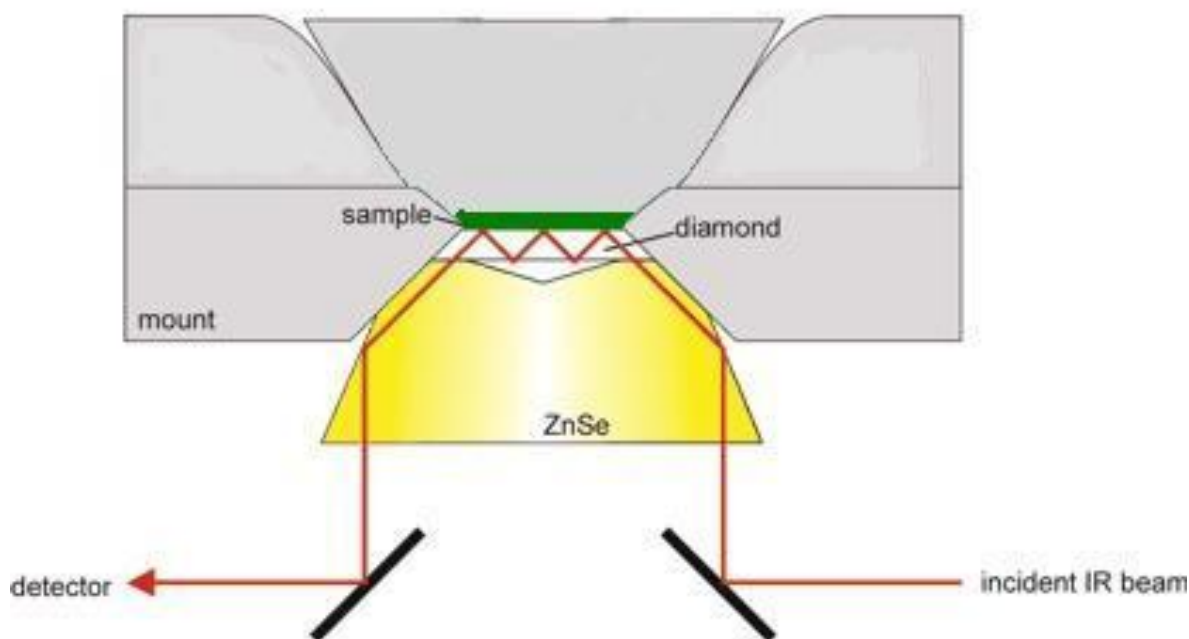
A gas pycnometer measures the difference of pressure between an empty sample cell and the cell with sample. The increase in pressure is related to the volume of gas displaced. When He is used as the analysis gas, all open voids are filled, thus He density is termed true density. The true density of powders was measured by a Micromeritics Accupyc 1330 gas pycnometer and the result utilized was the average of five measurements.



### A.1.2.2 Attenuated Total Reflectance Fourier Transform Infrared Spectroscopy (ATR-FTIR)

The surface chemistry of examined materials can be determined qualitatively by vibrational spectroscopy. The absorption of infrared radiation at different wavelengths is associated with the vibrational modes of different bonds, so different chemical species have characteristic infrared absorption spectra. Because of the difficulties of infrared light penetration in solid samples, the ATR device is used, and the radiation that comes to the detector is not transmitted through a bulky sample, but is many times reflected on it thanks to the ATR crystal. This contact is sufficient to allow absorption of IR radiation. The apparatus is made of: a sample holder that is pressurized by a steel piston (in order to maximize the contact area with the radiation), the ATR crystal, a source of IR radiation, and a detector. Since the radiation is passing through an interferometer before reaching the sample, Fourier Transform is applied to the detected signal in order to obtain a transmittance against wavelength spectrum from the interferogram. The measurements were performed by a Perkin Elmer Spectrum 100 instrument ( $1\text{ cm}^{-1}$  resolution,  $650\text{-}4000\text{ cm}^{-1}$  range, 16 scans).





### A.1.2.3 Thermogravimetric Analysis (TGA)

TGA allows to determine the amounts of physisorbed species and functionalizing organic molecules on an inorganic powder, by measuring the weight loss of the material as a consequence of a thermal treatment in a controlled atmosphere. Furthermore, unfunctionalized silica gels have a rich silanol surface chemistry that can be described by the weight losses that occur in different temperature ranges. In this way it is in fact possible to classify the two families of silanol groups, vicinal and isolated by the easier chemical desorption of the first group with respect to the second. The experimental setup comprises a quartz microbalance on which the sample is accommodated in a crucible, a heating oven, a gas pipeline and a computer. The instrument works in differential mode with a reference crucible placed on the balance arm, aside the sample crucible. The determination of weight loss profile was carried out by a Mettler Toledo TGA/DSC1 Star-e System. In order to calculate the silanol group present on the silica surface from the weight loss, the following formula was used, which takes into account the presence of functionalizing species inside the mesopores.

$$\left(\frac{n_{OH}-n_f}{2}\right) \times MW_{H_2O} + n_f MW_f = \Delta W_{150-1000}$$

where  $n_{OH}$  is the total number of hydroxy groups,  $n_f$  is the number of mercaptosilane groups calculated from the sulphur elemental analyses (see later)  $MW_{H_2O}$  and  $MW_f$  are the molecular weights of the water and the organic residual, respectively, while  $\Delta W_{150-1000}$  is the sample weight loss in the temperature range between 150 and 1000°C.

The density of silanol groups  $d_{OH}$  was calculated by TGA and SSA data, according the following equation, where  $N_A$  is the Avogadro number:

$$d_{OH} = \frac{n_{OH} \times N_A}{\Delta w_{150-1000} \times SSA \times 10^{18}}$$

#### **A.1.2.4 Elemental Analysis (EA)**

EA coupled with TGA allowed to isolate the component of weight loss associated with silanol species from the component due to sulfurated organic species. The apparatus consists in a furnace where the sample is allowed to decompose at high temperature in oxidative environment, and evolving species are detected by an atomic absorption analyzer. EA of sulfur content in  $SiO_2$ -X were performed by using a Thermo Flash EA1112.

#### **A.1.2.5 X-Ray Fluorescence (XRF)**

X-Ray Fluorescence is a non-destructive spectroscopic technique that allows for the determination of the characteristic lines of emitted fluorescence from the atoms constituting a solution or a solid finely particulate sample. All the nuclei with atomic mass higher than the sodium are in principle detectable with this methodology. In particular, using an internal standardization it is possible to obtain quantitative data if the analyzed nucleus is present in a concentration lower than 10% by weight (avoiding matrix effect). As an internal standard, it is possible to employ some ready-to-use reference materials prepared with atomic layer deposition techniques or similar, having an extremely reliable composition; on the other hand, it is possible to prepare solid mixtures or solutions at the correct element dilution by weighting precisely the constituents, of which the atomic composition is already known. Using internal standard with different concentrations, it is possible to build a calibration curve in which the emitted fluorescence intensity is correlated with the nucleus concentration. Values of magnesium concentrations in powdered samples were obtained by using a Bruker AXS S4 Pioneer XRF spectrometer operating at room temperature.

### **A.2 Nanocomposites characterization**

#### **A.2.1 Morphological analysis**

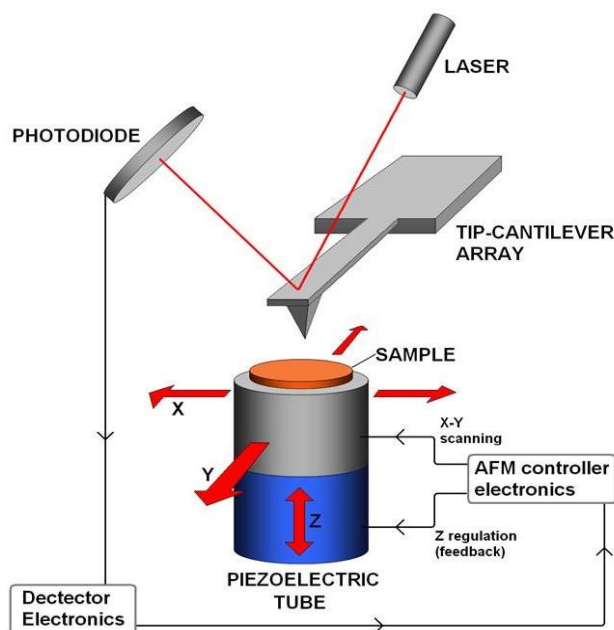
##### **A.2.1.1 Transmission Electron Microscopy (TEM)**

Transmission electron microscopy principles are already described in A.1.1.2, with the difference that an electron beam of lower energy has to be employed in order to avoid destruction of the polymeric matrix, and the sample preparation is more complicated. In detail, the investigation of both uncured and vulcanized composites was carried out by using a Zeiss EM 900 microscope. Ultrathin sections (about 50 nm thick) of composites were obtained with a Leica EM FCS cryo-

ultramicrotome equipped with a diamond knife, by keeping the samples at  $-130\text{ }^{\circ}\text{C}$ . The thickness of the specimens ( $\sim 40\text{ nm}$ ) can cause the longest silica particles to be cut, depending on their orientation. So the presence of some anomalous shorter and thinner particles in the TEM images may be due to the sectioning of the samples.

### A.2.1.2 Atomic Force Microscopy (AFM)

AFM is a microscopic technique from the family of Scanning Probe Microscopies (SPM), which groups all the technique that use a probe to scan a surface in a raster pattern and to create an image. In particular, AFM exploits the contact of an ultra sharp tip (having an apex just few nanometers large) with an almost flat surface which is kept on an equilibrium distance of few nanometers from the tip. The tip is mounted on a flexible cantilever. The equilibrium position corresponds to a minimum of energy due to the compensation of the attractive Van Der Waals force with the repulsive electrostatic force acting between the charged tip and the surface. The cantilever can have a starting deflection in the equilibrium position. During the scan, as the tip encounters higher or lower surface features, it further deflects to keep the equilibrium distance. The deflection is in the range of nanometers or even angstroms, but can be measured with high accuracy by a laser beam which is reflected by a cantilever into a diode detector. The piezoelectric tube is hence stimulated to modify the z position as a consequence of the cantilever deflection detected by the laser-diode system, in order to keep the equilibrium position. From the piezo tube z displacement it is possible to obtain an height image of the material. This is the original operating mode, also referred to as contact mode AFM.



Conversely, operating in tapping mode, the cantilever is oscillated at a constant frequency between an alternating attractive and repulsive force, while the tip scans the surface. Two similar height images are in this case obtained: since the oscillation amplitude change causes the piezo tube to displace, one image is obtained by the change in amplitude (Amplitude Error Image) and another is obtained from the z displacement (Height Image). Generally speaking, in contrast to height signal, the amplitude error signal shows contrast only at the interface, where the height changes sharply. During the oscillations, when the tip is in close contact to the surface, a repulsive force is exerted. This can be divided into two component (in-phase and out-of-phase), that correspond to an elastic repulsion rather than an inelastic one. The factors influencing the ratio between the two components include adhesive forces between tip and sample, and the modulus of the surface feature examined. The overall elastic vs inelastic component is summarized by a phase signal recorded at each point of scanning, that can be transferred into an image (Phase Image), which gives qualitative information about the local stiffness of the material, in other words, the materials heterogeneities. To sum up, AFM measurement conducted in tapping mode gives three simultaneous images (Height, Amplitude Error, Phase) of the materials surface that give a morpho-mechanical description of his heterogeneities at the nanoscale. The bulk morphology was evaluated by imaging the fracture area after previous freeze-fracturing of cured composites at the temperature of liquid nitrogen. Investigation of the surface topography was done by an atomic force microscope (MultiMode Digital Instruments NanoScope Dimension IIIa), equipped with the SSS-NCL probe, Super Sharp Silicon SPM-Sensor (NanoSensor Switzerland; spring constant 35 N/m, resonant frequency 170 kHz). Measurements were performed under ambient conditions using the tapping mode AFM technique. Surface images were taken by scanning sizes from 1 to 50  $\mu\text{m}$ . Investigations on crude materials was not possible because of their high stickiness.

## **A.2.2 Nanocomposites properties**

### **A.2.2.1 Thermogravimetric Analysis (TGA)**

Principles of TGA were already described in A.1.2.3. For silica/SBR nanocomposites, TGA analysis in air environment allows to verify the filler insertion in the rubber matrix. Quantitative determination of silica content in composites was carried out by Thermo Gravimetric Analysis (TGA), a Mettler Toledo TGA/DSC1 STAR-e System, at constant air flow ( $50 \text{ cm}^3 \text{ min}^{-1}$ ). The sample (20 mg) was placed in an alumina pan and heated under flowing air up to  $1000 \text{ }^\circ\text{C}$  at a heating rate of  $10 \text{ }^\circ\text{C min}^{-1}$ . The silica content was calculated by the following expression:

$$\text{SiO}_2 \text{ content (phr)} = \frac{W1}{W2} \times 100$$

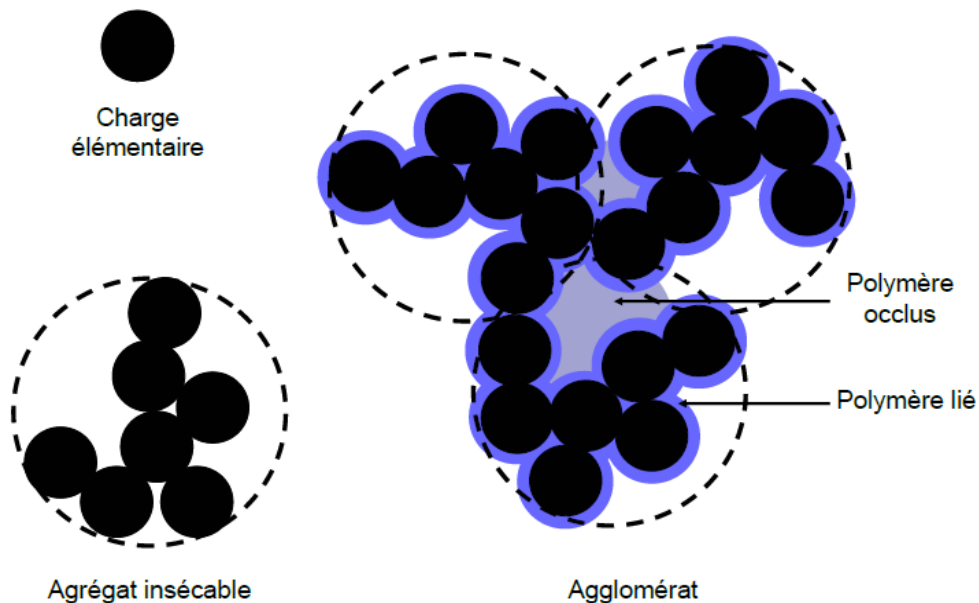
where W1 is the weight of remaining ash, W2 is the composite weight.

### A.2.2.2 Solvent extraction measurements

When a crude filler/rubber nanocomposite is contacted with a good solvent for rubber, the fraction that is not constrained by the presence of the filler is free to dissolve, while the remaining part is not. In this way it is possible to have a rough estimation of the bound rubber fraction. This last is composed by two contributions: the tightly bound interfacial rubber layer surrounding and interacting with the filler particle (by covalent or Wan Der Waals forces), and a more loosely bound rubber component, also called occluded, which is not in direct contact with the filler particle but is physically constrained by the filler particles organization (for example, inside agglomerates). The bound rubber fraction can be calculated with the formula:

$$B_r \% = \frac{\left[ m_d - m_0 \left( \frac{m_f}{m_f + m_r} \right) \right]}{m_0 \left( \frac{m_r}{m_f + m_r} \right)} \times 100$$

where  $m_d$  and  $m_0$  are the mass of dried and bare sample, respectively, and  $m_f$  and  $m_r$  are the fractions of the filler and the rubber in the compound as determined by TGA on uncured materials.



### A.2.2.3 Swelling measurements and Kraus approach

Vulcanized rubber does not dissolve as free crude rubber when in contact with a good solvent, because of the presence of covalent sulfur bridges that keep the network interconnected. What actually happens is that the solvent fills the spaces between macromolecular chains, expanding the network until the crosslinking density makes it possible. The extent of this expansion is measured as absolute swelling ratio, represented by the equation:

$$Q = \frac{m_s}{m_d}$$

where  $m_s$  is the weight of the swollen mass, and  $m_d$  is the weight of the swollen mass after vacuum removal of the solvent. This data is typically used for comparing vulcanized with different crosslinking densities, through the Flory-Rhener equation.

Further crosslinks can be due to the filler immobilization capability, a parameter that can be calculated by the Kraus approach. In fact, assuming that the filler does not swell, it is possible to calculate an immobilization constant  $c$  which reflects the capability of the filler to entrap increasing amount of rubber at increasing filler content, that can be correlated with the amount of rubber immobilized at the interface:

$$\frac{Q_r}{Q_{r0}} = \frac{v_{r0}}{v_r} = 1 - \frac{m\Phi}{1-\Phi}$$

where  $Q_r$  is the swelling ratio of unfilled cured material,  $Q_{r0}$  is obtained by the absolute swelling ratio  $Q_r = \frac{Q-\Phi}{1-\Phi}$ , and  $v_r$  and  $v_{r0}$  are the volume fraction of the unfilled and filled rubber, respectively and

$$m = 3c(1 - v_{r0}^{1/3}) + v_{r0} - 1$$

The constant parameter  $c$  corresponds to the slope of the straight line obtained from the plot of  $\frac{Q_r}{Q_{r0}}$  against  $\frac{\Phi}{1-\Phi}$ .

The swelling tests of the vulcanized compounds were performed using toluene as a solvent. Samples of size 10 x 10 x 2 mm<sup>3</sup> were immersed in 20 mL of toluene at room temperature for three days in a closed vessel in dark (in order to avoid photodegradation reaction of the compounds). Toluene was replaced daily to eliminate soluble additives (antidegradant, sulfur, CBS...). Finally, the swollen mass was weighted and dried to constant mass in vacuum.

#### A.2.2.4 Nuclear Magnetic Resonance (NMR)

The nuclear magnetic resonance (NMR) is a special technique that allows to analyze the chemical structure of a substance: it exploits the principle that the nuclei of the atoms of some elements, when subjected to an external magnetic field, orient themselves in the direction of the field imposed.

In general each nucleus is provided with a specific number of spin (I), for example,  $I = 0, 1 / 2, 1, 3 / 2$ , which depends on the mass number and the atomic number. Nuclei that have non-integer spin, originate an elementary magnetic field  $\mu$ , which makes them similar to small magnets. The nuclei of the common isotopes of carbon and oxygen (<sup>16</sup>O and <sup>12</sup>C) are not magnetic ( $I = 0$ ) and not give rise to phenomena of nuclear magnetic resonance; the atoms most used for this type of

analysis, and which are commonly present in the polymers, are  $^1\text{H}$  and  $^{13}\text{C}$ , which are equipped with number spin equal to 1/2.

When a magnetic nucleus is introduced in an external uniform magnetic field, the said nucleus will be oriented in one of only two possible directions, corresponding to an energy level of  $\pm \mu H_0$  (where  $H_0$  is the intensity of the external magnetic field). The orientation at low energy ( $-\mu H_0$ ) corresponds to nuclei with magnetic moment aligned parallel to the external magnetic field, while the orientation of the high-energy ( $+\mu H_0$ ) corresponds to nuclei antiparallel to the external field. The shift from a possible orientation to another is the result of absorption or emission a certain amount of energy, which equals  $E = h \nu = 2\mu H_0$  where  $h$  is Planck's constant and  $\nu$  is the frequency of the electromagnetic radiation that is absorbed or emitted. If the resonance frequency was the same for all the nuclei of the same type (for ex.  $^1\text{H}$ ) of a given sample, it would be observed in the resonance spectrum a single peak for each atomic species present. Indeed it is not: it is possible to observe slight differences in the resonance frequency of the NMR of the same atom according to its neighboring nuclei. The electrons surrounding, in fact, shield the nucleus in different ways, depending on the chemical structure of the molecule examined. To distinguish these subtle differences, the NMR spectrometer must be constituted by a very powerful electromagnet establishing a stable and homogeneous magnetic field, then a radio waves emitter, a receiver and an apparatus capable of varying the frequency of the radiation in a narrow range.

The deviation of the resonance frequency of the nuclei with respect to a certain molecule taken as standard takes the name of the chemical shift. This quantity is defined by

$$\delta(\text{ppm}) = \frac{(\nu_r - \nu)}{\nu_r}$$

where  $\nu_r$  is the resonance frequency of a particular reference group, and  $\nu$  is the frequency of resonance of the sample considered. Typically for the  $^1\text{H}$  nucleus,  $\delta$  is the range 0-10ppm.

The NMR analysis on the nucleus  $^{13}\text{C}$  is possible but quite difficult because of its natural abundance (about 1%, the rest is  $^{12}\text{C}$ ), then only a few carbon atoms will be oriented, consequently the signal/noise ratio will decrease.

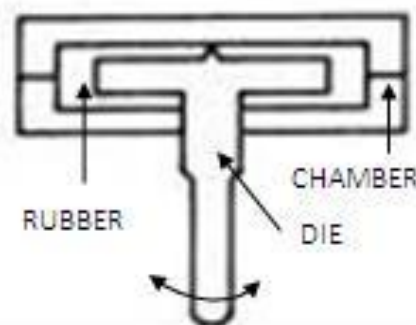
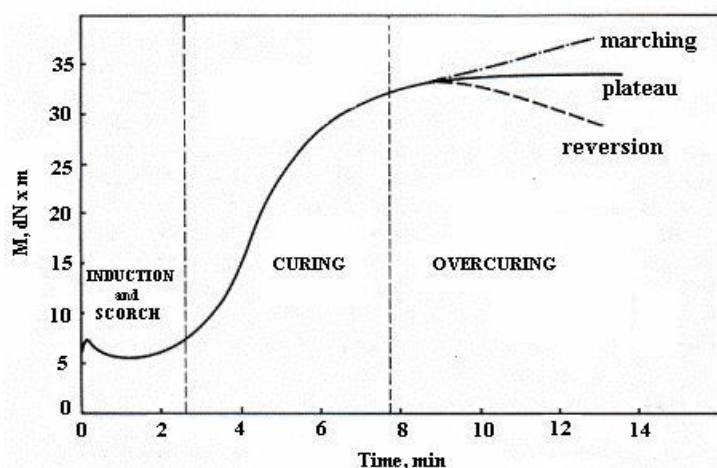
In a  $^1\text{H}$ -NMR spectrum can be seen that hydrogen atoms with "chemical environments" different match different peaks; Moreover, by the area underlying each peak, we can determine the relationship between the different types of hydrogen atoms present. The area of a peak in fact, is independent of the structure to which it is linked the corresponding hydrogen, depends only on the frequency with which the atom is repeated within the molecule. Then dividing the area of each peak

by the number of nuclei in whose corresponding values are obtained perfectly comparable with those given by the chemical formula which corresponds to the substance analyzed.

Proton ( $^1\text{H}$ -NMR), carbon ( $^{13}\text{C}$ -NMR) and silicon ( $^{29}\text{Si}$ -NMR) nuclear magnetic resonance are employed to verify the structure and to determine the composition of the specimens. Furthermore, the  $^1\text{H}$ -NMR is also conducted with low magnetic field spectrometers (LF $^1\text{H}$ -NMR), without distinguishing the chemical shifts, just to measure the transverse relaxation time  $T_2$ . This will be explained in detail in the paragraphs dedicated to NMR spectroscopy (4.4)

#### A.2.2.5 Moving Die Rheometry (MDR) and curing kinetics.

Rheological measurements are the main techniques to evaluate dynamo-mechanical performances of rubber nanocomposites. These can be also measured at any moment during the vulcanization process, that is the formation of chemical crosslinks: therefore, it is a branch of the so-called chemorheology. In particular, moving die rheometers make use of a steel die oscillating at a constant frequency and strain amplitude. The crude material is placed all around the die, and the whole system is enclosed in a pressurized thermostated chamber, as represented schematically in figure. Upon heating at a chosen vulcanization temperature, the vulcanization process starts, and it can be



followed by the increase of the torque acting on the moving die, which is a

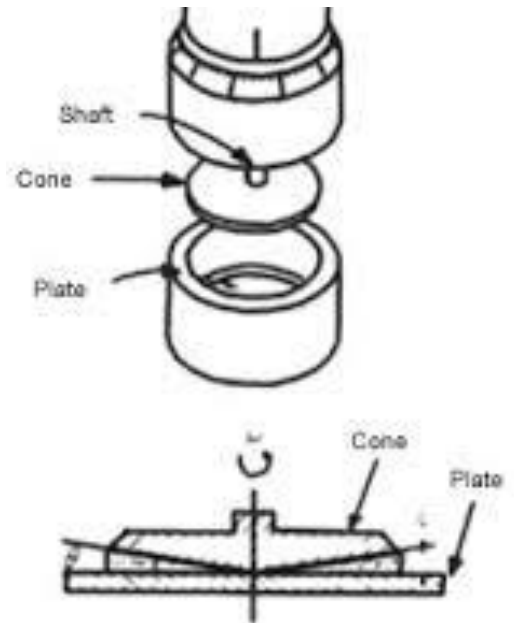
consequence of the increase of elasticity that is occurring in the material. A typical curve of a vulcanizing system is reported below: in the first part (induction), we observe a materials softening due to the heating, and a subsequent increase (also referred to as scorch) due to the starting of the vulcanization reaction; in a second time, the curve increase rapidly, as a consequence of the curing reaction, reaching a plateau, corresponding to the end of the vulcanization. Overheating may cause a reversion of the vulcanization process, represented by the third part of the curve that is deleterious for the final material properties. The main result from the curve is the optimal curing time at which the material can be completely vulcanized avoiding overcuring reaction to take place. Curing



profiles of crude compounds were measured with a Moving Die Rheometer (RPA 2000, Alpha Technological) under the following conditions:  $\pm 1^\circ$  oscillation angle,  $170^\circ\text{C}$  temperature, 4.3 bar pressure and 30 min running time.

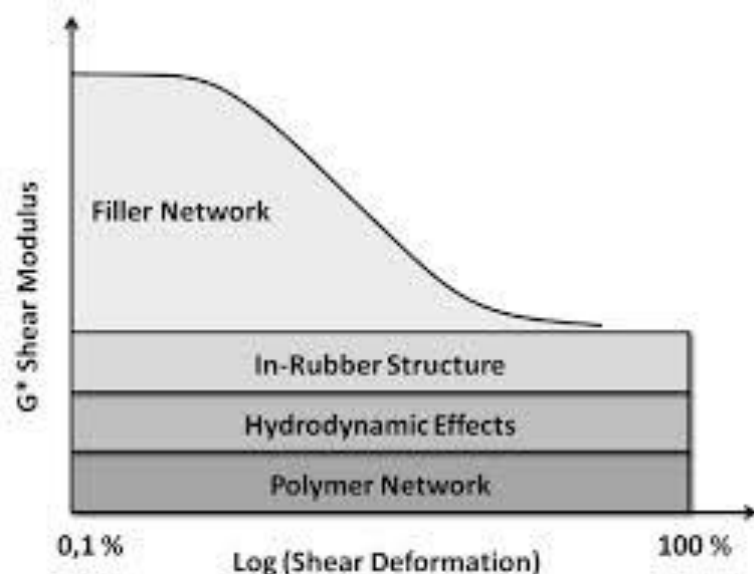
#### A.2.2.6 Oscillating Disk Rheometry (ODR) and stress-strain measurements

Filled rubbers are characterized by Payne effect, consisting in a strain softening phenomenon, due to the destruction of the filler network. Since the filler network the main cause of the reinforcement, at some critical value of strain the Storage Modulus  $G'$  drops from a starting plateau position (integer network) to a final plateau position (distrupted network), see image below. The extent of the Payne effect is related to the balance between filler-filler and filler-rubber interaction: it has been demonstrated for many different nanofiller shapes and nature of the interphase. The testing chamber is composed by an upper moving part (rotor), with cone geometry and a lower part (stator), with plate geometry.



The torque acting on the rotor during oscillation can be transformed into a value of modulus and divided into a real and an imaginary part, giving the Storage Modulus  $G'$ , associated with an elastic response, and the Loss Modulus  $G''$ , associated with a viscous response. The ratio between  $G''$  and  $G'$  ( $\tan\delta$ ) is a predictive number of the energy disipated from the tire during usage.

ODR measurements of crude composites was performed by Rubber Process Analyzer (RPA2000, Alpha Technologies) by applying a shear stress mode. The strain sweep tests were carried out at  $70^\circ\text{C}$  and 1 Hz from 2 to 100 % of elongation. Same measurements was also performed on cured composites, after vulcanizing the crudes in the testing chamber at the



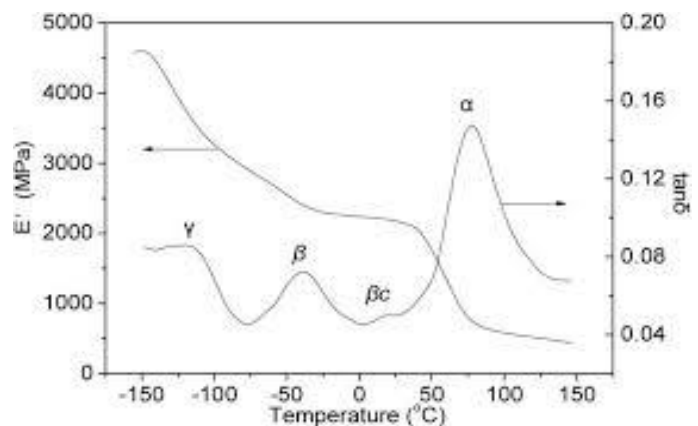
optimum temperature. In this case the strain sweep was carried out at  $70^\circ\text{C}$  and 10 Hz, from 0,2 to 10% elongation. Specimens were cut by using a Constant Volume Rubber Sample Cutter (CUTTER

2000, Alpha Technologies); the dimensions were 3.5 cm diameter and  $\approx 0.2$  cm thick, the weight  $4.5 \pm 0.3$  g. Two measurements were carried out for each sample, and the average value was reported.

#### A.2.2.7 Dynamo Mechanical Thermal Analysis (DMTA)

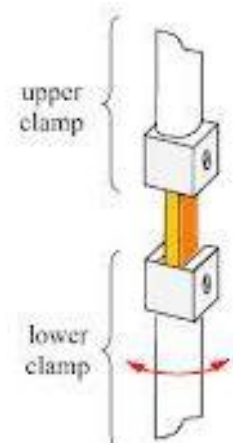
Dynamo mechanical measurement of the final material can be also conducted along a wide temperature range, above and below the glass transition temperature of the material. The main interests in using DMTA as an additional dynamo mechanical technique are, first, the identification of the correct glass transition temperature more precisely than DSC (Differential Scanning Calorimetry), as seen by the mechanical relaxation of polymer chains, and second, the identification of the relaxation modes different from the glass transition. In fact, while increasing the temperature, other chain relaxation phenomena can occur, as a result of increasing entropy: for example in polar polymers hydrogen bonds can break upon a certain temperature, allowing new segmental movements to take place, or in filled polymers the chains interacting with the filler surface can increase their mobility at temperatures that are different from the main glass transition.

An example of a silica filled thermoplastic polyurethane, in which these effects are both presents, is shown in figure: the profile of  $\tan\delta$  against temperature clearly show the presence of different relaxation phenomena.



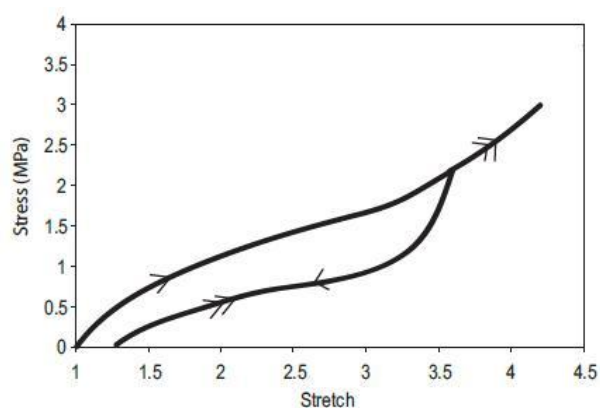
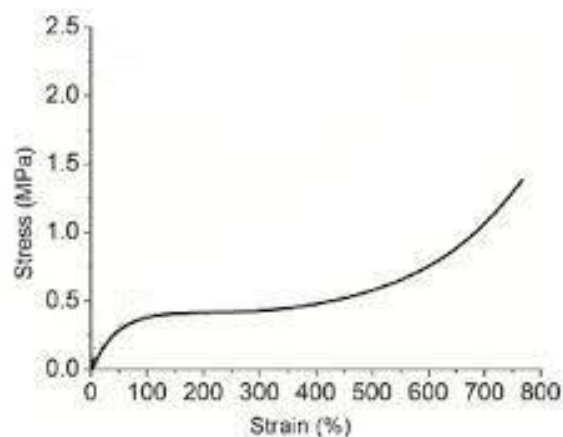
The greek letters denotes different relaxation

processes, and in general the ‘ $\alpha$  relaxation’ terminology is used for the main glass transition. The instruments setup is composed by a thermostated chamber, in which the sample is a rectangular slab, clamped on the upper part with a static clamp, and on the lower part with a moving clamp (see picture). Dynamic mechanical characterization of cured materials was performed by a TA Ares G3 instrument by applying a shear stress mode. Temperature dependence of the complex shear modulus of rectangular samples ( $5 \times 1 \times 0.25$  cm<sup>3</sup>) was measured by oscillatory shear deformation at a constant frequency and deformation amplitude.



### A.2.2.8 Tensile tests and Mullins effect

Dynamo-Mechanical analysis in tensile mode can be supportive of the data collected in shearing mode for cured compounds, because they can explore a much wider spectrum of deformation values, until failure. A typical tensile curve for an unfilled vulcanized rubber is reported in figure. Tensile properties at high extensions can be predictive of stability and ageing properties of the materials, that are related to strain-induced crystallization phenomena, final extensibility of polymer chains and to the mechanism of disruption of the interphase between filler and rubber. In particular, cyclic loading/unloading tensile tests can more precisely reveal which part of the input strain can be recovered and which cannot. This phenomenon of strain induced permanent deformation (more precisely pseudo-permanent, since the recovery time is not infinite) has been extensively studied by Mullins, hence it is referred to as Mullins effect. Two idealized cycles are shown in figure. In the first loading cycle (ascending single arrow) the material is still following the theoretical stress strain profile represented in figure, while the second loading cycle (ascending double arrow) show an inflection which is due to the yielding of the material. The instruments mainly consists in a couple of clamps (one fixed to the load cell and one movable through the moving crosshead) in the middle of which the a dumbbell-shaped (see chap. 3) specimen is put. The extensometer is generally a video camera which measure the actual strain value of the material at each point, while the stress is recorded from the moving crosshead. Tensile properties and Mullins effect were measured on an Instron 5800 apparatus at 22 °C and a crosshead speed of 50 mm/min. The equilibration time between each cycle was 30 minutes.



### A.2.2.9 Dynamic compression experiments

Dynamic compression experiments on cured compounds simulate the real conditions of material usage in a tire. As in tensile tests, it is possible to measure the Storage modulus, Loss modulus and  $\tan\delta$ . The moduli obtained by compression experiments can be related to tensile moduli, by taking into account the Poisson's ratio of the material (for rubbery materials is about 0,35)

$$E = 2G \times (1 + \nu)$$

The instrument is composed by two plates (one static and one vibrating) that compress a cylindrical sample until a starting value of compression figure (a). During the measurement, the vibrating up and down to give a periodic compression to the sample centered in the initial value of compression, see figure (b). The measurements were performed on an INSTRON Dynamic Dynamometer 1341 at compression from 3 to 25% operating at 10 Hz and at 70°C, simulating the operating temperatures of a tire in dry conditions.

